Engineering highly active and diverse nuclease enzymes by combining machine learning and ultra-high-throughput screening

Neil Thomas*[,1], David Belanger*[,2], Chenling Xu[3], Hanson Lee[3], Kathleen Hirano[3], Kosuke Iwai[3], Vanja Polic[3], Kendra D Nyberg[3], Kevin Hoff[3], Lucas Frenz[3], Charlie A Emrich[1], Jun W Kim[1], Mariya Chavarha[4], Abi Ramanan[1], Jeremy J Agresti[3], Lucy J Colwell[2,5]

1 X, the Moonshot Factory
2 Google Deepmind
3 Triplebar
4 Google Accelerated Sciences
5 Dept. of Chemistry, Cambridge University
* denotes equal contribution

Correspondence to: Neil Thomas <thomas.a.neil@gmail.com>, David Belanger <dbelanger@google.com>, Lucy Colwell <lcolwell@google.com>

Abstract

Designing enzymes to function in novel chemical environments is a central goal of synthetic biology with broad applications. In this work, we describe a campaign guided by machine-learning (ML) to engineer the nuclease NucB, an enzyme with applications in the treatment of chronic wounds. In a multi-round enzyme evolution campaign, we combined ultra-high-throughput functional screening with ML and compared it to parallel campaigns of *in-vitro* directed evolution (DE) and *in-silico* hit recombination (HR) . The ML-guided campaign discovered hundreds of highly-active variants with up to 19-fold nuclease activity improvement, outperforming the 12-fold improvement discovered by DE. Further, the ML-designed hits were up to 15 mutations away from the NucB wildtype, far outperforming the HR approach in both hit rate and diversity. We also show that models trained on evolutionary data alone, without access to any experimental data, can design functional variants at a significantly higher rate than a traditional approach to initial library generation. To drive future progress in ML-guided design, we curate a dataset of 55K diverse variants, one of the most extensive genotype-phenotype enzyme activity landscapes to date. Data and code is available at: https://github.com/google-deepmind/nuclease_design.

Introduction

The ability to engineer proteins has revolutionized applications in industry and therapeutics[1–6]. Generally, a protein engineering campaign can be divided into two stages[7–9]. First, the *discovery*

phase seeks to find initial candidate proteins that perform a desired function with a non-zero level of activity. After an initial functional candidate has been identified, the *optimization* phase seeks to improve its attributes, such as the binding strength of an antibody[10] or the catalytic activity[11], thermostability[12,13], or stereoselectivity of an enzyme[14]. *Directed evolution* (DE) is the standard technique for protein optimization, where a pool of genotypes is iteratively improved using *in-vitro* selection and mutagenesis[15–18]. Proteins designed by DE have been applied in many industrial and therapeutic settings[19], but DE has drawbacks: a DE campaign can fail to cross valleys in the protein fitness landscape and the diversity of the pool can collapse, leading to dead ends in an optimization campaign[20].

One way to improve directed evolution is to increase the size of the population being evolved, using for example, automation[21], microfluidics[22,23], display systems[23–26] or multiplexing[27] to screen large pools in parallel, or by applying selective pressure to continuously-evolving populations [28,29]. While the scale of such approaches can be quite large, the population of genotypes is typically updated through random mutagenesis or recombination, either performed intentionally by protein engineers or arising through natural mechanisms as the population evolves continuously. Such a simple local search strategy can hinder optimization performance.

As such, protein optimization can also be improved by more precise, systematic exploration of the protein fitness landscape. While DE alternates between hit selection and mutagenesis, ML-guided directed evolution (MLDE) alternates between data collection, modeling, and suggesting new genotypes using the model[30]. A number of recent surveys discuss the state of MLDE, much of which is powered by advancements in deep learning methods for generating protein sequences and predicting protein fitness[9,31–34]. Both MLDE and DE benefit from the deeper exploration of the fitness landscape afforded by higher screening throughput, yet there is limited prior work directly comparing the two approaches across multiple rounds of high-throughput experiments. Instead, many case studies demonstrating MLDE success have occurred in regimes with such low throughput that a standard DE workflow based on random mutagenesis and screening would be infeasible[35–40], have only performed a single round of experiments[41,42], or have sought to maintain a target phenotype instead of improving it[43].

In this study, we show that MLDE can design diverse, high-activity proteins better than DE when both employ the same ultra-high-throughput microfluidics platform in a multi-round protein engineering campaign. We engineer NucB, a biofilm-degrading endonuclease with applications in chronic wound care[44–46] and anti-biofouling[47]. NucB is secreted naturally by *Bacillus licheniformis*[48] and can degrade the DNA in the extracellular matrix required for the formation of biofilm[49]. NucB is active in its native context at alkaline pH, but experiences about an 80% reduction in enzymatic activity at pH 7 (Supp. 6D). The goal of our protein engineering campaign was to not only restore but improve NucB's nuclease activity at pH 7, a necessary prerequisite for its application as a wound healing therapeutic at physiological pH[50].

The paper has the following overall contributions: we identify high-activity NucB variants that are promising candidates for biofilm degradation, we show that an MLDE campaign delivers demonstrable benefits in activity and diversity over DE in finding such variants, and we

demonstrate that zero-shot design can generate better initial libraries than error-prone PCR. In the process, we identify general guidelines for ML-guided protein design. All experimental data from the project along with code reproducing our analyses is available at github.com/google-deepmind/nuclease_design.

Results

Our ML-guided campaign approach (**ML)** employed a portfolio of approaches (see Methods) that progressed from simple exploration of the fitness landscape to exploiting the predictions of neural networks fit on the wealth of data accumulated across multiple rounds of experiments. Each approach used the following general framework (Figure 1d). First, we trained a sequence-fitness model, which provides an *in-silico* fitness landscape. Then, after identifying candidate sequences *in-silico* with high predicted fitness, we selected a diverse subset for screening in the next round. Within each round, we divided our design budget among multiple methods to increase library diversity and to investigate various algorithmic choices.

An ultra-high-throughput microfluidic platform was used to measure the catalytic activity of large libraries of NucB variants at pH 7 simultaneously (Figure 1a). Variants were transformed into *B. subtilis* and individually encapsulated into droplets. After growth and protein expression, the nuclease substrate, a 20-mer dsDNA carrying a dye and a quencher, was injected into the droplets. Cleavage by the nuclease causes the dye and the quencher to separate, increasing the fluorescence of the droplet (see Supplementary Figure 27). Since nuclease activity is tied to fluorescence, droplets can be sorted (Figure 1a) to (i) sequester the best-performing variants (Figure 1b) or to (ii) create genotype-phenotype datasets of amino acid sequences and corresponding functional activity (Figure 1c). Below, we further purify and validate top hits using lower-throughput assays.

We ran 3 additional campaigns to provide qualitatively different baselines (Figure 2a). The independently-run directed evolution campaign (**DE**) involved two generations of hit selection and *in-vitro* mutagenesis using the same ultra-high-throughput platform (see Methods and Supplementary Figure 18). To enable finer-grained assessment of the overall composition of the **ML** library, we also ran a hit recombination (**HR**) campaign that was pooled with **ML** for all experiments. **HR** variants were designed *in-silico* to simulate *in-vitro* hit stacking, where novel recombinations of the top-ranked variants from the previous-round's dataset are sampled. Finally, we designed a zero-shot library (**ZS**) using a model of natural NucB homologs to investigate whether NucB activity could be improved using no prior experimental data.

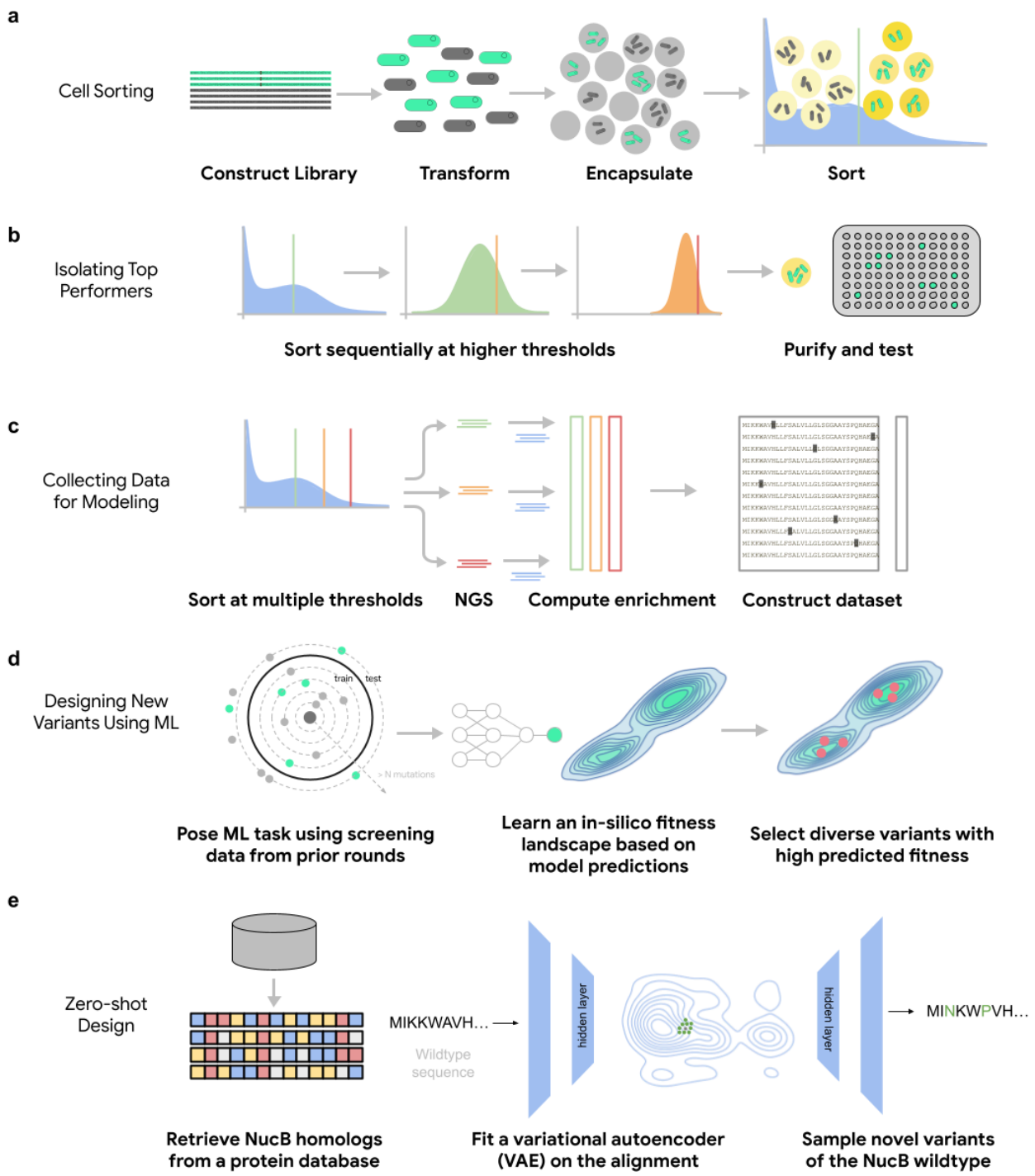

Figure 1: Generation and in vitro screening of variants proposed by ML models trained on screening data. *(a) Experimental workflow for selecting variants with high enzyme activity using a fluorescence-based ultra-high-throughput platform. Cells are encapsulated in droplets as a water-in-oil emulsion and injected with reagents to achieve the desired reaction conditions. Repeatedly sorting a library at different activity thresholds can be used to (b) apply selective pressure to identify top-performing variants and (c) produce a full dataset of genotype-activity pairs. (d) Model-based optimization workflow for designing libraries of novel enzyme variants*

using activity data from prior rounds of experiments. The fitness landscape (non-functional variants in gray, active variants in turquoise) is used for model training and model selection. Optimization on the in-silico landscape then yields a diverse batch predicted to have high fitness. (e) Zero-shot sampling approach for designing an initial library of variants using patterns observed in an alignment of homologous natural sequences.

The **DE**, **ML** and **HR** campaigns were all built upon the same initial library, generated by applying error-prone (epPCR) to a single-site saturation mutagenesis library of the *B. licheniformis* wildtype (WT) NucB sequence (see Supplementary Figure 28). **DE** had access to an initial dataset containing at least 211K distinct epPCR variants, while the higher DNA sequencing read depth required to estimate enzyme activity, based on estimating the enrichment of a variant in the post-sort vs. pre-sort population, meant the initial dataset used for **HR** and **ML** contained just 9.4K distinct variants (see Supplementary Figure 25). The **ZS** library did not require an initial dataset, instead employing 4.6K homologs. The **ML** campaign contained about 10K variants in each round, while **HR** libraries were about 1-2K in size, akin to a large-scale plate-based high-throughput enzyme screening experiment (Supplementary Table 3). Models for **ML** were trained on all **ML** and **HR** data from prior generations.

Machine learning paired with ultra-high-throughput screening designed higher-activity nuclease enzymes than directed evolution

To compare the performance of **ML** to **DE**, we performed a series of downselection assays on each library to isolate the best enzyme variant and then characterized its performance (see Supplemental Figure 7). First, we sorted droplets at a sequence of successively higher thresholds (Figure 1b), and cultured selected cells on agar plates. Those colonies were then assessed for nuclease activity in liquid culture plates. Finally, top-performing strains in the liquid culture plate assay were purified and promoted to a specific activity assay. The specific activity assay measures the fold-improvement of the kinetic rate of purified enzyme by comparing the temporal fluorescence trajectories of a variant v.s. the wildtype (see Methods: Nuclease activity assays).

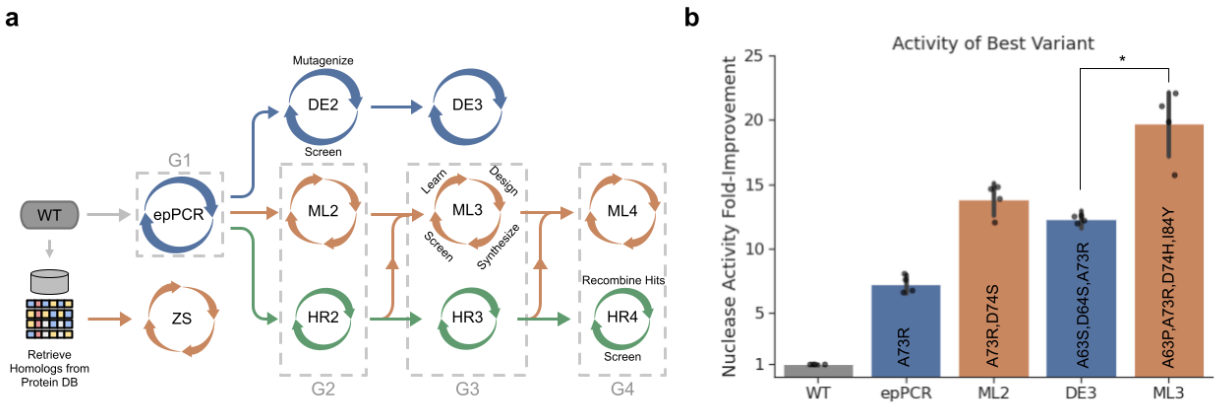

Figure 2: Machine learning paired with ultra-high-throughput screening designed a higher-activity nuclease enzyme than directed evolution using the same screening platform: *(a) We ran parallel enzyme optimization campaigns using traditional directed evolution (DE, blue), ML-guided design (ML, orange), and hit recombination (HR, green), where all were initialized from the same error-prone PCR variant library (epPCR, G1), in which about 11% of the variants were functional and 2% had activity higher than the wildtype. As denoted by the dashed lines, ML and HR libraries were pooled during synthesis and screening. We additionally ran a single round screen of a zero-shot designed library (ZS), designed by a model fit using homologous sequences. (b) Top-performing variants from each library were purified and assessed for nuclease activity at four enzyme concentrations, normalized by the WT activity. The best variant discovered after 2 rounds of ML guided design (ML3, orange) had significantly better activity than the best variant discovered after 2 rounds of directed evolution (DE3, blue, permutation test; $p < 0.05$). Error bars indicate ± 1 standard deviation, which accounts for variability across enzyme concentrations and variability in kinetic rate estimation (see Supplementary Figure 14 for details on the estimate of standard deviation*).

Figure 2b shows that the best enzyme discovered by two rounds of ML-guided design (**ML3**, orange) significantly outperforms the best enzyme discovered using two rounds of DE (**DE3**, blue; permutation test, p=0.014). The best **ML2** and **ML3** variants were proposed by model-based optimization on a learned neural network landscape (MBO-DNN, see Methods). After three generations, comprising ~23K variants, **ML3** discovered (A63P, A73R, D74H, I84Y), with a 19 fold-improved activity that outperforms the best **DE3** enzyme (A63S, D64S, A73R), with a 12 fold-improved activity at pH 7. Both exceeded our goal of restoring the activity level to that of the WT NucB at its optimal pH 9: the **ML3** enzyme showed 2.4 fold-improved activity, while the best **DE3** variant showed 1.5 fold-improved activity (see Supplementary Figure 16). Since the ML and HR libraries were pooled in each round and our stringent selection process isolated only the top variants, the fact that no **HR** proteins were selected for purification suggests that **HR** did not discover any variants with activity comparable to the best from **ML3** and **DE3**. We did not purify any variants from **DE2**, as the DE campaign was run independently with the goal of characterizing the overall highest-activity variant.

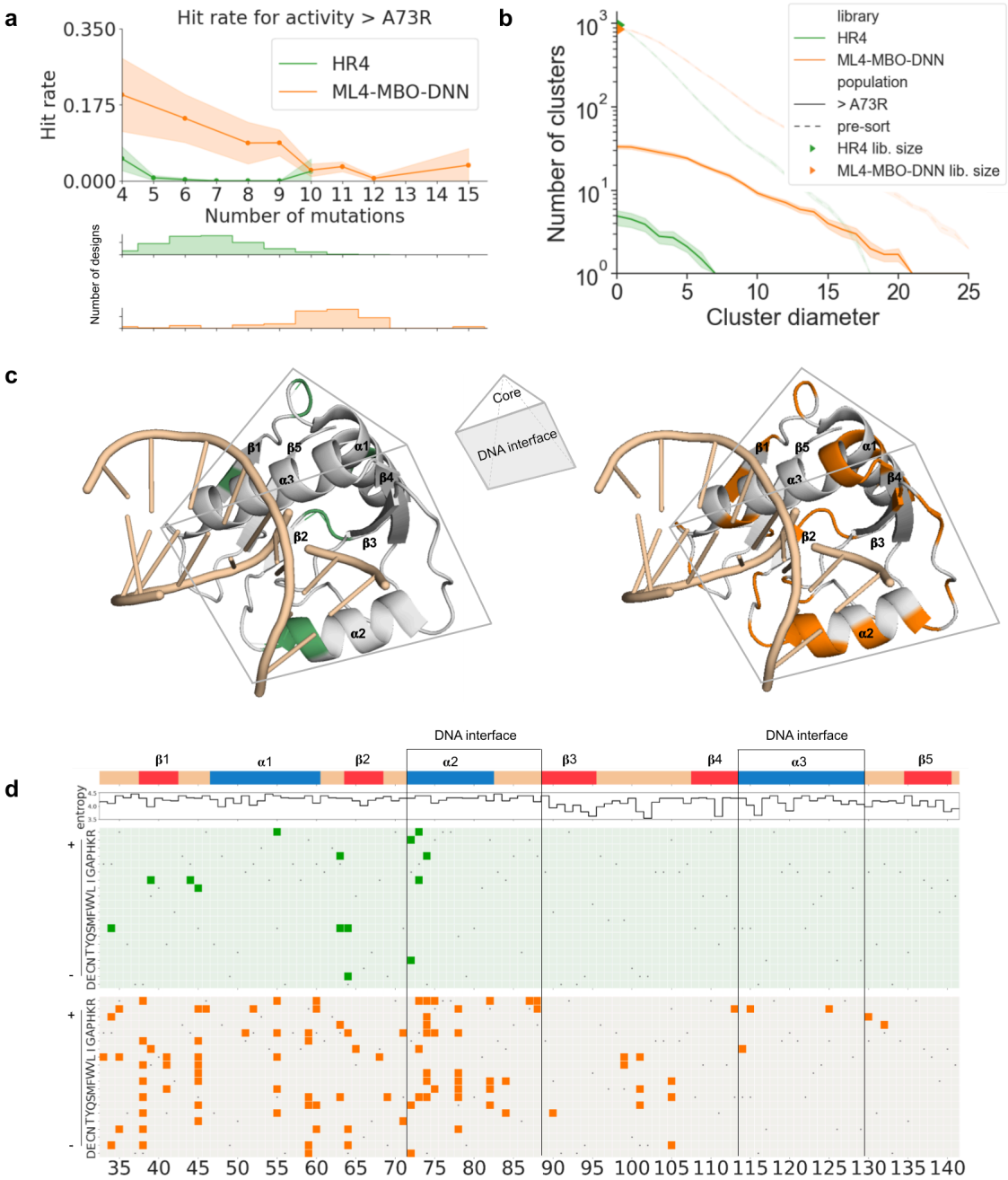

Figure 3: Pooled screening of ML-designed libraries alongside non-ML libraries reveals the significance of our method's improvement to hit rates and diversity. *(a) In G4, our MBO-DNN sequence design technique (ML4-MBO-DNN, orange) has a far higher hit rate than hit-recombination (HR4, green) for improving activity above the level of A73R, the best variant observed in the epPCR data. Notably, we are able to extend designs out to 15 mutations from the NucB wildtype, while still exceeding this threshold. (b) Clustering the hits by sequence similarity reveals that active ML4-MBO-DNN designs (solid orange) were substantially more diverse than active HR4 designs (solid green). The diversity of active designs was driven by both the improved hit-rate of ML4-MBO-DNN compared to HR4 and the diversity of the*

designed library prior to sorting (dotted lines). The cluster diameter is defined as the maximum Hamming distance between two sequences in the same cluster. (c) Three-dimensional model of NucB (PDB ID: 5OMT) with DNA based on the structural homology with Vvn endonuclease (PDB ID: 1OUP) as described in Baslè, et al.[110]*. NucB forms a square pyramid structure with a positively charged DNA binding interface and a negatively charged core. Mutations found in the HR4 and ML4-MBO-DNN designs are highlighted on the structure in green (left) and orange (right), respectively. (d) NucB secondary structure, per-position Shannon entropy, and mutations identified by the HR (green) and ML (orange) campaigns. The 52 highly-active nucleases designed by ML exhibited mutations that span more diverse positions (orange) in the amino acid sequence than 9 HR hits (green). Amino acids are ordered by increasing isoelectric point (pI). Wildtype residues are indicated in gray.*

We designed a follow-up screening to more closely mimic a clinical application, where we assessed biofilm disruption by culturing *Bacillus licheniformis,* which produces biofilm naturally, and exposing biofilm to the enzyme (see Supp. S6C). We found that the best **ML3** variant degraded *B. licheniformis* biofilms more effectively than the wildtype enzyme. At 1-μM enzyme concentration, the **ML3** variant degraded 71 ± 2% of the biofilm compared to 13 ± 3% degraded by the wildtype (t-test, $p < 1e-15$; see Supplementary Figure 15).

Machine learning discovered hundreds of diverse hits with high activity

Over three rounds of our campaign, we achieved two key goals: we improved enzyme activity at pH 7 beyond the WT activity at pH 9 and we demonstrated that **ML** did so better than **DE**. To further investigate the capabilities of ML-guided campaigns, we developed a fourth round of designs (**ML4**) with the goal of finding *diverse*, high-activity hits. Maintaining additional diversity over directed evolution is one of the key promises of ML-guided design[30]. Most design campaigns require optimizing over multiple objectives, such as expression, toxicity, and stability. Increasing the diversity of designs without sacrificing performance can increase the chance that a variant meets the requirements for additional properties in downstream screens. Evaluating **ML** performance in terms of diversity relies on characterizing enzyme activity for a large sample of the variants in parallel, and we enabled a head-to-head comparison against **HR**, a non-ML baseline, by pooling the **ML** and **HR** designs in each round (Fig 2A). We compare designed libraries in terms of both the 'hit-rate', the proportion of variants with activity above a given activity threshold, and the 'diversity', measured as the number of clusters of hits when clustered at a given sequence identity threshold.

To characterize hits at high-throughput, we sequence both the pre-sort and post-sort libraries (Figure 1c), compute an enrichment factor for each variant, and compare this with the empirical distribution of enrichment factors for synonymous variants of a *fiducial* reference enzyme with known activity (see Methods). A variant is labeled as more active than the fiducial using a right-sided t-test, and we estimate the hit rate of a collection of variants using a Benjamini-Hochberg[51] correction with an expected false discovery rate of 0.1 to account for multiple testing. Hit rates for all library design methods in all generations are provided in

Supplementary Table 1. We refer to the pooled experiments containing both **ML** and **HR** libraries, as *generations* G1 to G4 (Figure 2a), where G1 is the initial epPCR library. When analyzing the methods' performance in G4, we consider hit rates with respect to three fiducials of increasing activity: WT, A73R, and A73R,D74S. A73R was the top-performing variant from the initial epPCR library, with 8-fold higher activity than the WT at pH 7 (1.3-fold higher activity than the WT at pH 9). A73R,D74S was the best mutant seen in G2, with 13-fold improved activity (Figure 2b).

ML4-MBO-DNN (Methods) was the strongest-performing member of the portfolio of methods in **ML4** in terms of hit rate (see Supplementary Table 1). It had similar size as **HR4** (1356 vs. 1540 variants) and significantly outperformed **HR4** at finding hits above the A73R level (chi-square test; $P=1.3\times10^{-9}$): 52 ± 7 of the 1356 **ML4-MBO-DNN** variants (hit-rate 3.9% ± 0.5%; standard deviations estimated via bootstrapping) had greater activity than A73R, compared to only 7 ± 4 of the 1540 **HR4** variants (hit-rate 0.5% ± 0.2%). For discovering variants with activity greater than the WT, **ML4-MBO-DNN** significantly outperformed **HR4** (chi-square test; $p < 1e-15$). **ML4-MBO-DNN** found 1145 ± 15 hits out of 1356 designs (hit-rate 84.5% ± 1.1%), while **HR4** found 890 ± 17 hits out of 1540 designs (hit-rate 58.0% ± 0.1%). Finally, **ML4** discovered 31 variants with significantly better activity than A73R,D74S, of which 29 were designed by our MBO-DNN technique (2.2% ± 0.5% hit rate) and 21 had > 9 mutations (Supplementary Table 2). In contrast, **HR4** only discovered two variants better than the best variant in ML2 (0.1 ± 0.1 hit rate) and these each had just 4 mutations.

To quantify diversity for each library, we cluster hits by sequence similarity and count the number of clusters (see Methods). By sweeping over thresholds for the cluster diameter, we found that the **ML4-MBO-DNN** hits were more diverse than those in **HR4**, both for variants with activity higher than A73R (Fig. 3B) and for variants with activity higher than WT (see Supplementary Figure 16). While all 5 **HR4** hits are within 7 mutations of one another, the 52 **ML4-MBO-DNN** hits maintain 10 distinct clusters even when clustering at Hamming distance 10 (cluster diameter = 10, Figure 3b). We also see that there is substantially more diversity in the pre-sort pool (Figure 3b, dotted lines) for **ML4-MBO-DNN** than for **HR4**, though the libraries are approximately the same size with $\sim10^3$ variants. Furthermore, compared to **HR4** hits**,** which focused on 10 positions, **ML4-MBO-DNN** hits placed mutations across 38 positions in the protein, encompassing the DNA interface, all secondary structure domains, and unstructured loops (Figure 3d).

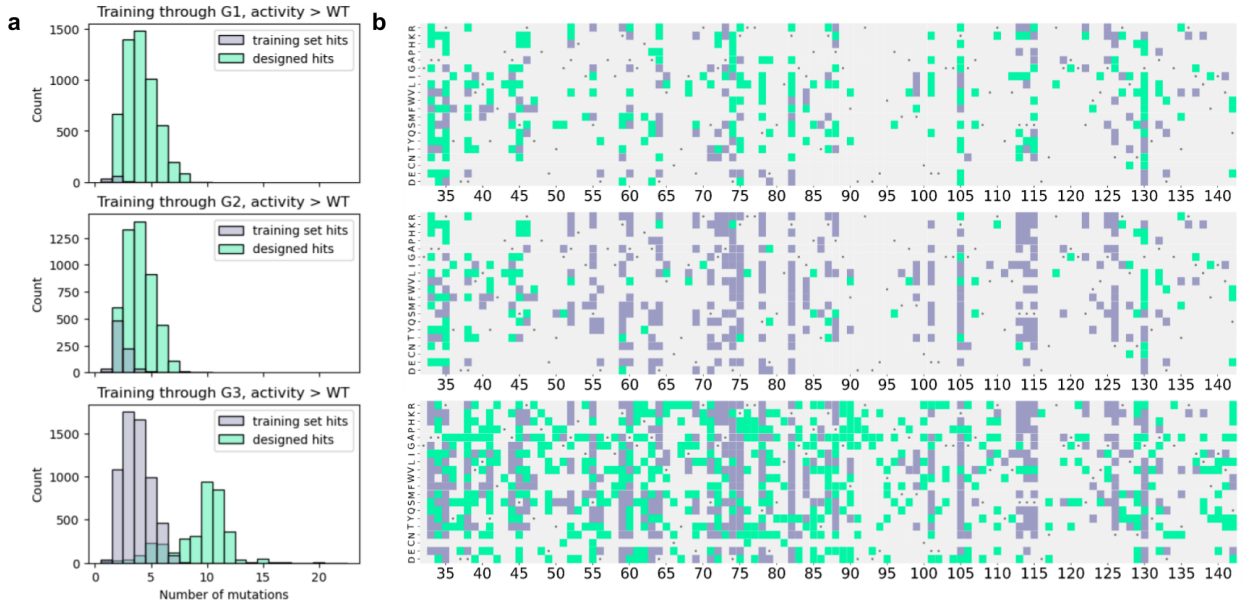

Figure 4: Models designed functional variants that are qualitatively different from the models' training data. *(a) Model-designed variants (green) were active at distances from the wildtype well beyond active variants seen in the training set (purple). In (b) we visualize the distinct mutations present in the hits in the training set and designs. The set of mutations found in active variants included novel mutations extending beyond those seen in training data from prior rounds. By definition, hit recombination is constrained to recombine hits seen in the prior rounds and thus it can not expand the set of mutations beyond the purple mutations in any round. Each row corresponds to models trained on data from a given round, i.e. the first row shows designs from models trained on G1 data (including the 'g2_redux' library screened in parallel with G4), the second row shows designs from models trained on G2 data, and the third row shows designs from models trained on G3 data.*

Machine learning designs revealed the ability of models to extrapolate beyond their training set

In typical directed evolution campaigns, a small number of mutations are incorporated into the protein in each generation[16]. For **HR4**, the distribution of distances from WT is dictated by the top **HR3** hits, while for **ML**, the distribution of distances is an algorithmic choice. To investigate whether our ML techniques can more rapidly traverse the fitness landscape while maintaining or improving activity, we deliberately designed variants that were many mutations beyond the highest activity variants seen in the training data. Because we wanted to test the ability to diversify the target protein, we define hits as having activity greater than WT. In Figure 4a we find that many of these **ML** hits had many more mutations than the hits from prior generations used to train the models. Further, the hits were not simple recombinations of mutations known to be active, but included mutations that had not previously been seen in a variant of the desired activity level (Figure 4b). Prior to G4, no variant with activity greater than WT and > 9 mutations was observed (Figure 4a), and no variant with activity greater than A73R with > 7 mutations was

observed (not shown). Despite this, **ML4** discovered variants with greater activity than A73R with up to 15 mutations, while simultaneously improving over the best activity seen in **ML3**. We also validated two **ML4** hits containing 11 mutations with greater activity than A73R in the liquid culture plate assay (see Supplementary Figure 6.7).

We hypothesized that the extrapolation capabilities of our ML methods depended on models' ability to infer epistasis, or non-additive effects of multiple mutations[52]. Epistasis can be learned from non-additive interactions observed in the experimental data[20,53,54], from correlations between residues in related natural homologs[55–58], or from combining both[59,60]. To better understand which components were important for such extrapolation, we paired our ML-guided libraries with 'ablation' sub-libraries that used the same overall design strategy but relied on an additive model (see Supp. S2). In G3, we generated variants using the PROSAR method[61], which assumes additive mutation effects, and an extension where PROSAR variants were filtered using scores from a non-additive model of nucB homologs. Doing so significantly increased the hit rate for discovering variants with activity higher than A73R from 4.5% ± 2.3% to 23.2% ± 6.2% (see ‘g3_prosar_low_unscreened’ and ‘g3_prosar_high_screen_high’ Supplementary Table 1, Supplementary Figure 3). This suggests that information from the homologs helped remove non-functional recombination variants, perhaps due to the model's non-additivity. Inspired by this result, in G4 we tested whether this semi-supervised learning approach would have added additional value even earlier in the campaign, when experimental data was limited. Our 'g2 redux' library only employed G1 data and had a similar hit rate for discovering functional variants as HR2, while incorporating about twice as many mutations per variant (Supplementary Figure 3). Additional ablations (Supp. S2) investigate the impact of algorithmic choices, such as the algorithm for generating candidates with high model score in MBO-DNN (Supplementary Figure 4)

Zero-shot models improved enzyme activity using no prior experimental data

In a protein optimization campaign, the first round of screening is essential for finding promising directions for further evolution of the target. Typically, the initial library is created using either random mutagenesis (e.g., epPCR) or single-site mutagenesis (SSM). These techniques often lead to a library either with low diversity or containing many non-functional variants, both of which can hinder subsequent optimization rounds based either on ML or directed evolution[63]. To investigate whether we could have generated a better initial library than our G1 library (created using a combination of epPCR and SSM) using ML-based 'zero-shot' sampling (Figure 1e), we ran an additional experiment. We designed variants without using any existing experimental data, instead relying on the conservation patterns observed in natural NucB homologs. We employed a variational autoencoder with fully-connected encoder and decoder based on the DeepSequence model[64], which was fit on a multiple sequence alignment and can both score the likelihood of a given sequence or sample novel sequences.

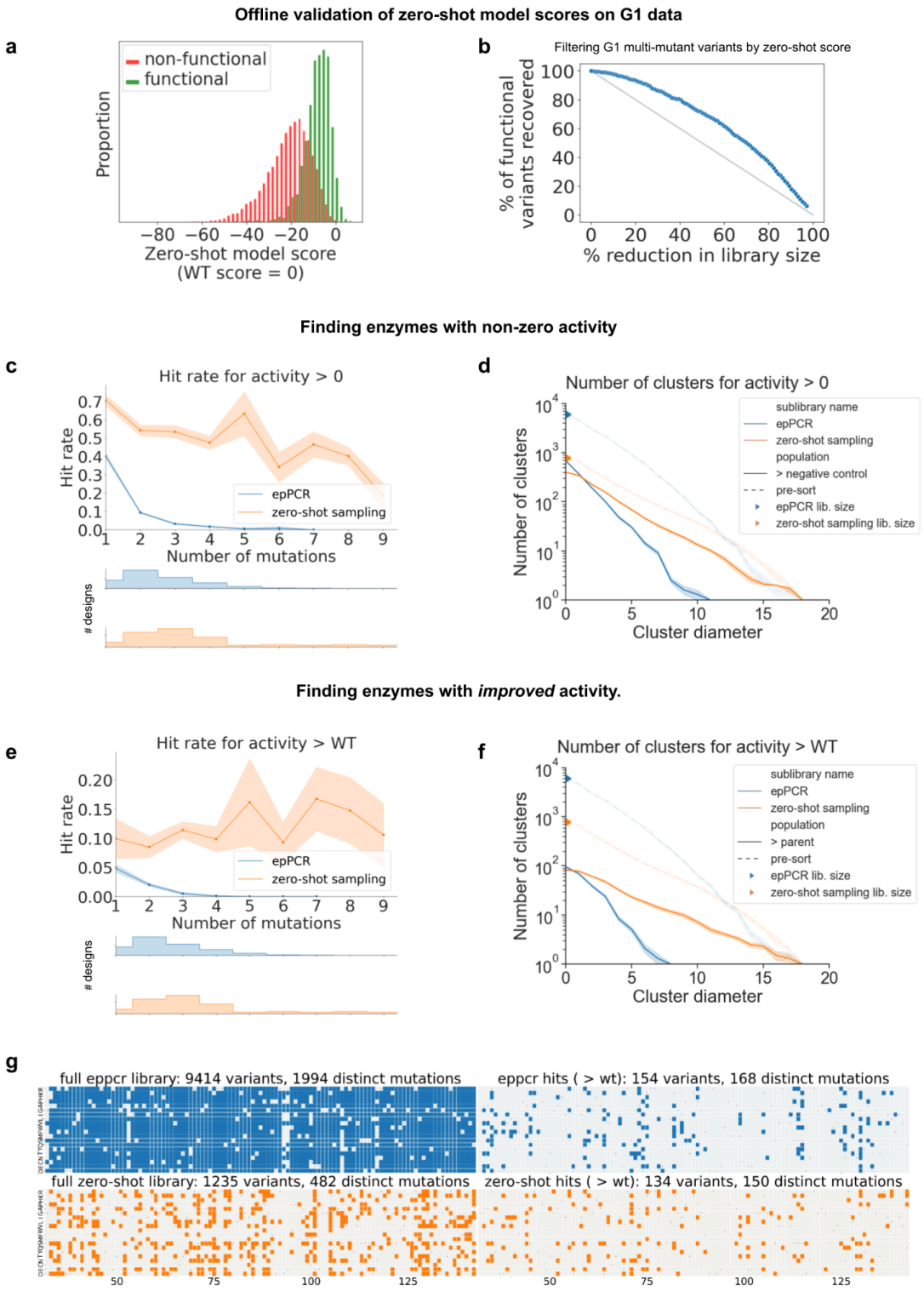

Figure 5: Without any experimental screening data, sampling from a zero-shot model of natural homologs is significantly better than *error-prone PCR (epPCR)* for providing an initial set of diverse hits that maintain and improve NucB function. *(a) We initially validated our zero-shot model by observing that sorting the epPCR library by model score provides*

significant separation between non-functional and functional variants. See Supp. S3 for comparisons to other zero-shot models. (b) Removing the bottom 50% of epPCR by score would only remove about 10% of the functional variants; the gray line represents the performance of random sub-sampling. (c) A significantly higher fraction of the novel variants sampled from the zero-shot model have non-zero activity than epPCR, despite incorporating more mutations per variant and (d) having higher sequence diversity. (e) The sampled library does not simply incorporate neutral mutations; the zero-shot designs also exhibit a much better hit rate for improving activity above the wildtype and (f) these improved hits are diverse. (g) While the zero-shot library was much smaller than epPCR, both in terms of the number of variants and the number of distinct mutations explored, it was able to discover a comparable number of promising mutations appearing in at least one variant with better-than-wildtype activity. The WT residue at each position is indicated by a gray dot.

We decided to investigate zero-shot design after initial analysis on the epPCR data (Figure 5a) demonstrated that sequences with low likelihood under the VAE tended to be non-functional, as observed in prior work for a variety of proteins and models[59,64–70] (Figure 5a). For example, filtering the set of multi-mutant epPCR variants to remove the bottom-scoring 50% would have removed only about 10% of the functional variants (Figure 5b). In Supp. S3, we further show that our model outperforms other popular mutation scoring models including ESM-1b[71] and a profile hidden Markov model[72] at identifying functional variants and better-than-WT variants. Here and below, variants are labeled as functional using the enrichment factors from variants containing premature stop codons to define a null distribution. Note that typically, zero-shot design approaches would not be able to validate the model on experimental data before sampling novel variants. However, our decision to allocate a portion of G4 to zero-shot samples was informed by model performance on scoring G1 variants. Our approach is still zero-shot because we did not tune any VAE parameters or hyper-parameters on experimental NucB data.

We next experimentally characterized the activity of a library of novel variants sampled from the VAE (see Methods) and compared the quantity and diversity of hits to those generated by epPCR in G1. In Figure 5c, we show that the zero-shot technique generates functional variants with significantly better hit rate than epPCR (51.0% ± 1.8% vs. 10.9% ± 0.9%; chi-squared test, $p < 1e\text{-}15$), even when we sampled variants containing many more mutations from the WT than those from epPCR. We also show in Figure 5d that while the diversity of the pre-sort library for epPCR was comparable to that of zero-shot sampling, the diversity of the functional variants from zero-shot sampling was far higher. We find that the rate of negative epistasis[52], here defined as the fraction of non-functional double-mutation variants composed of two mutations that led to a functional variant in isolation (see Methods), was much higher in the error-prone PCR designs (49%; 193 of 392) than in the zero-shot designs (27%; 49 of 181).

In Figure 5e we further demonstrate the zero-shot library's ability to discover variants with activity exceeding the WT. One concern when using a model fit on homologous sequences is that it would suggest mutations with neutral effect on activity, as these may tend to appear at positions with low conservation. However, we find that the zero-shot library has a significantly better hit rate than epPCR for finding variants that improve over the WT (10.9 ± 0.9% vs. 1.6% ±

0.1%; chi-squared test, $p < 1e-15$), even when incorporating many mutations in each variant. These hits are very diverse (Figure 5f), despite the fact that the zero-shot pre-sort library had far fewer variants than G1 (1235 vs. 9441).

Generally, follow-up optimization rounds build upon the initial library. For example, a common strategy is to propose variants that are composed of mutations that occurred in observed high-activity variants[11]. Thus, one measure of the quality of the library is the number of distinct mutations appearing in better-than-wildtype variants. In Figure 5g we find that the number of promising mutations discovered by zero–shot sampling and epPCR was about the same (168 vs. 150), despite the fact that there fewer distinct mutations appear in the zero-shot library (1994) than in epPCR (482). This suggests that zero-shot sampling could be particularly helpful in settings where experimental throughput is limited.

Finally, we further investigated whether a deep neural network is required to extract interesting candidate mutations from an alignment of natural homologs. We characterized a small library designed using a 'homolog grafting' technique (Methods) that incorporates mutations from the homologs in the VAE training data that are most close to the WT and found that it had a similar hit rate to zero-shot sampling but was able to generate far fewer variants (Supp. S3B).

Ultra-high-throughput screening enabled experimental characterization of the genotype-phenotype landscape

We released a 55,760-variant genotype-phenotype dataset containing all data from the **ML** and **HR** campaigns, one of the deepest-explored public enzyme fitness datasets to date. Most existing public landscapes either deeply explore combinations of few positions [20,73,74] or explore single mutants for many positions[75,76]. Our dataset contains all single mutant variants, as well as thousands of multi-mutant combinations, many of which are active. Our dataset contains significantly more active variants (Figure 6a) than the randomly-collected epPCR data (Figure 6b), and many of the active variants have at least 10 mutations from the WT (Figure 6b). See Methods for how activity labels were derived. Since most of the variants come from the trajectories of particular optimization techniques, their properties are qualitatively different from those of randomly-collected mutants. For example, the rate of negative epistasis (i.e. double mutants AB, where both A and B result in a functional variant in isolation but AB is non-functional), is 49% (193 of 392) in the epPCR dataset but only 20% (883 of 4416) in the overall dataset, which demonstrates that our techniques effectively navigated around 'holes' in the landscape[63]. We hope our dataset will drive the development of ML methods that can perform even better extrapolation.

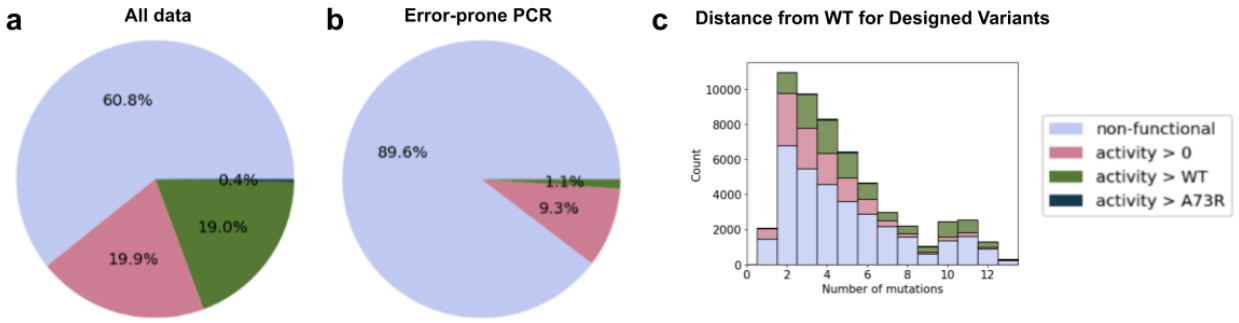

Figure 6: Overview of the genotype-phenotype landscape. *(a) The overall dataset, consisting of designed variants and error-prone PCR variants, provides many representatives across a broad range of activity levels. (b) The error-prone PCR dataset is more imbalanced. (c) The overall dataset contains many functional variants and variants with activity > WT that are far from the WT (x-axis clipped to show a maximum of 13 mutations).*

Discussion

Using the combination of ML-guided sequence design and an ultra-high-throughput microfluidic screening platform, we discovered a novel NucB variant with 19x better specific activity at pH 7 than the NucB wildtype, unlocking a key requirement for using the enzyme to degrade chronic wound biofilms at physiological pH. Analysis of our high-throughput data further suggests that we found a large number of diverse variants with activity greater than A73R, i.e. more than 8x better than the wildtype. Importantly, our ML campaign outperformed two directed evolution approaches that used the same platform: one that was run independently and using standard *in-vitro* techniques for hit selection and diversification and one that was pooled with the ML-designed libraries for screening. Finally, we showed that sampling from a zero-shot model provides advantages over error-prone PCR for designing active initial libraries.

As data accumulated, our design approach transitioned from depending on prior knowledge (e.g., from conservation in natural homologs) to exploiting non-additive patterns appearing in the observed experimental data. We also found that including multiple sub-libraries using different design strategies (Supplementary Table 1) allowed us to hedge against unclear choices, such as how much to trade off average model score vs. sequence diversity in a batch of variants. Additionally, we found that non-linear models strongly outperformed linear models when approximating the fitness landscape (Supp. S4), though the appropriate type of non-linear model to use is an active area of study[54,77,78]. We hope that our fitness landscape dataset will contribute to the development of improved methods for protein fitness prediction[53,76].

A key question is whether our ML-based design approach would work in settings with lower-throughput experiments. Our MBO-DNN system fit a neural network from scratch on the observed experimental data, with no prior knowledge about the relationship between protein sequence and function. In lower-throughput settings, accurate modeling may require using models with prior knowledge derived from physics[79], natural evolution[59,60], or experimental observations from related campaigns[80,81]. Alternatively, one could redefine the search space of

the protein optimization problem by using samples from protein language models[70,71,82–86], or fragment recombination[35–37] to create a pool of diverse, realistic candidates for in-silico screening. This provides safeguards against under-fit models that predict high activity for non-viable protein sequences.

Further, our ML campaign introduced additional costs and complexity beyond traditional DE, mainly from the DNA sequencing required to create a genotype-phenotype dataset and the synthesis of large pools of explicit DNA sequences. The continually-decreasing costs of synthetic biology workflows will continue to mitigate this difference. However, it may be fruitful to more carefully balance the cost of DNA synthesis with the level of control it provides. In early rounds of experiments, for example, it would have been interesting to employ ML to design random combinatorial libraries, which are significantly cheaper to assemble[38,87–94]. For a given budget, improvements to assays[95] and enrichment factor estimation[96] can also help improve the quality of datasets produced by sorting-based experiments.

The performance of our zero-shot library contributes to a growing body of evidence showing that samples from models fit on natural sequences can be used to generate libraries that are not only enriched for functional variants[82,97,98] but also contain variants with *improved* fitness[42,59,99–105], even though the zero-shot sampling process did not take the target phenotype of the engineering campaign into account. We encourage further exploration of these techniques for initial library design[63,106], particularly in lower-throughput settings where improving hit rates can increase the chance of finding at least one satisfactory variant (Figure 5b). Note that this approach is distinct from advancements in ML-based de-novo protein design[107–109], which can be used to design proteins with novel function, while our approach samples variants of a parent sequence in order to enhance a known function.

Our techniques are not specific to nucleases, and can be extended naturally to other proteins with available natural homologs and to fitness functions where high-throughput assays are practical. Going forward, we expect that ML methods for protein optimization will become increasingly standardized and target-agnostic. However, creating genotype-phenotype datasets will continue to require significant application-specific assay development. For example, our microfluidics approach relied on our ability to tie enzyme activity to fluorescence, which may not be straightforward for other protein functions. Overall, as advancements in synthetic biology allow us to screen a wider variety of functions with higher throughput, and computational advancements make models more data-efficient, we expect machine learning to dramatically reduce the amount of time it takes to go from an initial target to an optimized protein for many desired functions.

References

1. Eijsink, V. G. H., Gåseidnes, S., Borchert, T. V. & van den Burg, B. Directed evolution of enzyme stability. *Biomol. Eng.* **22**, 21–30 (2005).
2. Cabantous, S., Terwilliger, T. C. & Waldo, G. S. Protein tagging and detection with engineered self-assembling fragments of green fluorescent protein. *Nat. Biotechnol.* **23**, 102–107 (2005).
3. Pédelacq, J.-D., Cabantous, S., Tran, T., Terwilliger, T. C. & Waldo, G. S. Engineering and characterization of a superfolder green fluorescent protein. *Nat. Biotechnol.* **24**, 79–88 (2006).
4. Bornscheuer, U. T. *et al.* Engineering the third wave of biocatalysis. *Nature* **485**, 185–194 (2012).
5. Bartel, M. A., Weinstein, J. R. & Schaffer, D. V. Directed evolution of novel adeno-associated viruses for therapeutic gene delivery. *Gene Ther.* **19**, 694–700 (2012).
6. Lu, R.-M. *et al.* Development of therapeutic antibodies for the treatment of diseases. *J. Biomed. Sci.* **27**, 1 (2020).
7. Arnold, F. H. Directed Evolution: Bringing New Chemistry to Life. *Angew. Chem. Int. Ed Engl.* **57**, 4143–4148 (2018).
8. Sinai, S. & Kelsic, E. D. A primer on model-guided exploration of fitness landscapes for biological sequence design. *arXiv [q-bio.QM]* (2020).
9. Johnston, K. E. *et al.* Machine Learning for Protein Engineering. *arXiv [q-bio.BM]* (2023).
10. Boder, E. T., Midelfort, K. S. & Wittrup, K. D. Directed evolution of antibody fragments with monovalent femtomolar antigen-binding affinity. *Proc. Natl. Acad. Sci. U. S. A.* **97**, 10701–10705 (2000).
11. McIntosh, J. A. *et al.* Engineered Ribosyl-1-Kinase Enables Concise Synthesis of Molnupiravir, an Antiviral for COVID-19. *ACS Cent. Sci.* (2021)

doi:10.1021/acscentsci.1c00608.

12. Giver, L., Gershenson, A., Freskgard, P. O. & Arnold, F. H. Directed evolution of a thermostable esterase. *Proc. Natl. Acad. Sci. U. S. A.* **95**, 12809–12813 (1998).
13. Reetz, M. T. & Carballeira, J. D. Iterative saturation mutagenesis (ISM) for rapid directed evolution of functional enzymes. *Nat. Protoc.* **2**, 891–903 (2007).
14. Carballeira, J. D. *et al.* Directed evolution and axial chirality: optimization of the enantioselectivity of Pseudomonas aeruginosa lipase towards the kinetic resolution of a racemic allene. *Chem. Commun.* 1913–1915 (2007).
15. Romero, P. A. & Arnold, F. H. Exploring protein fitness landscapes by directed evolution. *Nat. Rev. Mol. Cell Biol.* **10**, 866–876 (2009).
16. Tracewell, C. A. & Arnold, F. H. Directed enzyme evolution: climbing fitness peaks one amino acid at a time. *Curr. Opin. Chem. Biol.* **13**, 3–9 (2009).
17. Packer, M. S. & Liu, D. R. Methods for the directed evolution of proteins. *Nat. Rev. Genet.* **16**, 379–394 (2015).
18. Wang, Y. *et al.* Directed Evolution: Methodologies and Applications. *Chem. Rev.* **121**, 12384–12444 (2021).
19. Zeymer, C. & Hilvert, D. Directed Evolution of Protein Catalysts. *Annu. Rev. Biochem.* **87**, 131–157 (2018).
20. Wu, N. C., Dai, L., Olson, C. A., Lloyd-Smith, J. O. & Sun, R. Adaptation in protein fitness landscapes is facilitated by indirect paths. *Elife* **5**, (2016).
21. Rapp, J. T., Bremer, B. J. & Romero, P. A. Self-driving laboratories to autonomously navigate the protein fitness landscape. *Nature Chemical Engineering* **1**, 97–107 (2024).
22. Agresti, J. J. *et al.* Ultrahigh-throughput screening in drop-based microfluidics for directed evolution. *Proc. Natl. Acad. Sci. U. S. A.* **107**, 4004–4009 (2010).
23. Markin, C. J. *et al.* Revealing enzyme functional architecture via high-throughput microfluidic enzyme kinetics. *Science* **373**, (2021).

24. Griffiths, A. D. *et al.* Isolation of high affinity human antibodies directly from large synthetic repertoires. *EMBO J.* **13**, 3245–3260 (1994).
25. Fowler, D. M. *et al.* High-resolution mapping of protein sequence-function relationships. *Nat. Methods* **7**, 741–746 (2010).
26. Ravikumar, A., Arzumanyan, G. A., Obadi, M. K. A., Javanpour, A. A. & Liu, C. C. Scalable, Continuous Evolution of Genes at Mutation Rates above Genomic Error Thresholds. *Cell* **175**, 1946–1957.e13 (2018).
27. Kinney, J. B. & McCandlish, D. M. Massively Parallel Assays and Quantitative Sequence-Function Relationships. *Annu. Rev. Genomics Hum. Genet.* **20**, 99–127 (2019).
28. Esvelt, K. M., Carlson, J. C. & Liu, D. R. A system for the continuous directed evolution of biomolecules. *Nature* **472**, 499–503 (2011).
29. Morrison, M. S., Podracky, C. J. & Liu, D. R. The developing toolkit of continuous directed evolution. *Nat. Chem. Biol.* **16**, 610–619 (2020).
30. Yang, K. K., Wu, Z. & Arnold, F. H. Machine-learning-guided directed evolution for protein engineering. *Nat. Methods* **16**, 687–694 (2019).
31. Markus, B. *et al.* Accelerating Biocatalysis Discovery with Machine Learning: A Paradigm Shift in Enzyme Engineering, Discovery, and Design. *ACS Catal.* **13**, 14454–14469 (2023).
32. Ruffolo, J. A. & Madani, A. Designing proteins with language models. *Nat. Biotechnol.* 1–3 (2024).
33. Hsu, C., Fannjiang, C. & Listgarten, J. Generative models for protein structures and sequences. *Nat. Biotechnol.* 1–4 (2024).
34. Notin, P., Rollins, N., Gal, Y., Sander, C. & Marks, D. Machine learning for functional protein design. *Nat. Biotechnol.* **42**, 216–228 (2024).
35. Romero, P. A., Krause, A. & Arnold, F. H. Navigating the protein fitness landscape with Gaussian processes. *Proc. Natl. Acad. Sci. U. S. A.* **110**, E193–201 (2013).
36. Bedbrook, C. N., Yang, K. K., Rice, A. J., Gradinaru, V. & Arnold, F. H. Machine learning to

design integral membrane channelrhodopsins for efficient eukaryotic expression and plasma membrane localization. *PLoS Comput. Biol.* **13**, e1005786 (2017).

37. Greenhalgh, J. C., Fahlberg, S. A., Pfleger, B. F. & Romero, P. A. Machine learning-guided acyl-ACP reductase engineering for improved in vivo fatty alcohol production. *Nat. Commun.* **12**, 5825 (2021).
38. Bedbrook, C. N. *et al.* Machine learning-guided channelrhodopsin engineering enables minimally invasive optogenetics. *Nat. Methods* **16**, 1176–1184 (2019).
39. Biswas, S., Khimulya, G., Alley, E. C., Esvelt, K. M. & Church, G. M. Low-N protein engineering with data-efficient deep learning. *Nat. Methods* **18**, 389–396 (2021).
40. Lu, H. *et al.* Machine learning-aided engineering of hydrolases for PET depolymerization. *Nature* **604**, 662–667 (2022).
41. Zhu, D. *et al.* Optimal trade-off control in machine learning-based library design, with application to adeno-associated virus (AAV) for gene therapy. Preprint at https://www.biorxiv.org/content/10.1101/2021.11.02.467003v2 (2021).
42. Hie, B. L. *et al.* Efficient evolution of human antibodies from general protein language models. *Nat. Biotechnol.* (2023) doi:10.1038/s41587-023-01763-2.
43. Bryant, D. H. *et al.* Deep diversification of an AAV capsid protein by machine learning. *Nat. Biotechnol.* (2021) doi:10.1038/s41587-020-00793-4.
44. Shakir, A., Elbadawey, M. R., Shields, R. C., Jakubovics, N. S. & Burgess, J. G. Removal of biofilms from tracheoesophageal speech valves using a novel marine microbial deoxyribonuclease. *Otolaryngol. Head Neck Surg.* **147**, 509–514 (2012).
45. Shields, R. C. *et al.* Efficacy of a marine bacterial nuclease against biofilm forming microorganisms isolated from chronic rhinosinusitis. *PLoS One* **8**, e55339 (2013).
46. Rostami, N. *et al.* A Critical Role for Extracellular DNA in Dental Plaque Formation. *J. Dent. Res.* **96**, 208–216 (2017).
47. Burgess, J. G., Hall, M. J. & Nijland, R. Compounds and methods for biofilm disruption and

prevention. *US Patent* (2017).

48. Nijland, R., Hall, M. J. & Burgess, J. G. Dispersal of biofilms by secreted, matrix degrading, bacterial DNase. *PLoS One* **5**, e15668 (2010).
49. Whitchurch, C. B., Tolker-Nielsen, T., Ragas, P. C. & Mattick, J. S. Extracellular DNA required for bacterial biofilm formation. *Science* **295**, 1487 (2002).
50. Sim, P., Strudwick, X. L., Song, Y., Cowin, A. J. & Garg, S. Influence of Acidic pH on Wound Healing In Vivo: A Novel Perspective for Wound Treatment. *Int. J. Mol. Sci.* **23**, (2022).
51. Benjamini, Y. & Hochberg, Y. Controlling the False Discovery Rate: A Practical and Powerful Approach to Multiple Testing. *J. R. Stat. Soc. Series B Stat. Methodol.* **57**, 289–300 (1995).
52. Kryazhimskiy, S., Draghi, J. A. & Plotkin, J. B. Evolution. In evolution, the sum is less than its parts. *Science* vol. 332 1160–1161 (2011).
53. Pokusaeva, V. O. *et al.* An experimental assay of the interactions of amino acids from orthologous sequences shaping a complex fitness landscape. *PLoS Genet.* **15**, e1008079 (2019).
54. Otwinowski, J., McCandlish, D. M. & Plotkin, J. B. Inferring the shape of global epistasis. *Proc. Natl. Acad. Sci. U. S. A.* **115**, E7550–E7558 (2018).
55. Marks, D. S. *et al.* Protein 3D structure computed from evolutionary sequence variation. *PLoS One* **6**, e28766 (2011).
56. Morcos, F. *et al.* Direct-coupling analysis of residue coevolution captures native contacts across many protein families. *Proc. Natl. Acad. Sci. U. S. A.* **108**, E1293–301 (2011).
57. Figliuzzi, M., Barrat-Charlaix, P. & Weigt, M. How Pairwise Coevolutionary Models Capture the Collective Residue Variability in Proteins? *Mol. Biol. Evol.* **35**, 1018–1027 (2018).
58. Kamisetty, H., Ovchinnikov, S. & Baker, D. Assessing the utility of coevolution-based residue-residue contact predictions in a sequence- and structure-rich era. *Proc. Natl. Acad. Sci. U. S. A.* **110**, 15674–15679 (2013).

59. Russ, W. P. *et al.* An evolution-based model for designing chorismate mutase enzymes. *Science* **369**, 440–445 (2020).

60. Hsu, C., Nisonoff, H., Fannjiang, C. & Listgarten, J. Learning protein fitness models from evolutionary and assay-labeled data. *Nat. Biotechnol.* (2022) doi:10.1038/s41587-021-01146-5.

61. Fox, R. J. *et al.* Improving catalytic function by ProSAR-driven enzyme evolution. *Nat. Biotechnol.* **25**, 338–344 (2007).

62. Wilson, D. S. & Keefe, A. D. Random mutagenesis by PCR. *Curr. Protoc. Mol. Biol.* **Chapter 8**, Unit8.3 (2001).

63. Wittmann, B. J., Yue, Y. & Arnold, F. H. Informed training set design enables efficient machine learning-assisted directed protein evolution. *Cell Syst* (2021) doi:10.1016/j.cels.2021.07.008.

64. Riesselman, A. J., Ingraham, J. B. & Marks, D. S. Deep generative models of genetic variation capture the effects of mutations. *Nat. Methods* **15**, 816–822 (2018).

65. Ng, P. C. & Henikoff, S. SIFT: Predicting amino acid changes that affect protein function. *Nucleic Acids Res.* **31**, 3812–3814 (2003).

66. Shihab, H. A. *et al.* Predicting the functional, molecular, and phenotypic consequences of amino acid substitutions using hidden Markov models. *Hum. Mutat.* **34**, 57–65 (2013).

67. Hopf, T. A. *et al.* Mutation effects predicted from sequence co-variation. *Nat. Biotechnol.* **35**, 128–135 (2017).

68. Meier, J. *et al.* Language models enable zero-shot prediction of the effects of mutations on protein function. *Adv. Neural Inf. Process. Syst.* **34**, (2021).

69. Rao, R. M. *et al.* MSA Transformer. in *Proceedings of the 38th International Conference on Machine Learning* (eds. Meila, M. & Zhang, T.) vol. 139 8844–8856 (PMLR, 2021).

70. Notin, P. *et al.* Tranception: Protein Fitness Prediction with Autoregressive Transformers and Inference-time Retrieval. **162**, 16990–17017 (17--23 Jul 2022).

71. Rives, A. *et al.* Biological structure and function emerge from scaling unsupervised learning to 250 million protein sequences. Preprint at https://www.pnas.org/content/118/15/e2016239118 (2021).
72. HMMER. http://hmmer.org/.
73. Olson, C. A., Wu, N. C. & Sun, R. A comprehensive biophysical description of pairwise epistasis throughout an entire protein domain. *Curr. Biol.* **24**, 2643–2651 (2014).
74. Papkou, A., Garcia-Pastor, L., Escudero, J. A. & Wagner, A. A rugged yet easily navigable fitness landscape. *Science* **382**, (2023).
75. Esposito, D. *et al.* MaveDB: an open-source platform to distribute and interpret data from multiplexed assays of variant effect. *Genome Biol.* **20**, 223 (2019).
76. Notin, P. *et al.* ProteinGym: Large-Scale Benchmarks for Protein Design and Fitness Prediction. *bioRxiv* 2023.12.07.570727 (2023) doi:10.1101/2023.12.07.570727.
77. Park, Y., Metzger, B. P. H. & Thornton, J. W. The simplicity of protein sequence-function relationships. *bioRxiv* (2023) doi:10.1101/2023.09.02.556057.
78. Aghazadeh, A. *et al.* Epistatic Net allows the sparse spectral regularization of deep neural networks for inferring fitness functions. *Nat. Commun.* **12**, 5225 (2021).
79. Nisonoff, H., Wang, Y. & Listgarten, J. Coherent Blending of Biophysics-Based Knowledge with Bayesian Neural Networks for Robust Protein Property Prediction. *ACS Synth. Biol.* **12**, 3242–3251 (2023).
80. Angermueller, C. *et al.* High-throughput ML-guided design of diverse single-domain antibodies against SARS-CoV-2. *bioRxiv* 2023.12.01.569227 (2023) doi:10.1101/2023.12.01.569227.
81. Zhou, Z. *et al.* Enhancing the efficiency of protein language models with minimal wet-lab data through few-shot learning. *arXiv [q-bio.BM]* (2024).
82. Madani, A. *et al.* Large language models generate functional protein sequences across diverse families. *Nat. Biotechnol.* 1–8 (2023).

83. Bepler, T. & Berger, B. Learning the protein language: Evolution, structure, and function. *Cell Syst.* **12**, 654–669.e3 (2021).

84. Elnaggar, A. *et al.* ProtTrans: Toward Understanding the Language of Life Through Self-Supervised Learning. *IEEE Trans. Pattern Anal. Mach. Intell.* **44**, 7112–7127 (2022).

85. Ferruz, N., Schmidt, S. & Höcker, B. ProtGPT2 is a deep unsupervised language model for protein design. *Nat. Commun.* **13**, 4348 (2022).

86. Hsu, C. *et al.* Learning inverse folding from millions of predicted structures. in *Proceedings of the 39th International Conference on Machine Learning* (eds. Chaudhuri, K. et al.) vol. 162 8946–8970 (PMLR, 17--23 Jul 2022).

87. Parker, A. S., Griswold, K. E. & Bailey-Kellogg, C. Optimization of combinatorial mutagenesis. *J. Comput. Biol.* **18**, 1743–1756 (2011).

88. Saito, Y. *et al.* Machine-Learning-Guided Mutagenesis for Directed Evolution of Fluorescent Proteins. *ACS Synth. Biol.* **7**, 2014–2022 (2018).

89. Verma, D., Grigoryan, G. & Bailey-Kellogg, C. Pareto Optimization of Combinatorial Mutagenesis Libraries. *IEEE/ACM Trans. Comput. Biol. Bioinform.* **16**, 1143–1153 (2019).

90. Yang, K. K., Chen, Y., Lee, A. & Yue, Y. Batched Stochastic Bayesian Optimization via Combinatorial Constraints Design. *arXiv [cs.LG]* (2019).

91. Wu, Z., Kan, S. B. J., Lewis, R. D., Wittmann, B. J. & Arnold, F. H. Machine learning-assisted directed protein evolution with combinatorial libraries. *Proc. Natl. Acad. Sci. U. S. A.* **116**, 8852–8858 (2019).

92. Hu, R. *et al.* Protein engineering via Bayesian optimization-guided evolutionary algorithm and robotic experiments. *bioRxiv* 2022.08.11.503535 (2022) doi:10.1101/2022.08.11.503535.

93. Weinstein, E. N. *et al.* Optimal Design of Stochastic DNA Synthesis Protocols based on Generative Sequence Models. in *Proceedings of The 25th International Conference on Artificial Intelligence and Statistics* (eds. Camps-Valls, G., Ruiz, F. J. R. & Valera, I.) vol. 151

7450–7482 (PMLR, 28--30 Mar 2022).

94. Weinstein, J. Y. *et al.* Designed active-site library reveals thousands of functional GFP variants. *Nat. Commun.* **14**, 1–13 (2023).

95. Trippe, B. L. *et al.* Randomized gates eliminate bias in sort‐seq assays. *Protein Sci.* **31**, (2022).

96. Busia, A. & Listgarten, J. MBE: model-based enrichment estimation and prediction for differential sequencing data. *Genome Biol.* **24**, 1–32 (2023).

97. Repecka, D. *et al.* Expanding functional protein sequence spaces using generative adversarial networks. *Nature Machine Intelligence* 1–10 (2021).

98. Praljak, N., Lian, X., Ranganathan, R. & Ferguson, A. L. ProtWave-VAE: Integrating Autoregressive Sampling with Latent-Based Inference for Data-Driven Protein Design. *ACS Synth. Biol.* **12**, 3544–3561 (2023).

99. Hawkins-Hooker, A. *et al.* Generating functional protein variants with variational autoencoders. *PLoS Comput. Biol.* **17**, e1008736 (2021).

100. Giessel, A. *et al.* Therapeutic enzyme engineering using a generative neural network. *Sci. Rep.* **12**, 1536 (2022).

101. Bachas, S. *et al.* Antibody optimization enabled by artificial intelligence predictions of binding affinity and naturalness. Preprint at https://www.biorxiv.org/content/10.1101/2022.08.16.504181v1.abstract (2022).

102. Xie, W. J. *et al.* Enhancing Luciferase Activity and Stability through Generative Modeling of Natural Enzyme Sequences. *bioRxiv* (2023) doi:10.1101/2023.09.18.558367.

103. Malbranke, C. *et al.* Computational design of novel Cas9 PAM-interacting domains using evolution-based modelling and structural quality assessment. *PLoS Comput. Biol.* **19**, e1011621 (2023).

104. Fram, B. *et al.* Simultaneous enhancement of multiple functional properties using evolution-informed protein design. *bioRxiv* (2023) doi:10.1101/2023.05.09.539914.

105. Sumida, K. H. *et al.* Improving Protein Expression, Stability, and Function with ProteinMPNN. *J. Am. Chem. Soc.* (2024) doi:10.1021/jacs.3c10941.

106. Saito, Y. *et al.* Machine-learning-guided library design cycle for directed evolution of enzymes: the effects of training data composition on sequence space exploration. *bioRxiv* 2021.08.13.456323 (2021) doi:10.1101/2021.08.13.456323.

107. Dauparas, J. *et al.* Robust deep learning-based protein sequence design using ProteinMPNN. *Science* **378**, 49–56 (2022).

108. Watson, J. L. *et al.* De novo design of protein structure and function with RFdiffusion. *Nature* **620**, 1089–1100 (2023).

109. Ingraham, J. B. *et al.* Illuminating protein space with a programmable generative model. *Nature* 1–9 (2023).

110. Baslé, A. *et al.* Crystal structure of NucB, a biofilm-degrading endonuclease. *Nucleic Acids Res.* **46**, 473–484 (2018).

111. Shanehsazzadeh, A., Belanger, D. & Dohan, D. Is Transfer Learning Necessary for Protein Landscape Prediction? *arXiv [q-bio.BM]* (2020).

112. Starr, T. N. & Thornton, J. W. Epistasis in protein evolution. *Protein Sci.* **25**, 1204–1218 (2016).

113. Angermueller, C. *et al.* Population-Based Black-Box Optimization for Biological Sequence Design. *arXiv [cs.LG]* (2020).

114. Kingma, D. P. & Welling, M. An Introduction to Variational Autoencoders. *Foundations and Trends® in Machine Learning* **12**, 307–392 (2019).

115. Remmert, M., Biegert, A., Hauser, A. & Söding, J. HHblits: Lightning-fast iterative protein sequence searching by HMM-HMM alignment. *Nat. Methods* **9**, 173–175 (2012).

116. Brookes, D., Park, H. & Listgarten, J. Conditioning by adaptive sampling for robust design. in *Proceedings of the 36th International Conference on Machine Learning* (eds. Chaudhuri, K. & Salakhutdinov, R.) vol. 97 773–782 (PMLR, 09--15 Jun 2019).

117. Zhao, H., Giver, L., Shao, Z., Affholter, J. A. & Arnold, F. H. Molecular evolution by staggered extension process (StEP) in vitro recombination. *Nat. Biotechnol.* **16**, 258–261 (1998).

118. Codon Usage Database. https://www.kazusa.or.jp/codon/.

119. Li, J. & Makrigiorgos, G. M. COLD-PCR: a new platform for highly improved mutation detection in cancer and genetic testing. *Biochem. Soc. Trans.* **37**, 427–432 (2009).

120. Castillo-Hair, S. M., Fujita, M., Igoshin, O. A. & Tabor, J. J. An Engineered B. subtilis Inducible Promoter System with over 10 000-Fold Dynamic Range. *ACS Synth. Biol.* **8**, 1673–1678 (2019).

121. Zhang, X.-Z. & Zhang, Y.-H. P. Simple, fast and high-efficiency transformation system for directed evolution of cellulase in Bacillus subtilis. *Microb. Biotechnol.* **4**, 98–105 (2011).

122. Abate, A. R., Hung, T., Mary, P., Agresti, J. J. & Weitz, D. A. High-throughput injection with microfluidics using picoinjectors. *Proc. Natl. Acad. Sci. U. S. A.* **107**, 19163–19166 (2010).

123. Michaelis, L. & Menten, M. L. I93 Die Kinetik der Invertinwirkung. *Biochem. Z.*

124. UniProt. https://www.uniprot.org/help/uniref.

125. Pedregosa, F. *et al.* Scikit-learn: Machine Learning in Python. *J. Mach. Learn. Res.* **12**, 2825–2830 (2011).

126. Ke, G. *et al.* LightGBM: a highly efficient gradient boosting decision tree. in *Proceedings of the 31st International Conference on Neural Information Processing Systems* 3149–3157 (Curran Associates Inc., Red Hook, NY, USA, 2017).

127. Abadi, M. *et al.* TensorFlow: Large-Scale Machine Learning on Heterogeneous Distributed Systems. *arXiv [cs.DC]* (2016).

128. Henikoff, S. & Henikoff, J. G. Amino acid substitution matrices from protein blocks. *Proc. Natl. Acad. Sci. U. S. A.* **89**, 10915–10919 (1992).

129. Real, E., Aggarwal, A., Huang, Y. & Le, Q. V. Regularized Evolution for Image Classifier Architecture Search. *AAAI* **33**, 4780–4789 (2019).

130. Bubeck, S. & Cesa-Bianchi, N. Regret Analysis of Stochastic and Nonstochastic Multi-armed Bandit Problems. *Foundations and Trends® in Machine Learning* **5**, 1–122 (2012).

Methods

ML-Based Library Design Approaches

Each round combined multiple sub-libraries corresponding to different ML-based sequence design methods. We summarize the methods here and Supp. S1 provides additional details. Supplementary Table 1 provides a full breakdown of the library size and hit rate of each sub-library.

Model-based optimization with a deep neural network (MBO-DNN):

MBO-DNN fits a sequence-to-function model on the available experimental data and then proposes a library of new variants that have high model scores (Figure 1d). This can be expressed in terms of three stages: model fitting (approximating the sequence-activity mapping), candidate generation (find a large number of sequences with high predicted activity), and batch selection (trimming the candidates to achieve certain diversity criteria).

This section summarizes our G4 MBO-DNN system, which we recommend using once sufficient data has been accumulated from prior rounds, since it provides the most control over library diversity and the most comprehensive exploration of the model's approximate fitness landscape. See Supp. S1 for specific implementation details for our G2, G3, and G4 MBO-DNN systems, which employed the same overall stages as below, but slightly different approaches in each.

Model fitting develops a sequence-to-function model using standard ML methodologies. First, we convert the experimental data into a set of sequences with corresponding discrete enzyme fitness labels. While enzyme activity is a continuous value appropriate for a regression model, we use discrete labels and classification models to avoid needing to account for sigmoidal relationship between enzyme activity and enrichment factor (see 'Obtaining resolution for multiple activity levels' below). We used a convolutional neural network (CNN) classification model due to prior results demonstrating the effectiveness of CNNs on fitness datasets[111]. Since we discretize at multiple activity levels, the model is a multi-class classifier. To tune hyper-parameters of the model, we split the data into train and test sets, and then the final model used to propose new designs was re-trained using the optimal hyper-parameters on the entire dataset. All variants with 2 or fewer mutations are in the train set, and the remainder are reserved for the test set, which allows us to select models that can extrapolate beyond their training data to variants with more mutations. See Supplementary Table 4 for details of the hyper-parameter grid for model selection for the G4 models, including a comparison to linear models and decision trees. The process for the G2 and G3 models was similar. The G4 model uses 3 width-5 convolutional layers with 32 filters each, and a flattening operation to produce a single embedding for the sequence, followed by a fully-connected layer with 64 hidden units, and a final linear output layer, resulting in about 250K total parameters. All non-linearities are ReLUs.

Candidate generation creates a large list (100k+) of variants with high model scores using an approach that can be seen as in-silico directed evolution. We run a randomized local search optimizer with many replicates, where each local search trajectory is either initialized at the WT or a top-scoring variant from previous rounds (see Supp. S1). The optimizer builds up variants one mutation at a time, which enables the search to avoid negative epistasis in the model landscape, but not necessarily discover variants that exhibit positive epistasis[112]. It uses a portfolio of different local search strategies to further improve diversity[113] and constrains the local search to only propose variants within a given radius of the WT. The model score is the predicted log probability of a sequence belonging to the top-scoring discrete activity class.

Batch selection filters the candidates to a smaller final library. We grouped variants by the number of mutations from the WT and selected the top-scoring members of each group, where the number selected per group follows a prescribed distribution of distances from the WT. See "Selecting each sub-library's distribution over distances from the wildtype" below for details. To increase diversity, we clipped model scores such that all variants above some threshold are considered equally attractive within a given group and constrained each mutation to not appear in more than N variants in the library, using a greedy algorithm described in the Supp. S1.

Prosar and extensions

Prosar: We employ the popular method of Fox, et al. [61] with minimal modifications. First, an additive regression model is fit to a dataset of variants to estimate the relationship between a sequence and its observed enrichment factor. Then, the parameters of the model are used to estimate the effect of each possible single-point mutation on enzyme activity. We selected all mutations that were estimated to at least double the enrichment factor of the wildtype, which resulted in approximately 30 mutations, and sampled new variants containing combinations of 2–6 of these. The recombination is performed in-silico, but traditionally it is done in-vitro.

Prosar+Screen: We first generate a large number of recombination variants using Prosar and then select a final library by removing variants with low likelihood scores under the VAE model of natural NucB homologs described in the next section. Since the VAE is trained on diverse homologs, we hoped it would introduce pessimism about combinations of mutations that exhibit negative epistasis[112]. We deployed a few different versions of this library with different exploration-exploitation tradeoffs by varying the model score threshold used for selecting the base set of mutations to combine and the VAE score threshold used for filtering sampled combinations of these mutations.

Zero-Shot Sampling and Scoring

VAE model

The VAE is a latent variable model with latent variable z, a prior distribution P(z), a conditional distribution P(x|z) over amino acid sequence x given by a 'decoder' neural network, and an approximate posterior distribution P(z | x) given by an 'encoder' neural network[64,114]. Our model has fully-connected hidden layers of size 64 and 32 in the encoder and 32 and 64 in the decoder, where z has 32 dimensions, and the total number of parameters is about 400K. It is fit

on an alignment of 4625 homologs obtained by querying the 2020_06 version of UniRef30 using hhblits[115] with an e-value cutoff of 1e-3 and 8 search iterations. Every residue in the WT is designated as belonging to a match state in the alignment, such that the VAE can score mutations to any position.

Zero-shot neighbor sampling: We build on the sampling technique of Giessel, *et al.*[100] for sampling variants of the WT. First, we sample a latent variable from the posterior P(z | WT) and then sample from P(x | z). Any sample with more than 10 substitutions from WT or containing gap characters was rejected, and we revert any mutations appearing outside of the design region. The final library was constructed using the same 'batch selection' approach as above, where a distribution over the number of mutations was specified. Finally, we found that certain mutations appeared in a large fraction of samples, due to these mutations appearing in homologs with high sequence identity to the WT. To avoid over-using these, we expanded our pool of samples to include pseudo-samples where these mutations were reverted. A key advantage of this overall sampling technique is that it provides a principled way to sample variants of a given reference sequence. Unconditional samples from the VAE, or samples from a similar alignment-based method such as a profile HMM, are more diverse than desired.

Zero-shot scoring: Computing the VAE likelihood of a sequence is intractable because it requires marginalizing over latent variable z. We approximate it using importance sampling with 2500 samples, using the approximate posterior provided by the encoder as a proposal distribution. Inspired by the finding in Riesselman, *et al.*[64] that a Bayesian treatment of the neural network parameters improves performance, we average scores across 10 models trained independently with different parameter initialization. In Figure 5a we report the log-likelihood ratio of the variant sequence to the WT, i.e. we subtract the log-likelihood of the WT from all log-likelihood scores. Section Supp. S4 demonstrates that the VAE is either better or comparable to a variety of alternative zero-shot scoring methods on our data.

Alternative Supervised ML Approaches

Supervised neighbor sampling: Inspired by the 'conditioning by adaptive sampling' technique[116], we extend 'zero-shot neighbor sampling' to sample from a model fit on a combination of natural homologs and hits from previous rounds. The sampling technique, model architecture, and batch selection step are the same as above. A key advantage of this approach is that the model is only trained on hits, since avoiding data collection for non-hits can significantly simplify experimental workflows.

Sample and screen: This samples from the 'supervised neighbor sampling' model, assigns samples a score using the model from MBO-DNN (which was trained on both hits and non-hits), and finally uses the same batch selection approach as MBO-DNN. Essentially, this uses VAE sampling to replace the candidate generation step of MBO-DNN based on local search, which may find unrealistic sequences that have high model scores.

Handling multiple design regions

In 'Designed DNA library generation' below we discuss how DNA synthesis required that each *in-silico* design method could only propose variants containing mutations in a single 77-amino-acid design region. For approaches that generate independent samples from a distribution, such as zero-shot sampling, supervised neighbor sampling, and Prosar, we simply ran our code twice, once for each design region and merged the results. Note that our regression and classification models were trained on the entire dataset of variants, and scores are comparable across variants with mutations in either design region. Therefore, for approaches such as MBO-DNN, Prosar+Screen, and 'sample and screen', we generated candidates independently for each design region, but then pooled these together for the sake of batch selection. Since the design regions overlapped, many of the top hits appeared in the overlap; i.e., high-scoring candidates could have been proposed using either design region during candidate generation.

Selecting each sub-library's distribution over distances from the wildtype

In all of the above approaches, we explicitly controlled the sub-library's distribution over variants' distances from the WT, i.e., the number of mutations that they include. This can be seen as treating the ML technique as generating a set of candidates (e.g., by finding sequences with high model score or by sampling from a distribution over sequences defined by the model) and filtering these candidates to achieve a certain distance distribution. These distributions were different for each sub-library and were set heuristically based on our level of confidence in the model's ability to extrapolate.

Non-ML Library Design Approaches

Hit recombination (HR) was used as an *in-silico* approximation to an *in-vitro* directed evolution campaign using recombination to introduce sequence diversity. In each round, we took the top K variants with the highest enrichment factor, generated new variants by combining their mutations additively, and randomly selected a subset of the possible combinations to synthesize, stratified by their distances from the WT. The top K were selected from a pool consisting of those proposed by HR in the previous round or those that were a single mutation away from an HR variant, which mainly arise from DNA synthesis errors. Since we trained our ML models on such variants even though they were not explicitly designed by ML in a prior round, we felt that it was fair to provide HR access to them as well, particularly because the diversity in these variants would have been achievable during in vitro directed evolution.

For each pair of hits, we stacked their mutations into a single novel variant, unless the two hits contained mutations at the same position, in which case we created multiple variants. For example, if hit 1 contained mutations {A1C,T4K} and hit 2 contained mutations {R2A,T4S,K5P}, we created {A1C, R2A, T4S, K5P} and {A1C, R2A, T4K, K5P}. Note that this approach is less flexible than in-vitro recombination techniques that may also generate, for example, {A1C, K5P}. See Supp. FS9 for additional details.

Homolog grafting is used as a baseline for the zero-shot library. We used the same MSA of natural homologs that the VAE was trained on, and inspected it manually to identify promising combinations of mutations. First, we selected the 18 homologs that had fewer than 25 substitutions from the WT, which mostly come from *B. paralicheniformis* and *B. licheniformis* strains. Then, for each homolog we split the mutations into two subsets, based on which of the two design regions they occur in. For each design region, we created a novel set of variants by applying the corresponding set of mutations to the WT.

Broad recombination sampling: Here, we don't use any ML, and instead simply sample combinations of mutations that the available experimental data suggests may be promising. There are two key differences between this and 'hit recombination': we combine a larger footprint of mutations and we combine individual mutations, not groups of mutations that co-occur in known hits. First, we labeled variants as functional or not, using an enrichment factor threshold obtained by visually inspecting histograms of enrichment factors for negative controls and synonyms of the wildtype. Then, we labeled each mutation as 'observed-functional' if it appears in at least one functional variant, 'observed-dead' if all variants containing it were non-functional, or 'unobserved'. We sample combinations of these mutations with 2-8 mutations per variant, by uniformly sampling within each group of labels and sampling labels with probabilities (observed_live: 0.97, observed_dead: 0.01, unobserved: 0.02). The hit rate of this library was lower than we had hoped, likely due to our 'observed-functional' labeling being too permissive and including observed_dead mutations too frequently in this sampling.

Loop exploration: In G3, we included a small library to explore a hypothesis based on the role of mutations to the loop in residues 82-89 in modulating substrate binding. We randomly combined mutations in this region that had appeared in G1 or G2 in at least one variant with comparable or better activity than the WT and used 125 distinct variants at each radius between 3 and 6 mutations.

Single-site mutants: In G2 we included all single-mutation variants for all positions in the design region. In G3 we included single-mutation variants at positions that were in the design region for G3 but not G2.

Assay QC: Each round included a number of additional variants used for the sake of verifying the consistency and quality of the assay. Our 'stratified sample' was obtained by assigning variants to 4 discrete activity levels and then uniformly sampling a few variants from each group. We also included every variant that had been investigated in the previous round's plate assay described below.

Directed Evolution (DE) Campaign

A classical directed evolution campaign was pursued in parallel to the designed strategy to compare to ML campaign (Supplementary Figure 18**)**. The sorted library from G1 was used as input for DE2 (i.e. the same library that was used for training the model to design ML2). The DNA sequences of NucB from the input library were cloned and purified before being amplified

using a process of PCR shuffling termed StEP recombination[117]. The variants were then sorted in 8 parallel runs for the highest activity droplets (between the top 0.5–1%). Each run interrogated approximately 2.2 million droplets corresponding to 1.6 million cells. A total of 15,500 droplets passed the sorting thresholds and were collected and recovered for downstream assays and the next round of mutagenesis. A high activity variant with genotype D64S, A73R was isolated from the recovered cells using the liquid culture plate assay.

Variants for the DE3 were generated using a mixture of 1 or 2 rounds of error-prone PCR from the post-sort DE2 library, and 1 round of error-prone PCR from the D64S, A73R isolated variant. All variants were pooled and went through 6 rounds of iterative sorting. The top 0.5% droplets (Or the top 5% cells assuming an average 10% droplet occupancy) were sorted at each round. The post-sort libraries were further validated using the liquid culture plate assay, and hits identified with the specific activity assay. The highest activity variant discovered with the DE campaign had three substitutions: A63S, D64S, A73R.

Experimental Methods

Designed DNA library generation

Library designs were ordered as oligo arrays from Twist Biosciences. The initial site-saturation library mutated residues 33 to 142 of *B. licheniformis* NucB, excluding the native signal peptide sequence and active site residues D93 and N117, which coordinate the active site magnesium. Oligonucleotide synthesis was limited to 300 nucleotides, which was further limited to a design region of 78 amino acids, after subtracting restriction enzyme cut sites and spacers. For simplicity, we did not design variants containing insertions or deletions. Each variant contained mutations only in a single *design region*. These were chosen to maximize the proportion of promising mutations while exploring as much of the protein as possible. G2 used a single design region at residues 33–110 and G3/G4 used two overlapping regions: residues 33–110 and 65–142.

Due to errors during DNA synthesis and amplification, the DNA libraries contained a significant number of distinct sequences beyond what was designed. 14506 of the 55760 variants that had sufficient abundance to characterize enzyme activity came from such errors. These variants are not used in our hit rate analysis, but they were utilized when designing variants, since these non-designed variants sometimes displayed non-zero activity because they often result from crossover between designed variants.

In-silico design methods generated amino acid sequences, which were converted to DNA sequences as follows. All unchanged codons used the WT (*B. licheniformis*) codon. Mutated codons used the canonical codon given by the *B. subtilis* codon usage table[118]. Any designs with a *BsaI* cleavage motif (GGTCTC or GAGACC) had their first codon substituted with the next-most-likely *B. subtilis* codon

Random DNA library generation

We used both error-prone PCR (epPCR) (Agilent Genemorph II error-prone PCR kit) and shuffling by the Staggered Extension (StEP) Process PCR[117]. epPCR was carried out on the full length of the mature peptide according to the manufacturer's recommendations and subsequently purified by agarose size selection. StEP was performed on enriched library variants using a PCR protocol adapted to the KAPA HiFi HotStart ReadyMix (Roche). To maximize recombination, we used a 35–40°C extension temperature, with 100 cycles of 5s extension. Products were purified by agarose size selection using the Zymoclean™ Gel DNA Recovery Kit and run on a gel, size selected and purified.

Since StEP PCR can regenerate many parental sequences, COLD-PCR[119] was performed to enrich non-parental sequences, using an 85°C denaturation temperature for NucB which decreases PCR efficiency for DNA homodimers, but not heterodimers.

Nuclease expression in *Bacillus subtilis* host strain

Libraries were cloned into an IPTG-inducible shuttle vector which was ultimated integrated into *B. subtilis* for subsequent screening. The hybrid T7-lacO promoter [120] was employed due to its low background expression in E. coli. To further reduce leaky expression in *E. coli*, a copy of LacI is included in the backbone of the shuttle vector. T7 RNA polymerase required to transcribe the gene of interest is present only in the host *Bacillus* strain. IPTG-induced expression in this system was found to be equal or greater than expression from the constitutive Pveg promoter.

Expression vector construction. Plasmid libraries were assembled using either Gibson or Golden Gate assembly. For Gibson assembly, the NEBuilder Hifi DNA Assembly Master Mix (NEB E2621) was used according to the manufacturer's instructions. For Golden Gate assembly, the NEB® Golden Gate Assembly Kit (BsaI-HF®v2) (E1601) was used according to the manufacturer's instructions. A diagram of the plasmid construct is presented in Supplementary Figure 17a. Flanking sequences from amyE allow for integration of these constructs in B. subtilis via homologous recombination at the amyE site.

Assembled plasmids were transformed into *E. coli* for propagation by electroporation of 2-µL of a 1:1 dilution of the assembly reaction in nuclease free water. E. cloni® 10G SUPREME electrocompetent cells (Lucigen 60080-2) were loaded into a 1-mm cuvette as per the manufacturer's instructions. To determine transformation efficiencies, 10, 100, and 900 µL of recovery volume were plated on LB agar plates containing the appropriate antibiotic then incubated overnight at 37°C. The assembly mix was stored at –20°C until the transformation efficiencies were determined, then the number of reactions were scaled as needed to obtain sufficient library representation. Libraries were plated on 245-mm square LB agar trays (1–2mL recovery volume for each plate). After picking colonies for library QC, the q-trays and plates were scraped with 5 mL liquid LB and pooled. The plasmids were purified by ZymoPURE II Maxiprep kit from 10 mL each of pelleted cells.

Bacillus subtilis host strain. We used *B. subtilis* strain SCK6 (Bacillus Genetic Stock Center ID 1A976) from Zhang and Zhang[121]. Overexpression of the master regulator ComK in this strain enables high transformation efficiencies.

Bacillus subtilis library transformation The host strain was prepared for transformation by xylose-induction of ComK then frozen at –80°C as per Zhang and Zhang[121]. Frozen aliquots of competent cells were allowed to thaw at room temperature for 15 minutes. Transformations were carried out by adding 1 µg of the plasmid libraries to 1 mL of cells in sterile, round-bottom tubes and gently mixing. The tubes were incubated at 37°C incubator for 1.5 h while shaking. Transformation efficiencies were determined by plating 1 µL of the recovery mixture on an LB agar plate containing 10 ug/mL kanamycin, 5 ug/mL erythromycin, and 100 ug/mL spectinomycin (subsequently referred to as LB-KES). Libraries were subsequently plated as 200-µL volumes onto solid agar plates (245-mm, LB-KES, Teknova L4795), yielding approximately 100,000 cfu after overnight incubation at 37°C. The number of plates were scaled as required to obtain sufficient library representation.

Protein production and harvest

Strains with high activity in liquid culture plates were selected for protein expression. For each strain, two 2-L baffled flasks with 500-mL LB-KES, 100 mM MOPS, pH 7.2, 2% glucose were inoculated with 5 mL overnight cultures incubated at 37 °C, shaking at 220 rpm. Once the culture reached an OD of 0.8 (approximately 4h), IPTG was added to a final concentration of 0.5 mM to induce protein production overnight. Secreted NucB nuclease was harvested from the spent media (around 880 mL total) by centrifugation at 6000 rcf for 20 min and subsequently filtered across a 0.2 µm membrane.

Protein purification

We purified the NucB nuclease based on the method described in Rostami, et al.[46] using two chromatography steps. Briefly, proteins were precipitated from spent media using saturated ammonium sulfate solution to 65% final saturation (~1800 mL per liter of culture) and stirred at 4°C overnight. The precipitated protein was pelleted by centrifuging at 22,000 rcf at 4°C for 60 min. The pellet was resuspended at 4°C in 5 mL of 50 mM potassium phosphate, pH 7.2, 1.5 mM β-mercaptoethanol (BME), and protease inhibitors (Roche cOmplete) to a total volume of approximately 10 mL. After sterile filtration , the protein solution was desalted by FPLC (Akta start, Cytiva) at 5 mL/min on a pre-equilibrated XK 26/10 Hitrap Desalt column (Cytiva). The mobile phase was 50 mM potassium phosphate at pH 7.2, 1.5 mM BME, and 0.5 mM PMSF. Fractions containing NucB were pooled and subsequently purified by ion exchange. Samples were loaded onto a 5-mL Q-Sepharose HiTrap column, pre-equilibrated with the same mobile phase as used in desalting. NucB was eluted with 2 M NaCl in 25 mM Tris, pH 9, 1.5 mM BME, and 0.5mM PMSF. The fractions containing NucB were analyzed by SDS-PAGE (Bio-Rad Criterion AnykD, 26-well) . Fractions were concentrated using 3 kDa cutoff spin concentrators (Amicon® Ultra-15 Centrifugal Filter Unit) to a final volume of 5 mL and then dialyzed twice against 2L of 10 mM Tris, pH 9.0.

Nuclease activity assays

To select the set of variants to more-deeply characterize in our low-throughput, high-resolution assays, we used three different assays in series to isolate the top performers. 1) First, we used our ultra-high-throughput droplet-based microfluidics platform ("Automated Droplet-based Fluorescence Assay") to iteratively sort at increasing fluorescence thresholds (Figure 1a). 2) Cells that were sorted were then preliminarily assessed for activity in a microtiter plate-based enzyme kinetic assay using cultured strains ("Liquid Culture Plate Assay"). The top variants from the liquid culture plate assay were then assessed with 3) a microtiter plate-based enzyme kinetic assay using purified enzyme ("Specific Activity Assay"). Finally, the best variants from each campaign were assayed for biofilm disruption (Supplemental Section 6D). This progression of assays trades throughput for higher resolution (Supplemental Figure 7).

Nuclease activity was assayed with DNA hydrolysis probes consisting of two sets of duplexed 20-mer oligos: one labeled with a fluorescent probe and quencher, and one unlabeled. The ratio of the two substrates was tuned to maximize the linear response curve for nuclease activity. Endonuclease activity of NucB releases the quencher on the 3' end of G537 (3' Iowa Black® FQ) effectively dequenching the fluorescent probe at the 5' end of G651 (5' Alexa Fluor® 488).

Automated Droplet-based Fluorescence Assay

To measure the activity of millions of nuclease enzyme variants, we built a custom microfluidic platform and devices to conduct ultra-high-throughput screening in droplet-based microfluidics[22]. Cells in expression media with 0.1% (w/v) Pluronic F-127) were encapsulated as a water-in-oil emulsion in fluorocarbon oil, stabilized with a biocompatible surfactant on a custom microfluidic chip. Cells were prepared for encapsulation by culturing overnight at 37°C in LB-KES, then back-diluted 1:200 and grown for 8h to maximize cell viability. Cells were then washed and diluted to OD 0.08 to ensure a lambda of 0.1 in drops according to the Poisson distribution (average of 1 droplet containing a cell out of 10 total droplets). The low density minimized the chance of two cells being encapsulated in the same droplet, preventing false positives. Droplet diameters were tuned to 20 µm (~5 pL volume). Droplets were incubated at 37°C for 16 h for cell growth and nuclease expression, then passed through a second microfluidic chip where assay reagents were introduced via picoinjection[122], incubated on-chip for 4 seconds, sorted by fluorescence intensity, then merged into an aqueous recovery channel. The picoinjected assay solution consisted of 100 mM MOPS, pH 7, 2.5 mM $MnSO_4$, 2 µM G651/G537, 50 µM G24/G25 and 0.1% (w/v) Pluronic F-127. Sorted cells were fully recovered by breaking any residual emulsion with perfluorooctanol (PFO) and plating ~100 drops to estimate the recovery rate. The remainder of recovered cells were grown in 25 mL of LB+KES media overnight at 37°C.

Liquid Culture Plate Assay

The liquid culture plate assay was used to isolate hits obtained from the ultra-high-throughput screen. Optical density was used to normalize the measured activity, and therefore does not control explicitly for enzyme titer. The culture for plate validation was prepared in two stages: the growth phase, followed by the induction phase.

In the growth phase, a 96-deep-well plate was filled with 1 mL per well of LB-KES broth. Each well was then inoculated with a single colony. To maintain sterility while allowing gas exchange, the plate was covered with a breathable seal. The plate was then placed in an incubator set at 37°C, 750 rpm for 8 hours. After the incubation period, the optical density (OD) of the cultures was measured at a wavelength of 600 nm. For the OD measurement, 10 uL of each culture was diluted in 90 uL of 150 mM NaCl saline solution. Background correction was performed considering a 10-fold dilution in 100 uL, resulting in an approximate value of 0.094 absorbance units (AU). Additionally, a volume correction factor of approximately 0.3 was applied due to the 100 uL pathlength used for the measurements. Basic normalization for growth in the liquid culture was accomplished by dividing v_{max} by OD600 of each culture.

In the induction phase, another 96-deep-well plate was filled with 1 mL per well of expression media (LB-KES supplemented with 100 mM MOPS, pH 7.2, 2% glucose, and 0.5 mM IPTG). The 8-hour cultures were used to inoculate this plate, with 5 µL added per well. As before, the plate was covered with a breathable seal and then incubated at 37°C, 750 rpm for a minimum of 16 h.

Specific Activity Assay

Specific activity measurements for selected variants are presented in Figure 2b. Protein purification is a labor-intensive process that must be performed serially for each strain. The following variants were purified: the top-performing variants from each ML generation, the top performing strain for the DE campaign, and the wildtype enzyme. Each variant was evaluated at 4 concentrations (12.5, 25, 50 and 100 ng/mL) and its v_{max} was normalized to the kinetic rate of the wildtype enzyme at the same concentration, resulting in a measurement of fold-change activity. To determine whether one variant was higher activity than another, a permutation test was performed on the average of the fold-change activities measured at the 4 concentrations.

Both the liquid culture and specific activity kinetic assays measured activity at 25°C in 200mM MOPS pH7 buffer, 5mM MnSO4, 0.2% Pluronic in 384-well plates (Corning 3577). The fluorescently-labeled substrate (G651/G537) was present in the assay at 0.4 µM and the unlabeled substrate (G24/G25) was at 100 µM. Fluorescence was measured over a 40-60 minute timecourse with excitation at 495 nm and emission at 525 nm at fixed interval (12s for specific activity assay, and 1 min for liquid culture assay). Activity was calculated by fitting the linear slope of the initial fluorescence intensity change[123]. Examples of kinetic curves are shown in Supplementary Figure 14.

Selecting fluorescence thresholds for ultra-high-throughput sorting

In each round, the population of cells was sorted in parallel at multiple fluorescence thresholds, where each threshold was determined by the fluorescence of a fiducial enzyme sequence with known activity. Droplets of a sample of the library and of the fiducial sequences were generated and varying quantities of mFluor Green 620 acid (AAT Bioquest catalog number 1144) were added to the droplets before emulsification to differentiate the droplet samples in the assay. Droplets were then pooled and assayed for fluorescence intensity in our microfluidic platform. A

488-nm laser was used to excite both the mFluor Green 620 acid and the 5' Alexa Fluor® 488, which were measured with TRITC/CY3 620/52nm (Thorlabs, MF620-52) and FITC 530/43nm (Thorlabs, MF530-43) BP Emission Filters, respectively. Gates were selected relative to the activity of the fiducial sequences. For example, gates with fluorescence threshold at the center of the fiducial distribution are used to categorize variants having equivalent activity to the fiducial sequence. Gates set at the right tail (i.e. greater than the mean of the fiducial fluorescence distribution) are used to categorize variants as having improved activity relative to the fiducial (See Supplementary Figure 27).

Next-generation sequencing (NGS)

Variant sequences were determined by next-generation sequencing on the MiSeq platform with paired-end reads. Variable regions from each library were amplified by PCR with forward primer sequence TATTCTCCTCAGCATGCCGAAGGCG and reverse primer sequence AGATTACTACTGATAACCACTGTTGATTG. The adapter and sequencing primers are appended to the 3' end of the primers, with a variable 0–7 base-pair spacer to enable demultiplexing of pooled libraries. The fastq files were preprocessed using fastp, and aligned to the reference DNA sequence using Bowtie2. The details of the sequencing depth is summarized in Supplementary Table 6 .

Processing data from ultra-high-throughput experiments

We convert the observed NGS counts to discrete enzyme activity labels for the following reasons. First, since cell sorting is a discrete procedure, using discrete labels better reflects the nature of the underlying measurement, i.e. that variants that passed through the sort achieved the fluorescence threshold. Second, estimates of enrichment factors include noise from biological and technical variance. By discretizing, we can reduce models' overfitting to noise, and for these reasons we train multi-class classification models. Third, discrete labels allow us to analyze a library's hit-rate, which is easily interpretable. Finally, by using discrete activity buckets derived from fiducial sequences that appear in multiple rounds of experiments, it is straightforward to aggregate measurements from multiple rounds to create a single genotype-phenotype dataset (Supplementary Figure 24). See Supplementary Figure 23 for a schematic overview of the data processing procedure.

Computing enrichment factors: We perform NGS on both the pre-sort (input) library and the post-sort (output) variant pools. For a variant V, we estimate its abundance as:

$$abundance_V = \frac{reads_V}{total\ NGS\ reads}$$

The *enrichment factor* of V is the ratio of post-sort abundance to pre-sort abundance:

$$EF_V^{sort} = \frac{abundance_V^{post-sort}}{abundance_V^{pre-sort}}$$

Estimating the EF is sensitive to errors in the denominator. Therefore, we only kept variants that had abundance above a given threshold in the input pool. For example, in G4, only variants with ≥50 counts in the input pool were included, which left 15404 variants whose enrichment factors could be accurately estimated. This is only 20% of the total variants present with ≥2 reads (see Supplementary Figure 25).

Fiducial sequences: To interpret the enrichment factor of a screened variant, we compared it to the distribution of enrichment factors for a given fiducial sequence with known activity. In each library, we included multiple synonymous variants of each fiducial, where these can be distinguished during sequencing. Variants' enrichment factors for each sort were computed after translating to amino-acid space, while fiducial enrichment factors were computed based on DNA sequence reads. Variability in the enrichment factors of synonymous variants allows us to account for noise in the assay (i.e. from variability in growth rate, expression level, cell cycle, sorting, and other sources of technical and biological variability).

Constructing Fiducial Sequences: Synonymous variants were constructed by taking a stratified sample over the number of codons to modify. For a given number of codons C, C unchanged codons (i.e. those that did not include any amino acid mutations relative to the wildtype) were selected uniformly at random and changed to the next most common synonymous codon in the *B. subtilis* codon usage table. Error-prone PCR introduced synonymous codons and premature stop codons in G1. In each subsequent (designed) generation we picked fiducial sequences based on variants that had known activity confirmed in specific activity assays. In G2 and G3, we introduced synonyms of the wildtype and A73R, the best variant discovered in G1. In G4, we additionally included synonyms of (A73R, D74S) and (A63P, A73R, D74H, I84Y), found to have high activity in G3. Fiducials were designed for each design region. See Supp. S10 for details.

Hit-calling relative to a fiducial: To determine that a variant has activity greater than a fiducial in a given sort, we compute the t-statistic and associated p-value for the right-sided test where the null distribution is given by the fiducial's enrichment factors (see Supplementary Figure 24) and the observation contains a single enrichment factor for the variant EF_V^{sort} . Given a set of variants with associated p-values, we assign discrete labels to them jointly, controlling the overall expected false discovery rate (EFDR) by applying a Benjamini-Hochberg (BH) correction[51]. A variant with a significant p-value after correction is labeled as “hit”, but this labeling will vary depending on the context. For example, at times we report the hit rate of an entire library design method, while elsewhere we report separate hit rates of that method for variants at different distances from the WT. Here, the BH correction is applied within each pool of variants that a hit rate is reported for. We use an EFDR of 0.1 throughout the paper.

Obtaining resolution for wide-ranging activity levels: To characterize variants into multiple discrete activity levels that cover a broad range of enzyme activity, we sorted in parallel at multiple fluorescence thresholds (Figure 1c). This is necessary because the enrichment factor is a sigmoidal attenuation of the underlying enzyme activity. For example, high activity variants

cannot be distinguished by sorts performed at low fluorescence threshold (Supplementary Figure 24) because nearly all high-activity variants have the same sorting outcome. For each generation, fluorescence thresholds were chosen prior to sorting according to the procedure outlined above.

Obtaining the final genotype-phenotype dataset. To construct the final 55760-variant dataset of sequences from all generations, we needed to reconcile multiple, potentially-conflicting, activity labels for a given variant. Within a generation, the hit-calling with respect to multiple fiducials may be inconsistent, since different fiducials may use data from different gates. This does not guarantee, for example, that if we label a variant as better than WT we also label it as better than the negative control. Second, the labeling may be inconsistent across generations. For labels that appear in multiple generations, we take the label from the latest generation. Within a generation, we further assign each variant the highest activity label for which it was labeled as better than the corresponding fiducial. For example, 5 variants across G3 and G4 failed to reject the null when compared to the negative control, but rejected the null when compared to the WT and A73R fiducials and 973 variants across G3 and G4 failed to reject the null when compared to the negative control, but rejected the null when compared to the WT.

Quantifying diversity with sequence clustering

We used a method inspired by the clustering in UniRef, where clusters are defined by the maximum distance from the seed: i.e. in UniRef90 clusters are composed of sequences that have at least 90% sequence identity with the seed sequence of the cluster[124]. To build clusters for a given set of variants, we first set the maximum distance D between two sequences in the same cluster. Then, we build a dendrogram between sequences by starting with one node per sequence and iteratively connecting two nodes if the distance separating them is the smallest among all pairwise distances. The distance between two nodes u and v is given by the “farthest point” inter-cluster distance i.e. $d(u, v) = \max_{ij} d(u[i], v[j])$. Nodes are joined iteratively until all sequences are connected. Clusters are formed by the largest nodes that contain sequences whose maximum pairwise distance is no larger than D.

Quantifying negative epistasis

Epistasis is often quantified for continuous fitness measurements, where it measures the extent to which the impact of mutations on fitness is non-additive [112]. For our discrete activity labels, we instead measure the extent to which the impact of applying multiple mutations to the protein renders it functional vs. non-functional in a way that is consistent with mutations impacting the protein independently. Many protein engineering approaches seek to combine mutations that have been previously observed to maintain or improve protein function (i.e., they have been labeled as having non-zero activity). Therefore, we investigate the rate of negative epistasis: how often combining such mutations produces a non-functional protein.

Our dataset contains experimental measurements for nearly all single-mutation variants of the WT. From this, we obtain a list of mutations that were observed to not destroy the function of the

protein using our above labeling scheme. Then, we select the set of multi-mutation variants that only contain mutations in this list. The negative epistasis rate is defined as the fraction of such variants that are non-functional. Under a null model of the protein fitness landscape where mutations impact the protein independently, we would expect the negative epistasis rate to be 0. Given that the labeling scheme has an expected false positive rate of 0.1, and an additional chance of false-negatives, however, the expected empirical epistasis rate is non-zero even under the null model. We only report negative epistasis for double-mutation variants, where the impact of false positives on the analysis is smaller than it would be for higher-order mutants.

Competing interests

C.X., H.L., K.Hirano., V.P., K.D.N., K.I., L.F., K.Hoff. and J.J.A. performed research as part of their employment at Triplebar. J.J.A. is a cofounder of Triplebar. N.T., D.B., C.A.E., M.C., A.R., and L.J.C. performed research as part of their employment at Google LLC. Google has filed a provisional patent application for inventions related to this work.

Acknowledgements

We thank the entire Triplebar team for their support. For helpful feedback and discussions, we would like to thank Andreea Gane, Ankur Parikh, Christof Angermueller, David Andre, Hemai Parthasarathy, Jue Wang, Mathias Voges, Melis Anahtar, Nilesh Tripuraneni, Tim Beissinger, Zach Wu, and Zelda Mariet.

Supplementary Figures

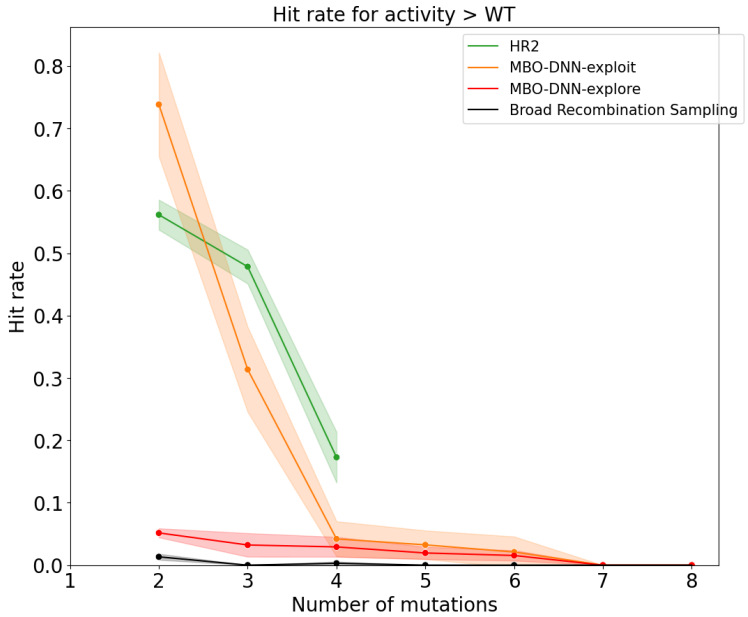

Supplementary Figure 1: *hit rates for key sub-libraries in G2.*

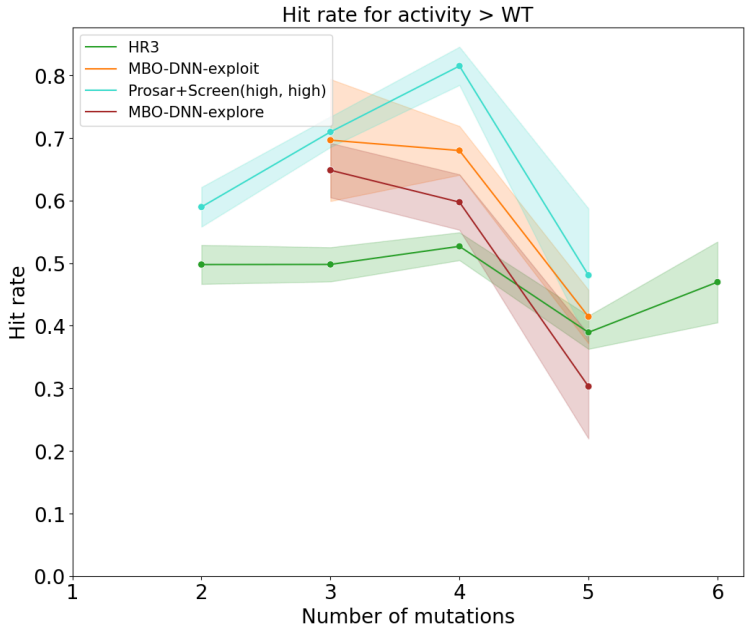

Supplementary Figure 2: *hit rates for key sub-libraries in G3.*

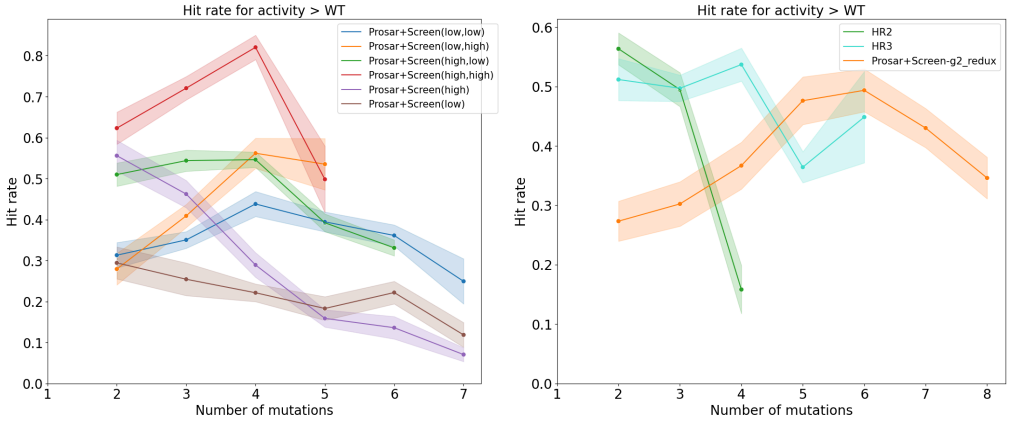

Supplementary Figure 3: *(left) Hit rates for ablations of the Prosar+Screen method where we vary the threshold used for selecting mutations to include in the combinatorial library and the threshold used for dropping recombination variants with low VAE score. (right) Using Prosar+Screen as an alternative design approach in G2 has a similar hit rate to HR2, but the hits include far more mutations per variant.*

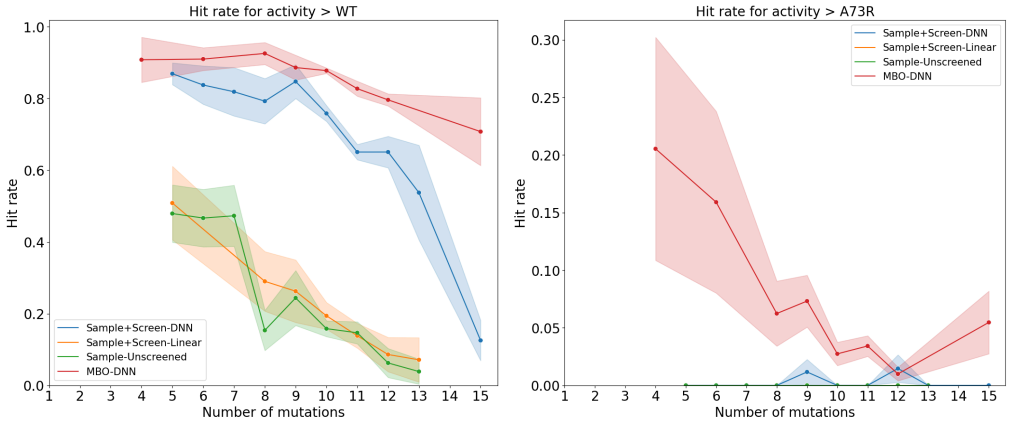

Supplementary Figure 4: *Contrasting the performance of different methods for finding sequences with high model score (Sample+Screen-DNN vs. MBO-DNN) and different types of models (Sample+Screen-DNN vs. Sample+Screen-Linear vs. Sample-Unscreened).*

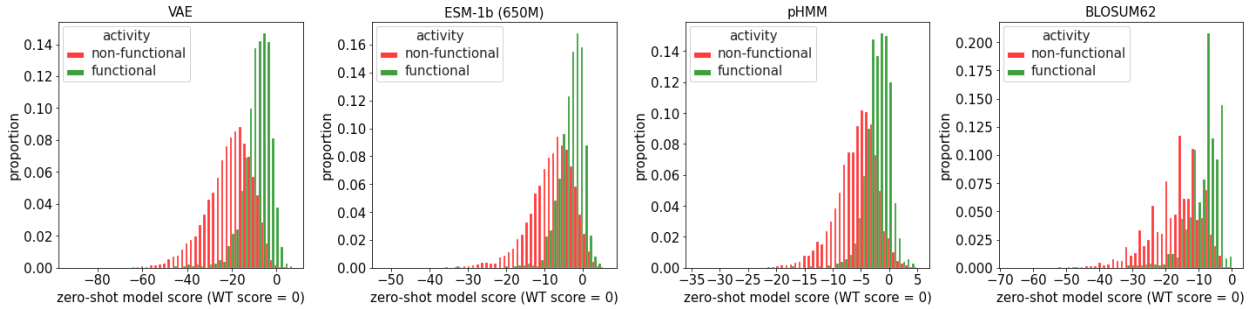

Supplementary Figure 5: *Histograms of zero-shot scores for functional and non-functional G1 variants. All methods provide some separation between functional and non-functional variants, with the distributions most separated for the VAE.*

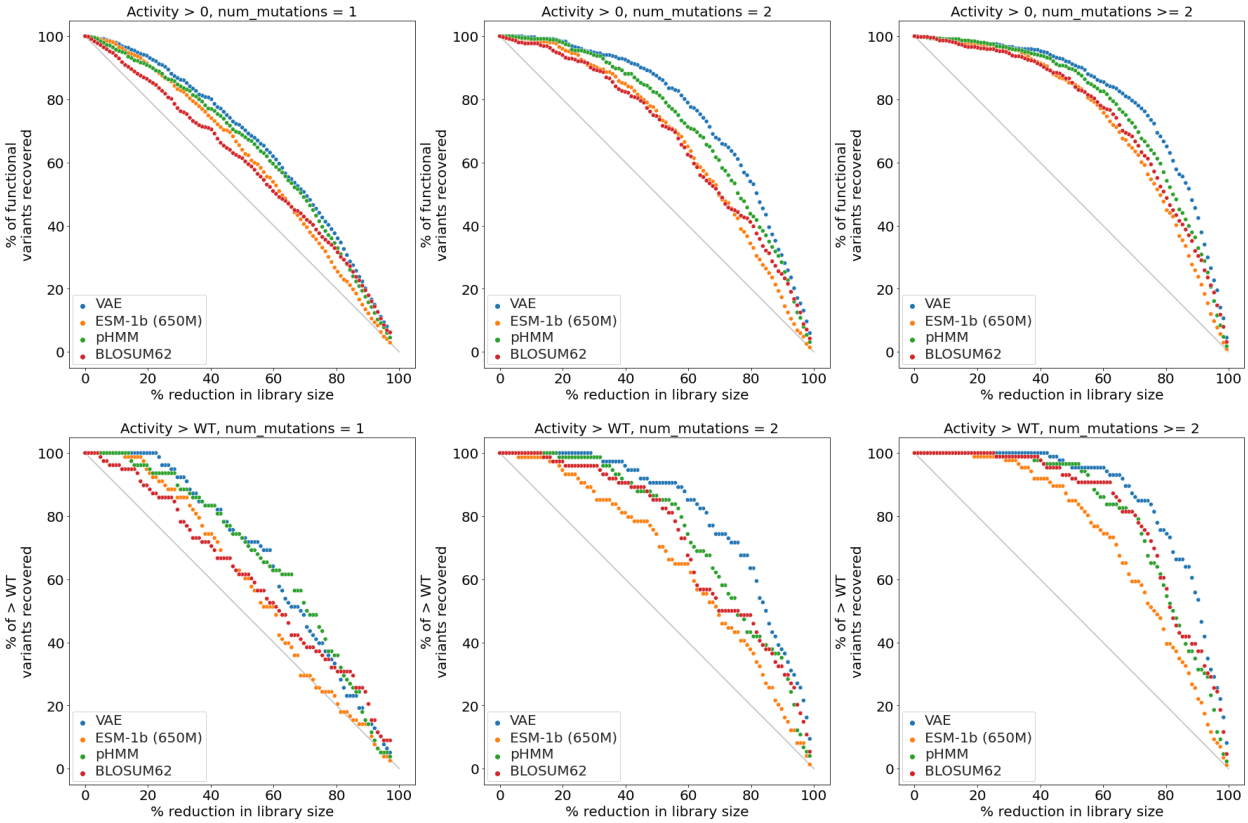

***Supplementary Figure 6**: Effectiveness of sub-sampling the G1 library using various zero-shot scoring methods. Sweeping over the X axis provides a tradeoff between how much the library size is reduced and how many variants with target activity are discovered. Across values dataset reduction percentages, the VAE performs comparably or better than alternative methods at discovering such variants. Subfigure rows: which level of activity is used to define a hit. Subfigure columns: which set of variants is analyzed.*

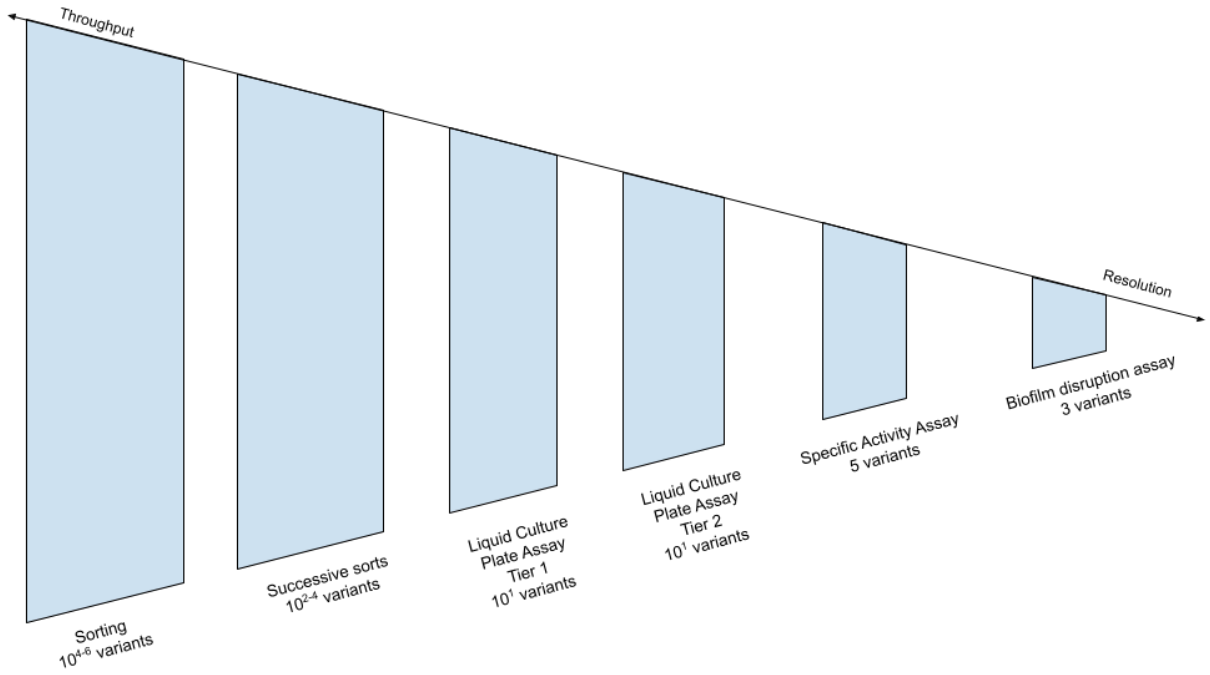

Supplemental Figure 7: The sequence of filtering steps leading from our highest throughput assays to our highest resolution assays. *Our selection procedure proceeds as follows, with the best performers promoted to the next assay at each stage: we screen millions of variants in high throughput, successively sorting at higher fluorescence thresholds. We then screen tens of variants in our plate assay (Tier 1) and verify them with replicates (Tier 2). We then purify the top several performers and screen for specific activity. The very best performers are validated in a biofilm disruption assay.*

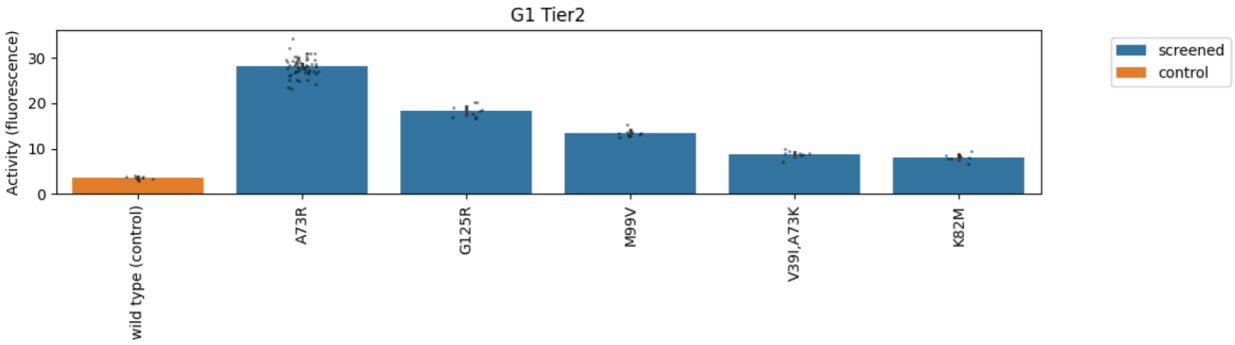

Supplementary Figure 8: G1 Tier 2 liquid culture plate assay activity assessment. *The y axis ("activity") measures fluorescence normalized by optical density. On the x axis are genotyped strains. Variants in orange were added to plates as controls. A73R was selected for purification. Error bars represent ±1 standard error of the estimated activity.*

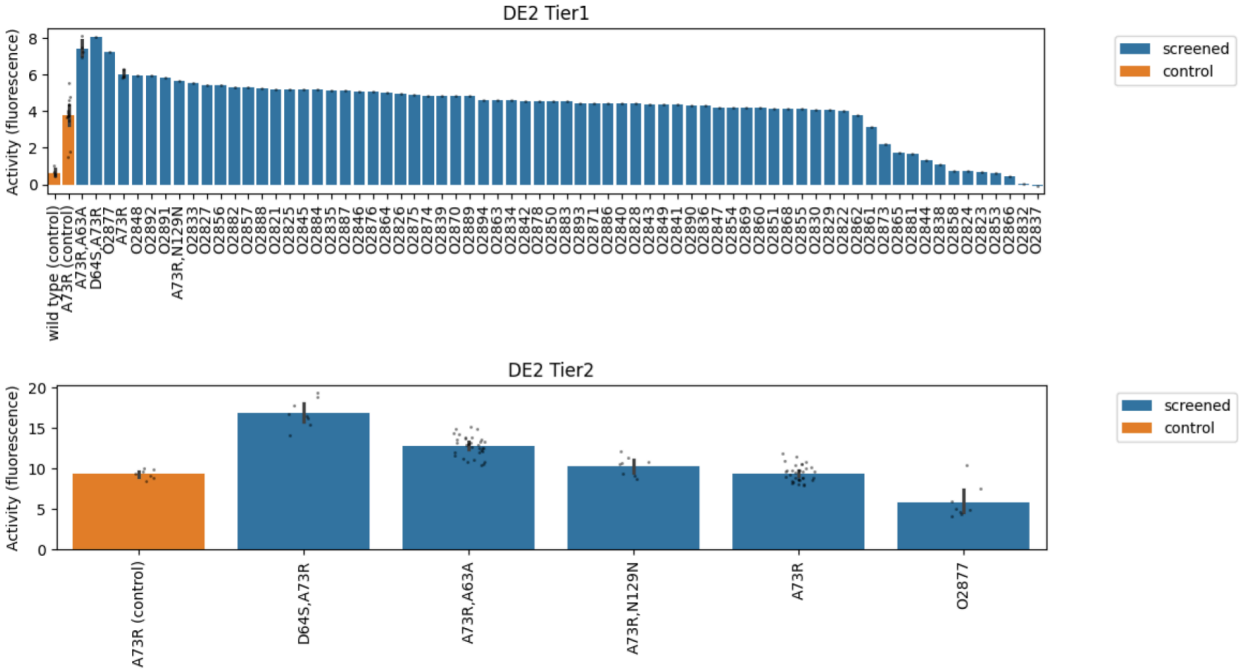

Supplementary Figure 9: DE2 Tier 1 and 2 liquid culture plate assay activity assessment. *The y axis ("activity") measures fluorescence normalized by optical density. On the x axis are genotyped strains. Variants in orange were added to plates as controls. In Tier 1, variants that were not selected were not genotyped and are reported with their numerical strain identifier starting with "O". D64S,A73R has the highest activity in the Tier 2 screen. Error bars represent ±1 standard error of the estimated activity.*

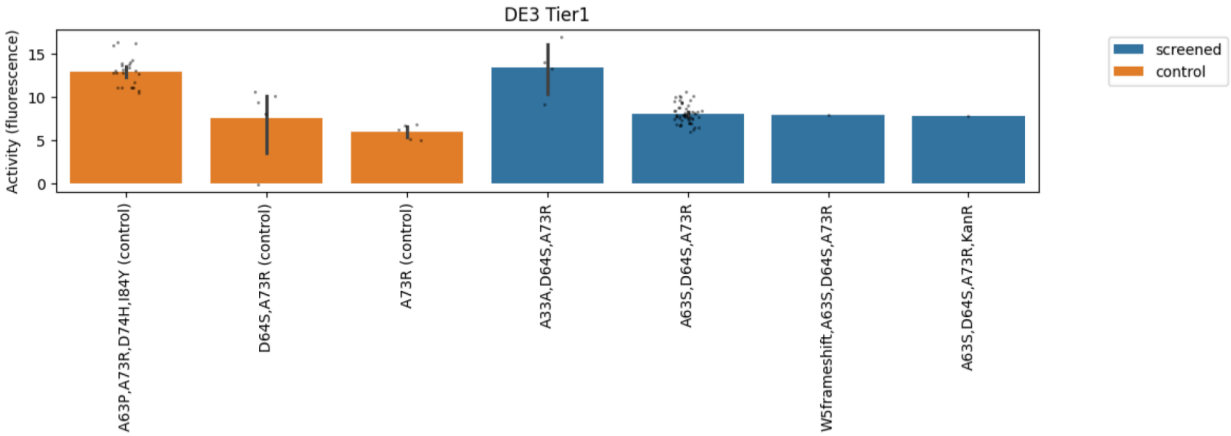

Supplementary Figure 10: DE3 Tier 1 liquid culture plate assay activity assessment. *The y axis ("activity") measures fluorescence normalized by optical density. On the x axis are genotyped strains. Variants in orange were added to plates as controls. A63S,D64S,A73R was selected for purification. A Tier 2 screen was unnecessary because there were sufficient replicates of each genotype Tier 1. Despite its high activity, A33A,D64A,A73R contained a promoter mutation and was excluded from further analysis due to a change in titer confirmed by SDS PAGE (data not shown). Error bars represent ±1 standard error of the estimated activity.*

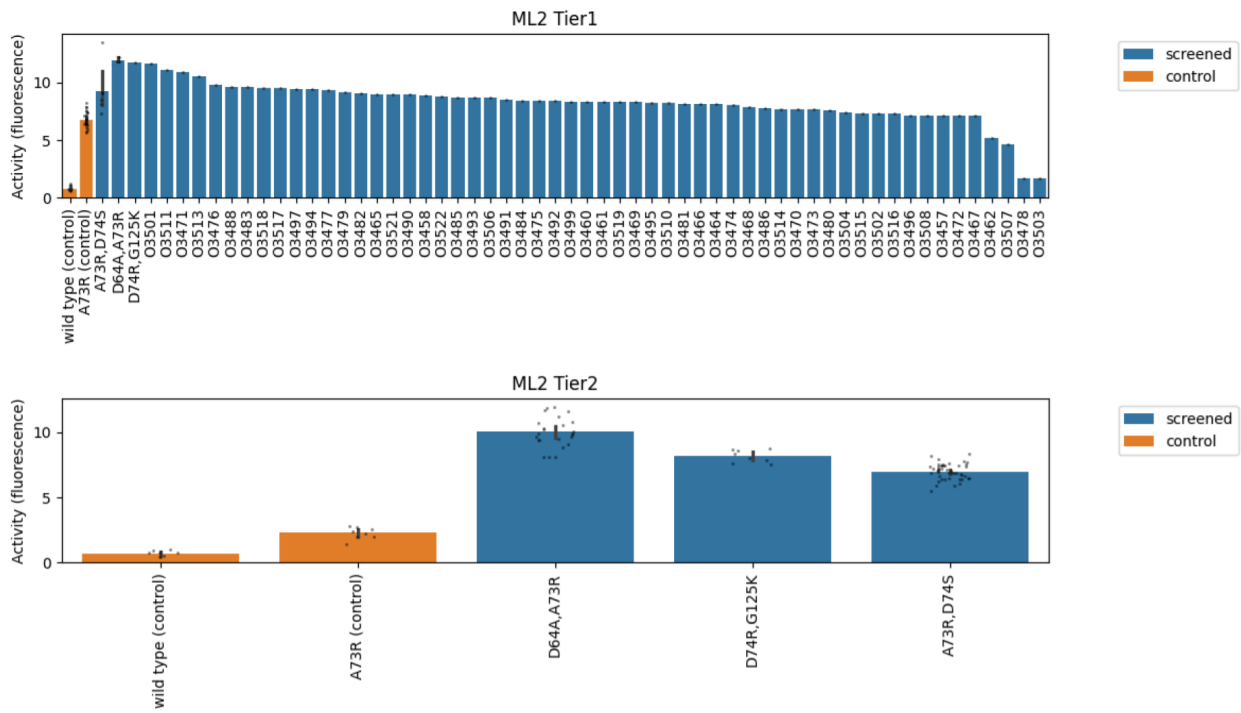

Supplementary Figure 11: ML2 Tier 1 and 2 liquid culture plate assay activity assessment. *The y axis ("activity") measures fluorescence normalized by optical density. On the x axis are genotyped strains. Variants in orange were added to plates as controls. In Tier 1, variants that were not selected were not genotyped and are reported with their numerical strain identifier*

starting with "O". D64A,A73R and A73R,D74S were selected for purification. Error bars represent ±1 standard error of the estimated activity.

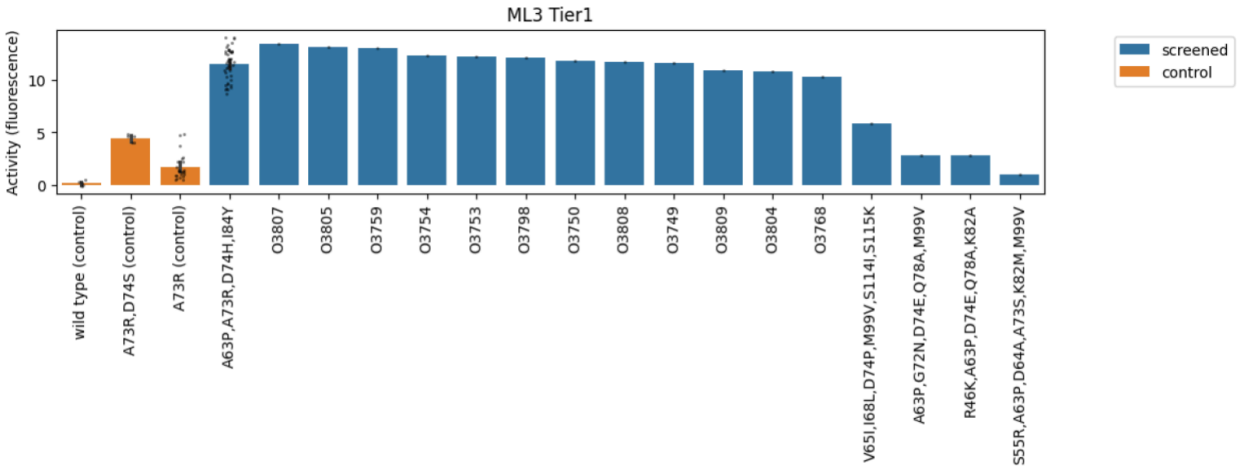

Supplementary Figure 12: ML3 Tier 1 liquid culture plate assay activity assessment. *The y axis ("activity") measures fluorescence normalized by optical density. On the x axis are genotyped strains. Variants in orange were added to plates as controls. In Tier 1, variants that were not selected were not genotyped and are reported with their numerical strain identifier starting with "O". A63P,A73R,D74H,I84Y was selected for purification. A Tier 2 screen was unnecessary because there were sufficient replicates of the highest performing genotype in Tier 1. Error bars represent ±1 standard error of the estimated activity.*

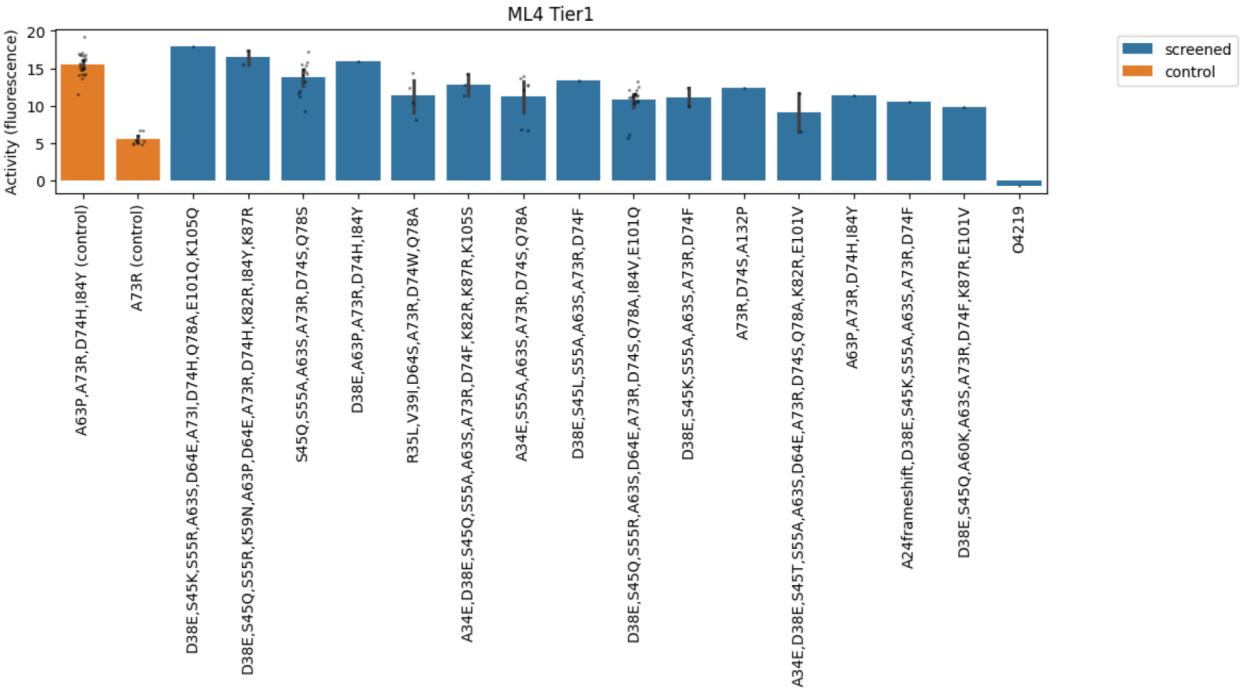

Supplementary Figure 13: ML4 Tier 1 liquid culture plate assay activity assessment. *The y axis ("activity") measures fluorescence normalized by optical density. On the x axis are*

genotyped strains. Variants in orange were added to plates as controls. No variants were purified from this screen, but the screen indicates that 2 variants, one with 10 mutations and one with 11 mutations, achieved activity at or above that of the highest performing variant in ML3 (A63P, A73R, D74H, I84Y, orange).

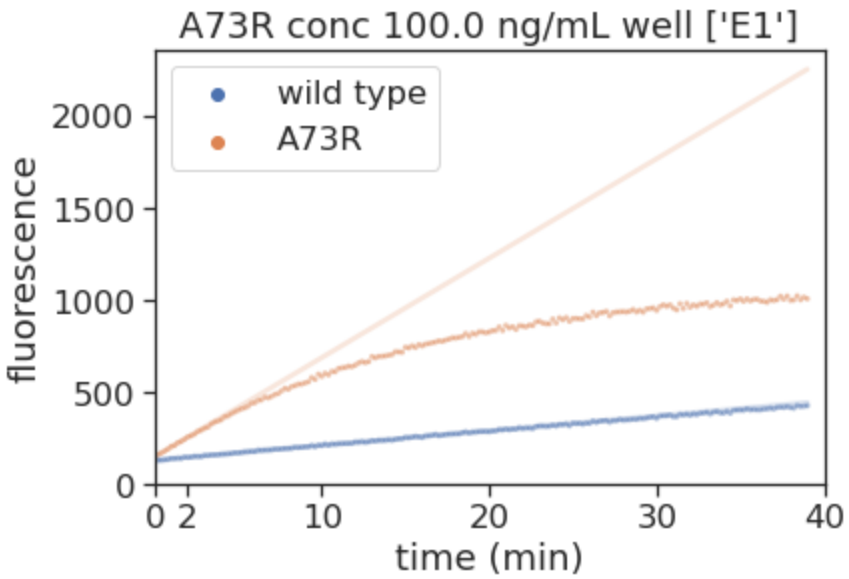

Supplementary Figure 14: fluorescence signal over time for a reaction trajectory. *The estimated slope is the initial velocity of the reaction. The slope of the variant (orange) was computed using the first 2 minutes of reaction data (10 points), while the slope of the wildtype (blue) was computed using 20 minutes of reaction trajectory (100 points). The ratio of the orange slope to the blue slope is the fold-change activity of the variant. The fold change was computed across 4 different concentrations (12.5, 25, 50, 100 ng/mL). In Figure 2b, the overall fold-change activity reported was the average across 1000 samples from the posterior of the estimated slope parameter in each of the 4 concentrations.*

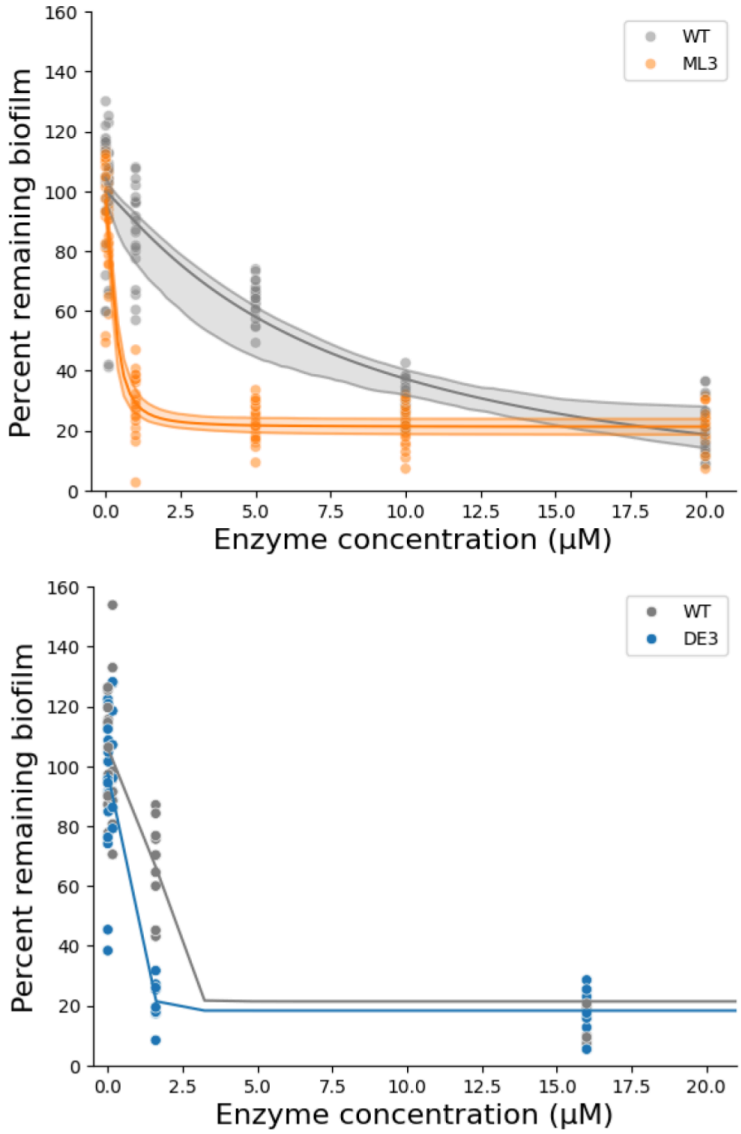

Supplementary Figure 15: Dose-response curves for the best variant discovered in ML3 and DE3. *The best-fitting line was computed by fitting the observed values using the least square method for the Hill equation. The uncertainty interval for the ML3 variant was determined by the 5% and 95% percentile of 200 simulated dose-response curves, sampling the parameters of the Hill equation from a multivariate normal distribution inferred by scipy.optimize.curve_fit. We only show the best fitting curve for the DE3 best variant because there were fewer replicates as well as conditions. There is clear improvement for biofilm degradation of the ML3 variant over the wildtype enzyme at low enzyme concentration. Similarly, at low enzyme concentration the best DE3 variant shows improvement over the wildtype.*

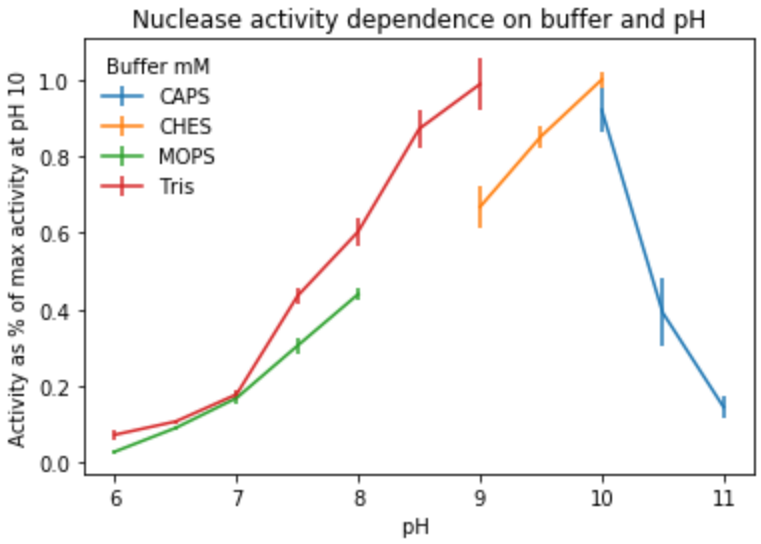

Supplementary Figure 16: Wildtype NucB activity dependence on buffer and pH. *The maximum enzyme activity was achieved in the CHES buffer at pH 10 (with 98.8% of the max activity achieved in the Tris buffer at pH 9). At pH 7, the activity is reduced: in MOPS the activity level is 16.9 ± 1.5% of the max activity, and in Tris, 17.8 ± 1.2%. Activity measurements vary depending on the buffer. Each point is an average of three technical replicates.*

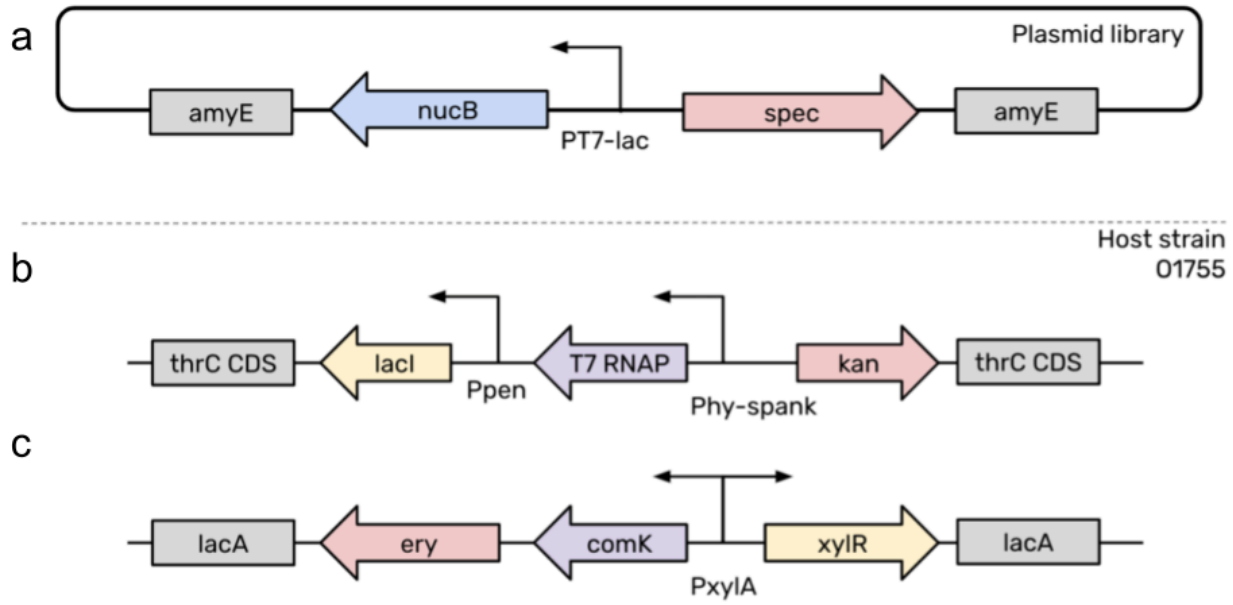

Supplementary Figure 17: Diagram of plasmid library construct and host strain genetic modifications in the final expression strain. *The expression strains consisted of the following: (a) the NucB library with unmodified native signal peptide under an IPTG-inducible T7 promoter integrated into the amyE locus with spectinomycin resistance; (b) LacI and an IPTG-inducible T7 RNA polymerase under the Phy-spank promoter integrated into the thrC locus with kanamycin resistance; (c) xylose-induced comK integrated into the lacA locus with erythromycin resistance.*

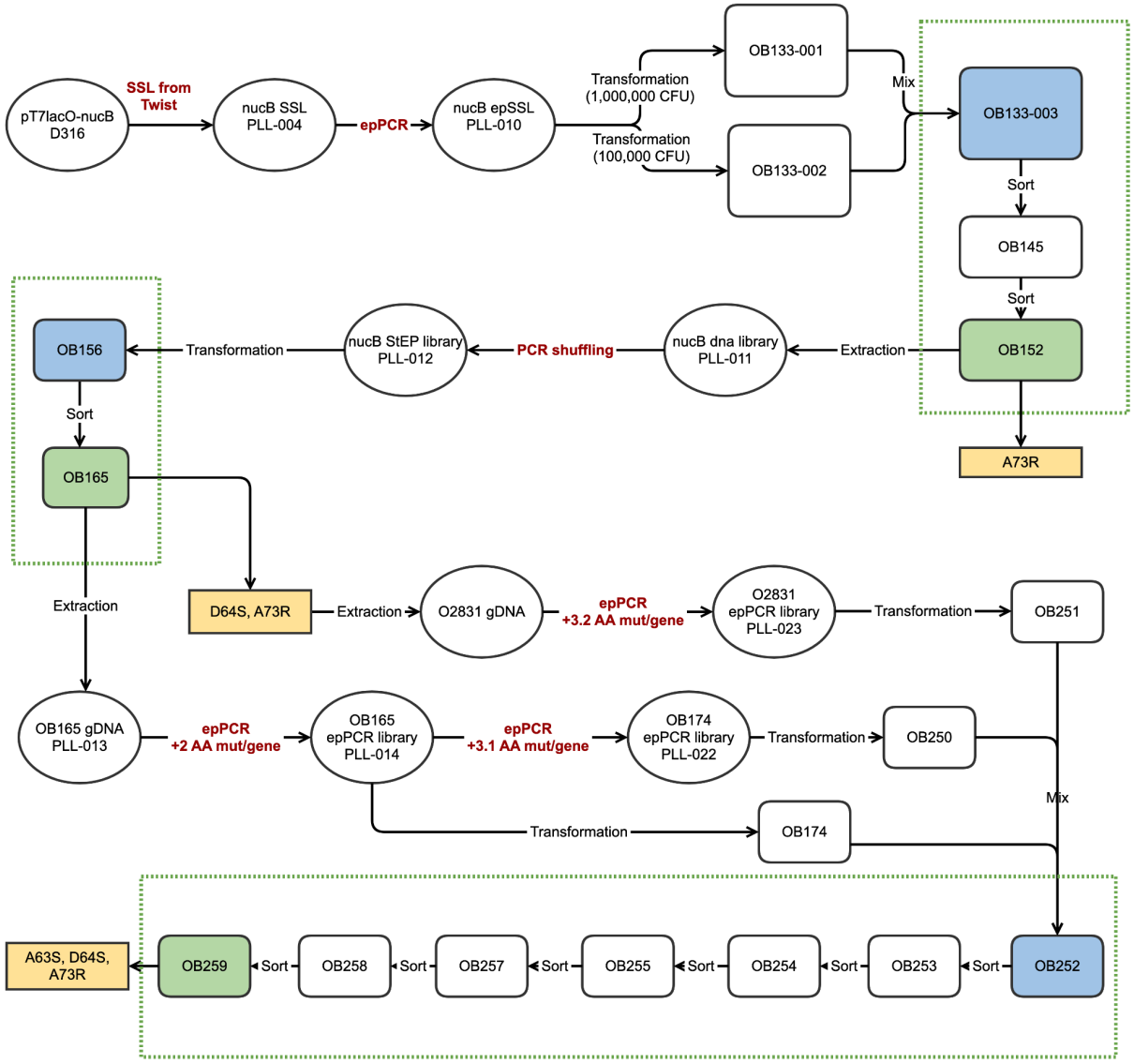

Supplementary Figure 18: Schematic representation of the experimental workflow of the directed evolution (DE) campaign. *The G1 library contained Site-Saturated Sequences (nucB SSL) with additional mutations added using error-prone PCR. For G1, one of the high-gate, post-sort libraries (OB145) was sorted again and underwent culture plate validation. The highest performing G1 strain A73R was found and sequenced from this library. In DE2, the sorted library (OB152) underwent recombination and was sorted again, resulting in a library (OB165) from which the highest performing DE2 strain D64S,A73R was found and sequenced. In DE3, three random libraries were mixed (OB252), one based on epPCR diversification of the highest performing DE2 strain, and the other based on epPCR diversification of an intermediate sorted library from DE2 (OB165). After successive sorts, the highest performing DE3 strain A63S,D64S,A73R was found and sequenced. All samples with names starting with OB*

represent libraries containing mixed strains. Each diversification step is highlighted in red. The starting library of each generation is colored blue and the ending library of each generation is colored in green. The highest activity genotype isolated from each generation is colored in yellow.

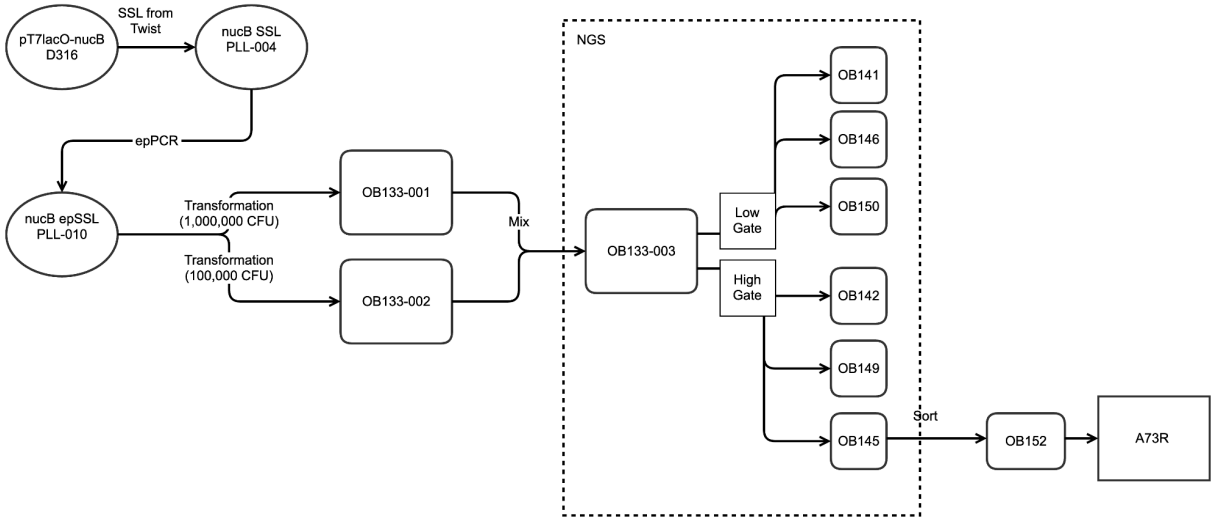

Supplementary Figure 19 : Schematic of G1. *High and low gates were sorted and sequenced with NGS. The G1 library went through high and low gate sorting, with three replicates each. An additional sort (OB152) after a high gate sort led to the identification of the A73R variant. All libraries that were sequenced using NGS are enclosed in dotted lines.*

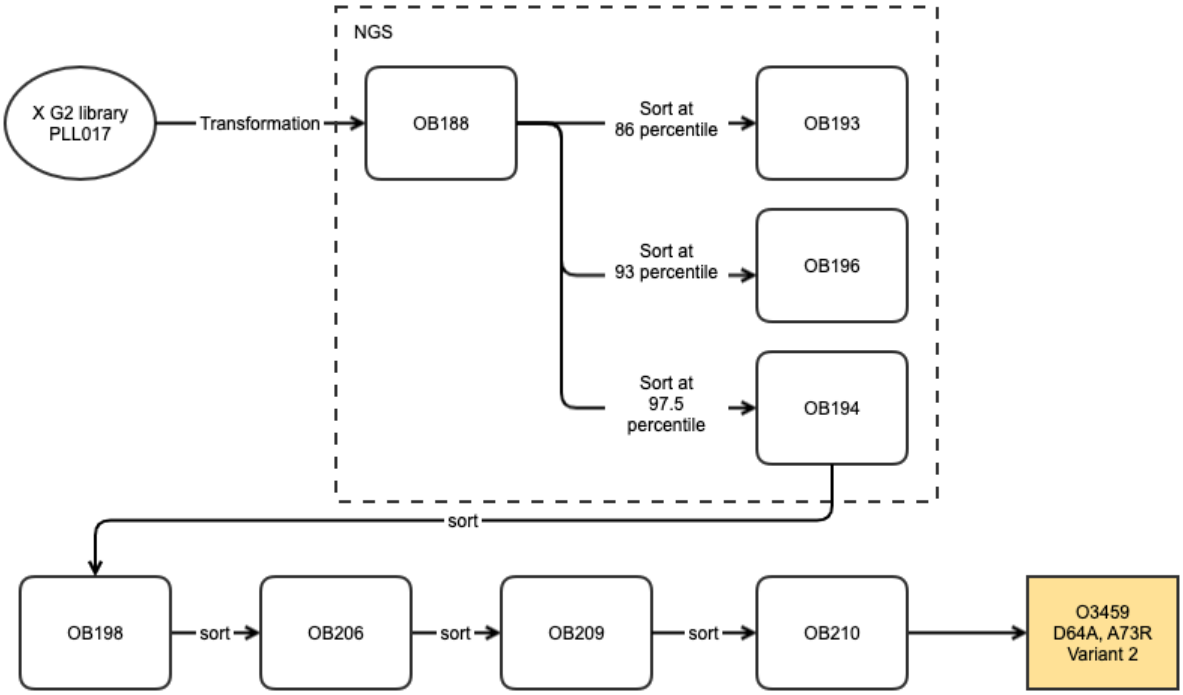

Supplementary Figure 20: Schematic of G2. *Three gates were used for data generation in G2, corresponding to different library fluorescence percentiles. An additional 4 sorts after a 97.5 percentile sort led to the identification of the D64A,A73R variant. All libraries that were sequenced using NGS are enclosed in dotted lines.*

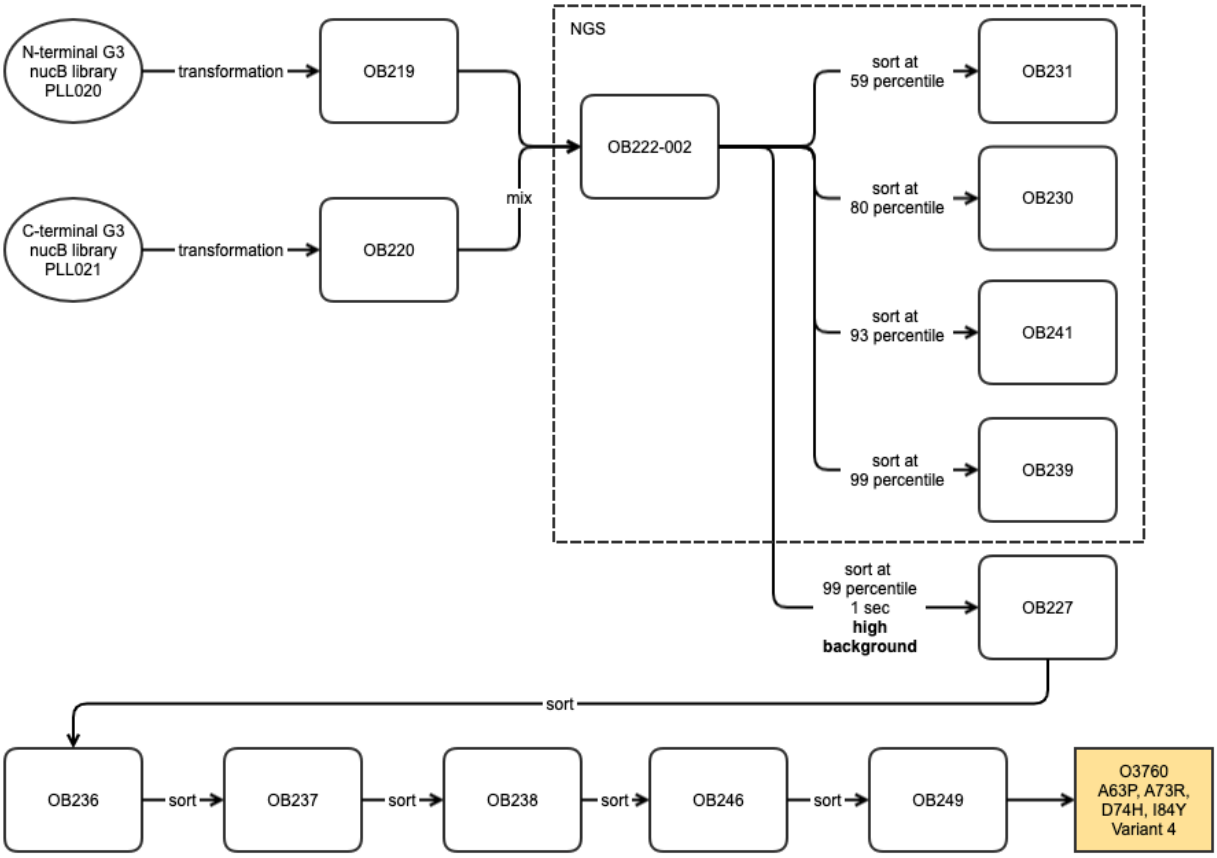

Supplementary Figure 21: Schematic of G3. *Four gates were used for data generation in G3, corresponding to different library fluorescence percentiles. An additional 6 sorts after a 99th percentile sort (not sequenced) led to the identification of the A63P,A73R,D74H,I84Y variant. All libraries that were sequenced using NGS are enclosed in dotted lines.*

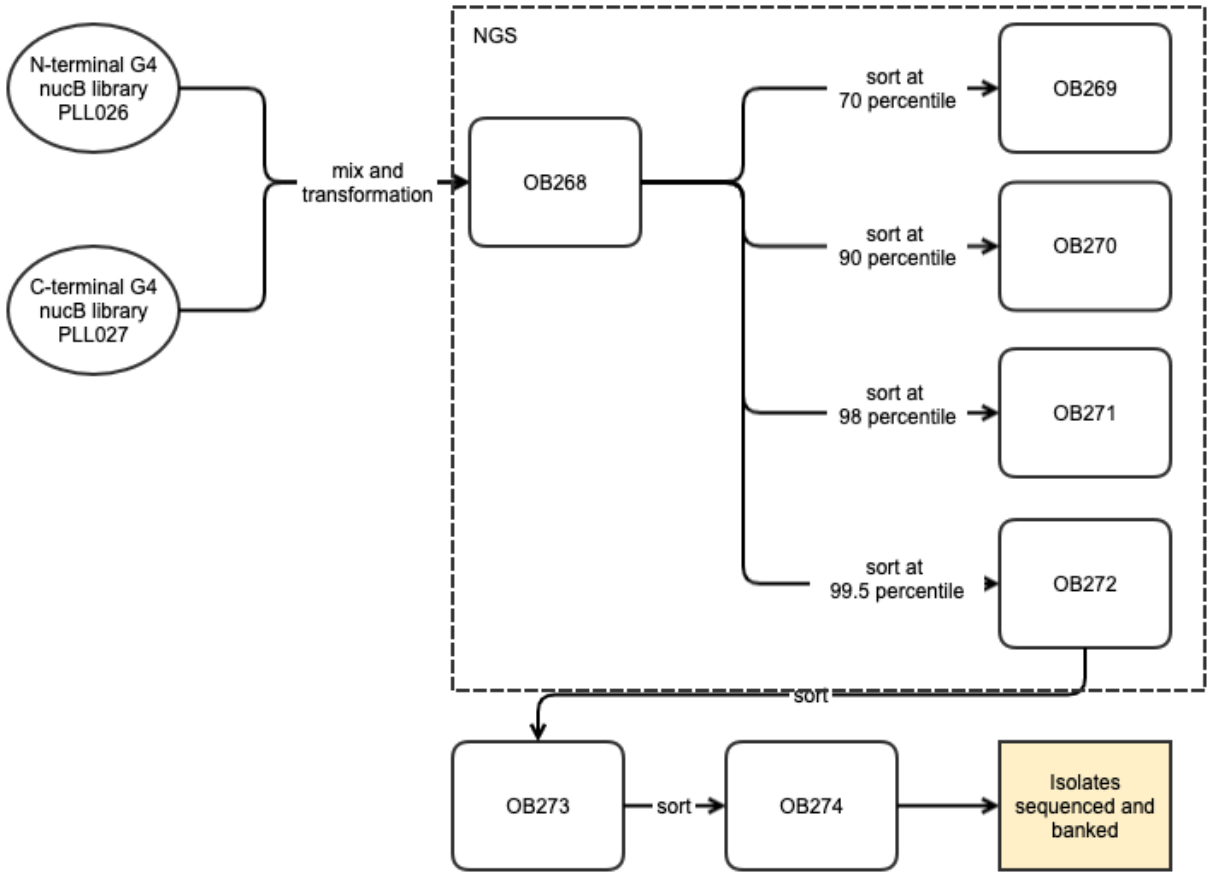

Supplementary Figure 22: Schematic of G4. *Four gates were used for data generation in G3, corresponding to different library fluorescence percentiles. All libraries that were sequenced using NGS are enclosed in dotted lines. The final isolates were sequenced and banked.*

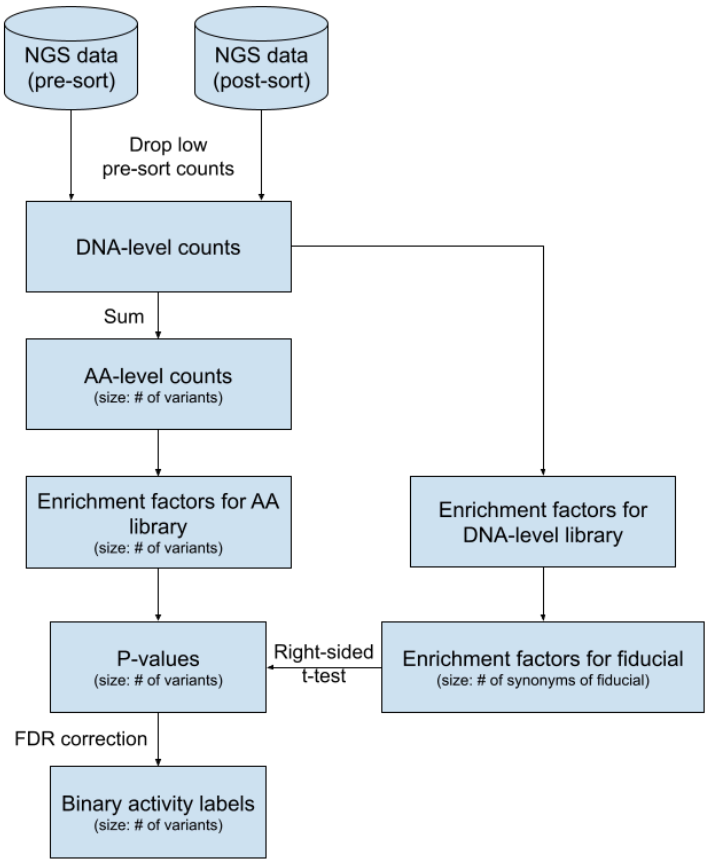

Supplementary Figure 23: schematic of data processing. *The per-variant activity labels are derived as follows: load all NGS counts for the screened library, drop variants with low input counts, compute enrichment factors at both the DNA and amino acid level, compute p-values for a right-sided t-test with the null distribution given by a fiducial's DNA-level enrichment factors, and label variants as having higher activity than the fiducial sequence, using a false-discovery rate correction.*

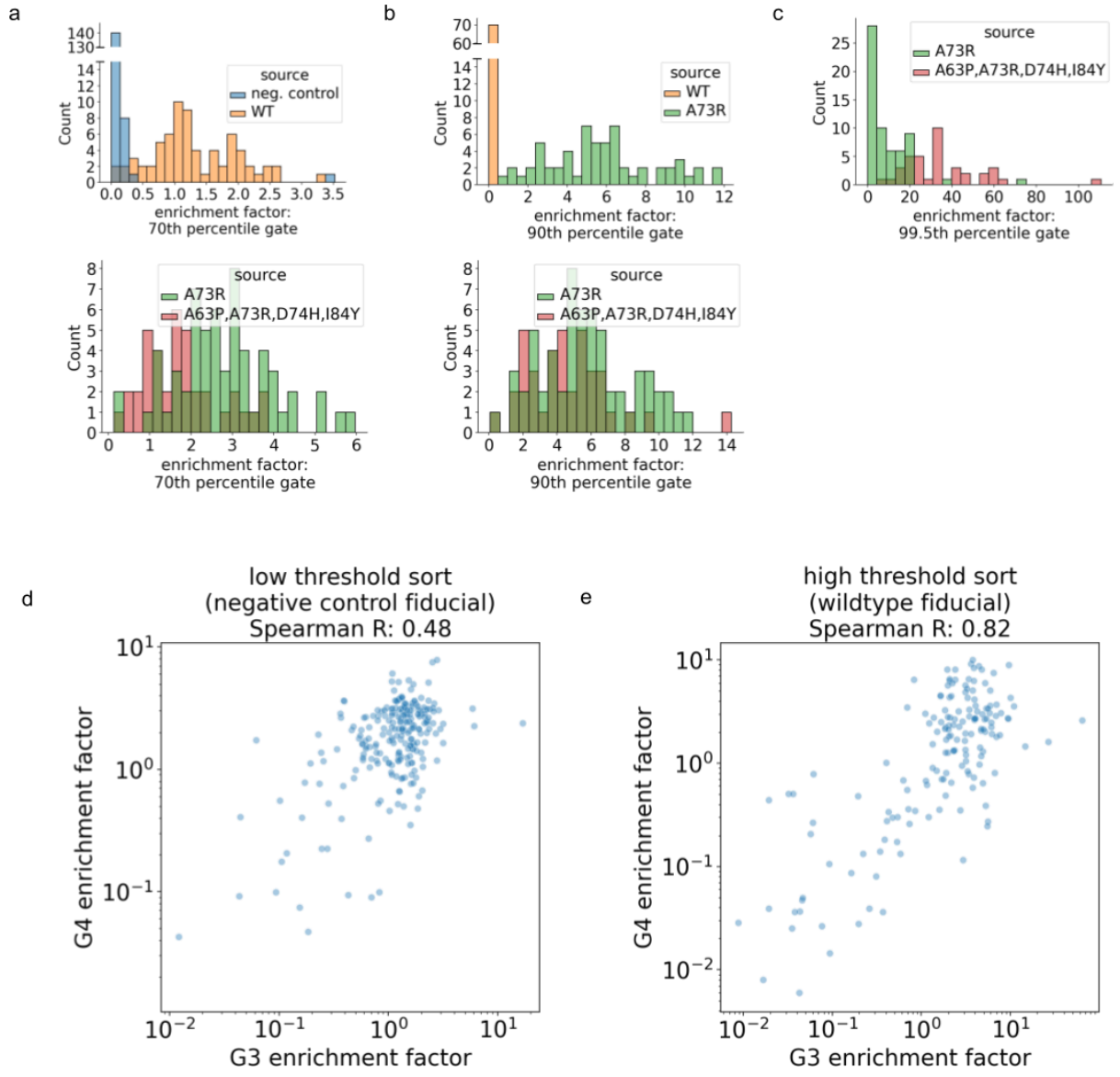

Supplementary Figure 24: sorts with higher fluorescence thresholds separate fiducials by activity while low threshold gates exhibit saturation behavior. *In (a), (b), and (c), the enrichment factor distribution of two fiducials is shown in a series of successively-higher gates used in G4, where the fluorescence threshold is lowest in (a) and highest in (c). Based on culture plate assays, we expect the activity of the fiducial sequences to be ordered by negative control < WT < A73R < quad, where "negative control" refers to stop codons introduced in the middle of the coding sequence, which should produce inactive proteins. We see that the gate used in (a) separates negative control and WT fiducials (top panel), the gate used in (b) separates WT and A73R fiducials (top panel). While the gate used in (c) separates A73R and quad (A63P, A73R, D74H, I84Y) fiducials (top panel), the lower threshold gates used in (a) and (b) are unable to separate the A73R and quad fiducials (bottom panel), as most replicates of high activity variants pass the lower threshold screen. In (d) and (e), we plot the enrichment*

factors for 251 functional variants screened in both G4 and G3. The G4 enrichment factor (y axis) and G3 enrichment factor (x axis) are plotted for the sorts used to determine activity level relative to negative control (d) and wildtype (e) fiducials, analogous to the negative control sort in subfigure (a) and wildtype sort in subfigure (b), respectively. The variants screened in both G3 and G4 were enriched for functional variants, and as such, we see enrichment factor saturation in the low threshold sorts (d), leading to a lower enrichment factor correlation across generations than in the high threshold sorts (e) (Spearman R 0.48 vs 0.82). However, our discrete activity labels were concordant across generations. Of the variants sorted with a threshold calibrated to the negative control fiducial (d), 206 were concordantly predicted to be better than the negative control in both G3 and G4, 24 were concordantly predicted to be worse than the negative control, and 21 were predicted discordantly. Of the variants sorted with a threshold calibrated to the wildtype fiducial, 131 were predicted to be better than wildtype in both G3 and G4, 96 were predicted to be worse than wildtype in both rounds, and 24 were predicted discordantly.

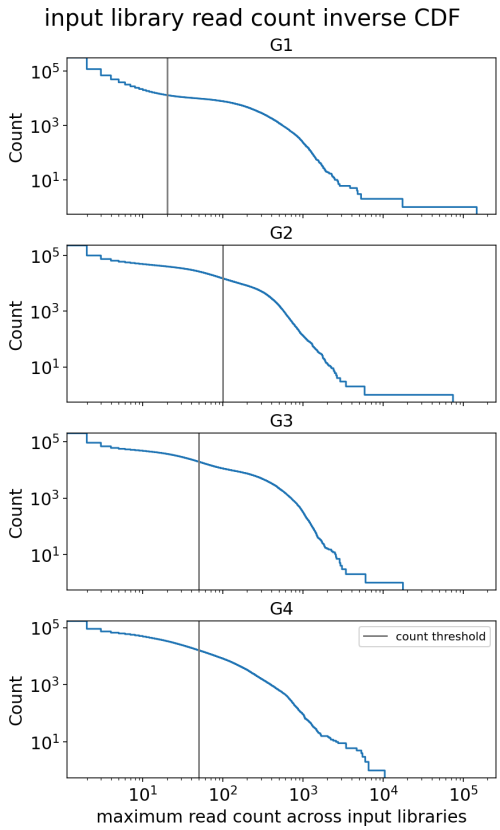

Supplementary Figure 25: Read count thresholding determines the number of unique variants we can characterize. *Read count thresholds were determined heuristically in each generation to assure accurate enrichment factor estimates. In order from G1 to G4 (top to bottom), the read count threshold was set to 20, 100, 50, and 50 reads, respectively. In each generation, this corresponds to filtering the library from ~10^5 (no thresholding) to ~10^4 variants (with thresholding).*

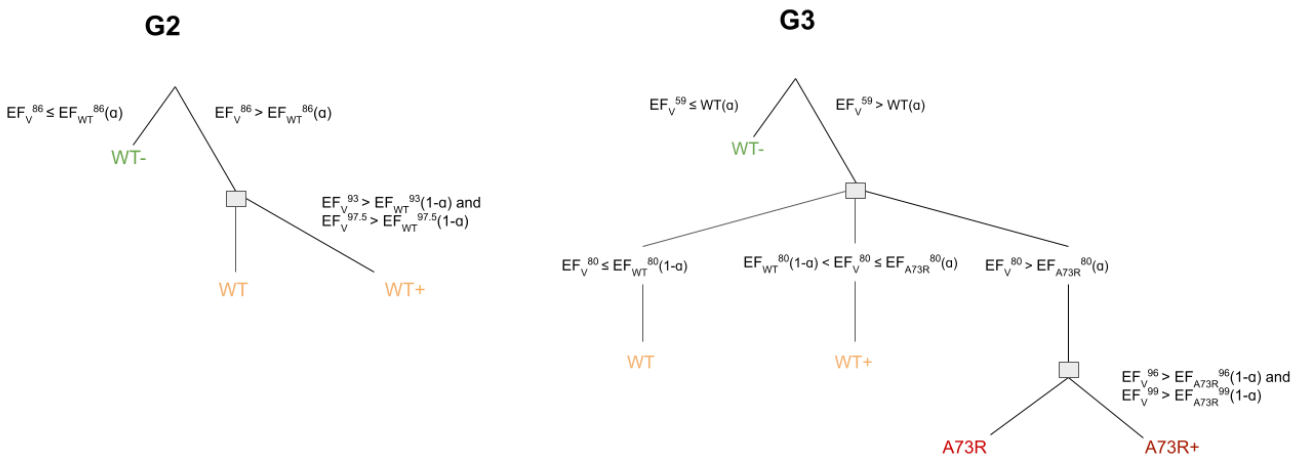

Supplementary Figure 26: Procedure for assigning discrete ML training labels for G2 and G3 data. *Activity labels were assigned through a series of comparisons, utilizing all sorts for which there was data. The variant V enrichment factor in a given sort is indicated by the library percentile of the sort ($EF_V^{sort\ percentile}$). Edges are labeled with the comparison used to make an assignment. $EF_{fiducial}^{sort}(\alpha)$ (e.g. $EF_{A73R}^{80}(\alpha)$) and refers to the α quantile of the empirical synonym enrichment factor distribution for the fiducial. The final label is in the set {WT-, WT, WT+, A73R, A73R+} and was used as a classification objective for model training.*

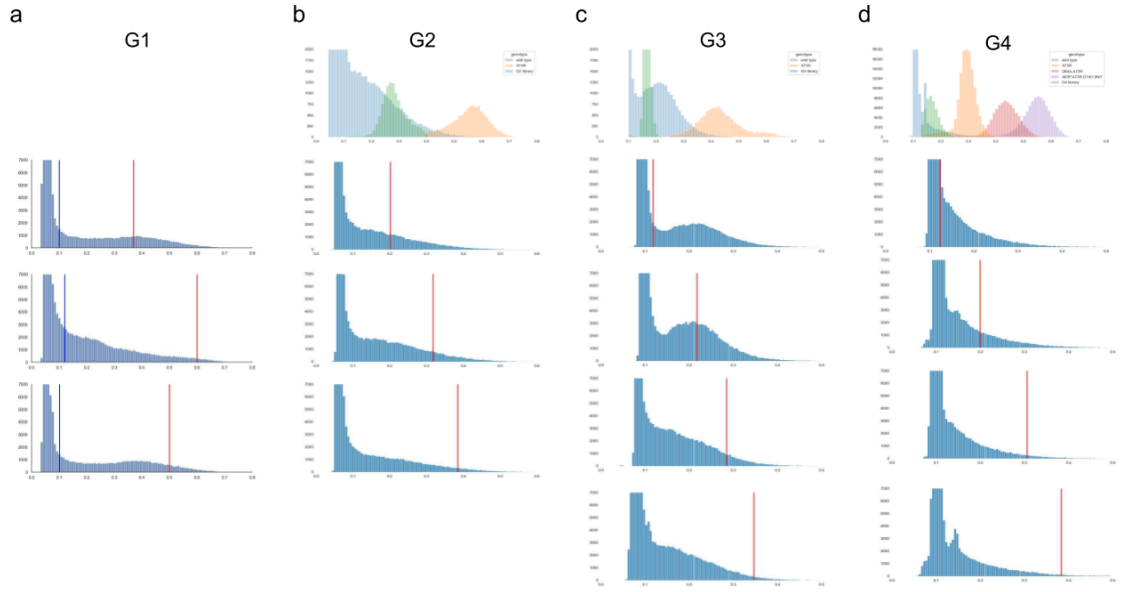

Supplementary Figure 27: Gate fluorescence thresholds compared to fiducial sequence fluorescence for all generations. *Columns a, b, c, and d correspond to screens of G1, G2, G3 and G4, respectively. The histogram in the first row show the overall library fluorescence distribution (blue) and the fiducial fluorescence distributions (WT in green, A73R in orange, D64A,A73R in red, and A63P,A73R,D74H,I84Y in purple). G1 was a random library, and does not include fiducials. The histograms in each subsequent row show the fluorescence level for each sort in that generation. The red line indicates the minimum fluorescence threshold for a cell to be sorted. In column a the low gate sort threshold is additionally indicated by the blue line, while the high gate sort threshold is indicated by the red line.*

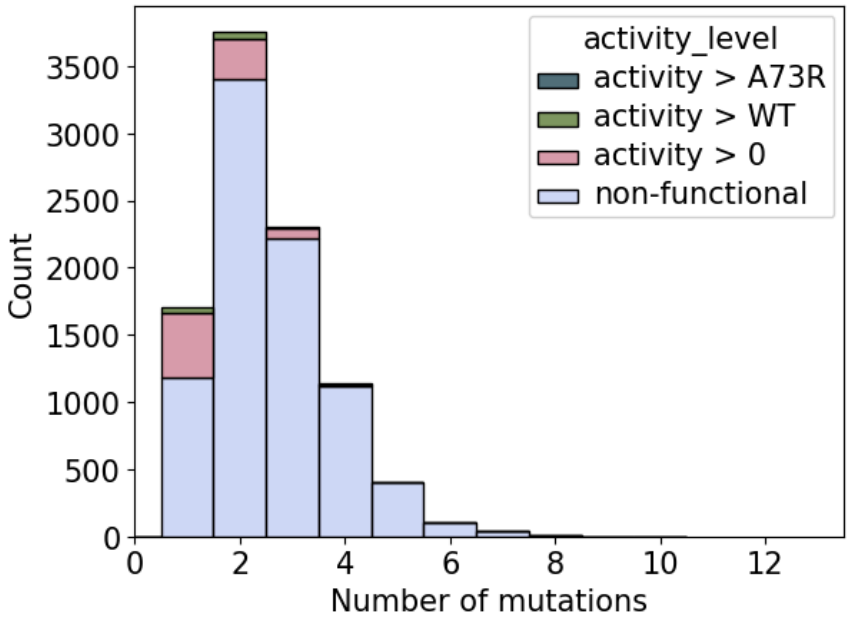

Supplementary Figure 28: Activity level distribution for G1. *G1 variants, colored by estimated activity levels. G1 included a single-site saturation mutagenesis library as well as variants generated by error-prone PCR. On average, G1 variants had 2.5 mutations, while functional variants had, on average, 1.6 mutations.*

Supplementary Tables

generation	name	library size	num hits (> neg_control)	hit rate % (> neg_control)	num hits (> WT)	hit rate % (> WT)	num hits (> A73R)	hit rate (> A73R)
g1	g1_eppcr	9441	1084.5 +/- 33.0	11.49 +/- 0.35	155.1 +/- 10.0	1.64 +/- 0.11	N/A	N/A
g2	g2_broad_recombination_sampling	3598	99.5 +/- 9.5	2.76 +/- 0.26	6.1 +/- 3.5	0.17 +/- 0.10	N/A	N/A
g2	g2_g1_plate_assay_variants	5	5.0 +/- 0.0	100.00 +/- 0.00	3.7 +/- 0.9	73.33 +/- 17.99	N/A	N/A
g2	g2_hit_recombination	951	830.9 +/- 12.5	87.37 +/- 1.32	470.0 +/- 10.1	49.42 +/- 1.06	N/A	N/A
g2	g2_mbo_dnn_exploit	287	104.5 +/- 9.7	36.40 +/- 3.37	43.1 +/- 7.5	15.03 +/- 2.63	N/A	N/A
g2	g2_mbo_dnn_explore	4083	1393.9 +/- 27.3	34.14 +/- 0.67	171.7 +/- 20.0	4.20 +/- 0.49	N/A	N/A
g2	g2_single_mutants	1402	384.4 +/- 12.7	27.42 +/- 0.91	43.0 +/- 6.3	3.07 +/- 0.45	N/A	N/A
g2	g2_stratified_sample	40	16.2 +/- 3.6	40.50 +/- 9.12	2.7 +/- 1.7	6.83 +/- 4.27	N/A	N/A
g2	g2_unmatched	4365	446.8 +/- 18.3	10.24 +/- 0.42	103.9 +/- 11.8	2.38 +/- 0.27	N/A	N/A
g2	g2_wt_synonyms	1	1.0 +/- 0.0	100.00 +/- 0.00	0.0 +/- 0.0	0.00 +/- 0.00	N/A	N/A
g3	g3_a73r_synonyms	1	1.0 +/- 0.0	100.00 +/- 0.00	1.0 +/- 0.0	100.00 +/- 0.00	0.0 +/- 0.0	0.00 +/- 0.00
g3	g3_g1_stratified_sample	38	12.9 +/- 3.0	33.86 +/- 7.89	2.1 +/- 1.9	5.44 +/- 4.92	0.0 +/- 0.0	0.00 +/- 0.00
g3	g3_g2_plate_assay_variants	6	6.0 +/- 0.0	100.00 +/- 0.00	4.9 +/- 0.8	81.11 +/- 13.90	0.0 +/- 0.0	0.00 +/- 0.00
g3	g3_hit_recombination	1712	1443.9 +/- 19.0	84.34 +/- 1.11	815.8 +/- 21.3	47.65 +/- 1.24	26.8 +/- 7.7	1.57 +/- 0.45
g3	g3_loop_explore	389	123.1 +/- 11.3	31.64 +/- 2.91	2.3 +/- 1.5	0.58 +/- 0.38	0.0 +/- 0.0	0.00 +/- 0.00
g3	g3_mbo_dnn_exploit	369	277.3 +/- 9.2	75.16 +/- 2.51	196.3 +/- 11.1	53.21 +/- 3.01	11.2 +/- 3.6	3.04 +/- 0.97
g3	g3_mbo_dnn_explore	299	233.4 +/- 6.9	78.06 +/- 2.32	174.3 +/- 8.4	58.28 +/- 2.80	7.7 +/- 3.0	2.59 +/- 1.00
g3	g3_prosar_high_screen_high	670	634.7 +/- 4.5	94.74 +/- 0.68	472.3 +/- 9.7	70.49 +/- 1.44	23.2 +/- 6.2	3.46 +/- 0.92
g3	g3_prosar_high_screen_low	2080	1690.9 +/- 9.6	81.29 +/- 0.46	979.7 +/- 24.7	47.10 +/- 1.19	20.2 +/- 7.3	0.97 +/- 0.35
g3	g3_prosar_high_unscreened	1315	766.9 +/- 16.1	58.32 +/- 1.23	362.1 +/- 16.2	27.54 +/- 1.23	1.0 +/- 2.0	0.08 +/- 0.15
g3	g3_prosar_low_screen_high	820	765.9 +/- 5.4	93.40 +/- 0.66	345.1 +/- 17.1	42.08 +/- 2.09	3.5 +/- 1.6	0.43 +/- 0.19

g3	g3_prosar_low_screen_low	1930	1568.3 +/- 18.1	81.26 +/- 0.94	707.5 +/- 20.7	36.66 +/- 1.07	7.6 +/- 3.3	0.39 +/- 0.17
g3	g3_prosar_low_unscreened	1108	711.3 +/- 14.7	64.20 +/- 1.32	245.9 +/- 14.0	22.20 +/- 1.27	4.5 +/- 2.3	0.40 +/- 0.21
g3	g3_single_mutants	577	221.1 +/- 9.6	38.32 +/- 1.66	4.1 +/- 2.2	0.70 +/- 0.38	0.0 +/- 0.0	0.00 +/- 0.00
g3	g3_unmatched	7796	3831.5 +/- 38.9	49.15 +/- 0.50	1853.0 +/- 36.8	23.77 +/- 0.47	76.3 +/- 13.0	0.98 +/- 0.17
g3	g3_wt_synonyms	1	1.0 +/- 0.0	100.00 +/- 0.00	0.0 +/- 0.0	0.00 +/- 0.00	0.0 +/- 0.0	0.00 +/- 0.00
g4	g4_a73r_synonyms	1	1.0 +/- 0.0	100.00 +/- 0.00	1.0 +/- 0.0	100.00 +/- 0.00	0.0 +/- 0.0	0.00 +/- 0.00
g4	g4_double_synonyms	1	1.0 +/- 0.0	100.00 +/- 0.00	1.0 +/- 0.0	100.00 +/- 0.00	0.0 +/- 0.0	0.00 +/- 0.00
g4	g4_g3_hit_constituents	241	234.1 +/- 2.0	97.15 +/- 0.81	209.1 +/- 4.2	86.78 +/- 1.74	1.4 +/- 1.1	0.58 +/- 0.44
g4	g4_g3_plate_assay_variants	14	14.0 +/- 0.0	100.00 +/- 0.00	14.0 +/- 0.0	100.00 +/- 0.00	0.4 +/- 1.1	2.86 +/- 7.54
g4	g4_hit_recombination	1540	1009.6 +/- 22.7	65.56 +/- 1.47	886.9 +/- 14.1	57.59 +/- 0.91	8.5 +/- 4.2	0.55 +/- 0.28
g4	g4_homolog_graft	11	5.6 +/- 1.8	50.91 +/- 16.76	0.0 +/- 0.0	0.00 +/- 0.00	0.0 +/- 0.0	0.00 +/- 0.00
g4	g4_mbo_dnn	1356	1095.5 +/- 15.4	80.79 +/- 1.14	1147.0 +/- 15.8	84.59 +/- 1.17	52.4 +/- 6.8	3.86 +/- 0.50
g4	g4_mbo_linear	280	2.1 +/- 1.3	0.76 +/- 0.47	13.7 +/- 3.5	4.90 +/- 1.24	0.0 +/- 0.0	0.00 +/- 0.00
g4	g4_mbo_seeds	27	27.0 +/- 0.0	100.00 +/- 0.00	26.0 +/- 0.8	96.30 +/- 3.13	0.4 +/- 0.7	1.48 +/- 2.73
g4	g4_other	4494	1147.9 +/- 40.7	25.54 +/- 0.91	944.9 +/- 28.6	21.03 +/- 0.64	0.7 +/- 1.1	0.02 +/- 0.02
g4	g4_quad_synonyms	1	1.0 +/- 0.0	100.00 +/- 0.00	1.0 +/- 0.0	100.00 +/- 0.00	1.0 +/- 0.0	100.00 +/- 0.00
g4	g4_sample_and_screen_dnn	1298	977.8 +/- 14.1	75.33 +/- 1.09	898.5 +/- 17.2	69.22 +/- 1.32	1.9 +/- 1.3	0.15 +/- 0.10
g4	g4_sample_and_screen_linear	568	186.1 +/- 12.8	32.77 +/- 2.25	114.1 +/- 8.0	20.08 +/- 1.40	0.0 +/- 0.0	0.00 +/- 0.00
g4	g4_sample_unscreened	592	161.3 +/- 12.8	27.24 +/- 2.16	113.3 +/- 11.6	19.13 +/- 1.97	0.0 +/- 0.0	0.00 +/- 0.00
g4	g4_unmatched	2360	425.4 +/- 20.1	18.03 +/- 0.85	330.3 +/- 16.0	14.00 +/- 0.68	1.9 +/- 2.3	0.08 +/- 0.10
g4	g4_wt_synonyms	1	1.0 +/- 0.0	100.00 +/- 0.00	0.0 +/- 0.0	0.00 +/- 0.00	0.0 +/- 0.0	0.00 +/- 0.00
g2 (alternative)	prosar+screen_g2_redux	1464	1034.5 +/- 15.3	70.66 +/- 1.04	559.3 +/- 19.5	38.21 +/- 1.33	0.0 +/- 0.0	0.00 +/- 0.00
g1 (alternative)	zero_shot	1235	629.0 +/- 22.3	50.93 +/- 1.81	134.8 +/- 10.8	10.91 +/- 0.87	0.0 +/- 0.0	0.00 +/- 0.00

Supplementary Table 1: hit rates of all sub-libraries for both the WT and A73R fiducials. *Note that the total number of hits here is not consistent with the activity labels in our final genotype-phenotype fitness landscape file. This is because we applied a Benjamini-Hochberg false discovery rate correction within each row in this table, whereas it was applied globally when producing the landscape.*

generation	name	library size	num hits (> A73R,D74S)	hit rate (> A73R,D74S)
g4	g4_hit_recombination	1540	1.4 +/- 2.1	0.09 +/- 0.13
g4	g4_mbo_dnn	1356	29.1 +/- 6.9	2.15 +/- 0.51
g4	g4_mbo_seeds	27	0.5 +/- 1.2	1.73 +/- 4.61
g4	g4_quad_synonyms	1	1.0 +/- 0.0	100.00 +/- 0.00
g4	g4_sample_and_screen_dnn	1298	1.9 +/- 1.6	0.14 +/- 0.12

Supplementary Table 2 hit rates for G4 libraries for the A73R,D73S fiducial. *For brevity, only sub-libraries with non-zero hit rate are included. Note g4_quad_synonyms contains synonyms for a high-performance fiducial, so its hit rate is high by construction.*

Generation	Type of Sequence	Total number of variants used as input to design the library	Number of designed variants that data was obtained for
G1	-	-	9441
G2	HR	9441	951
G3	HR	10600	1712
G4	HR	13252	1540
G2	ML	9441	9370
G3	ML	24173	9557
G4	ML	43284	8588

Supplementary Table 3: Overall library sizes for ML and HR campaigns. *The third column reports the total number of variants considered so far by the campaign. For ML, this is the size of the model training set that aggregates data from all prior generations. HR recombined hits from the previous round of experiments and did not explicitly use data from prior rounds. However, for the sake of consistency we report the cumulative number of unique variants considered across rounds for both methods. Note that the third column is not simply the cumulative sum of the fourth column, since additional data was available for variants that arose from DNA synthesis and replication errors (referred to as "unmatched" in Supplementary Table 1). See 'Hit recombination' in Methods for details regarding how each round's data was used by HR. Our full genotype-phenotype landscape includes additional variants, for example, positive and negative controls.*

Parameter Name	Non-Default Values
Sklearn logistic regression	
C	logspace(1e-4, 1e4, 10)
'max_iter'	1000
LGBM classifier	
learning_rate	[0.01, 0.05, 0.1, 0.2, 0.4, 0.6]
n_estimators	[64, 100, 128]
CNN	
batch_size	256
epochs	[2000, 3000]
learning_rate	[0.001, 0.00005]
dropout_rate	[0.05],
num_conv_layers	[0, 1, 2]

Supplementary Table 4: Hyper-parameter grids for supervised models. *Each model was tuned over a subset of hyper-parameter values that were established as reasonable ranges using prior investigations on other protein fitness datasets.*

model	**hits@1000_wt**	**hits@1000_A73R**
Linear	0.44	0.09
LGBM	0.71	0.15
CNN	0.82	0.21

Supplementary Table 5: Results for the best hyper-parameter setting for supervised models. *We trained 3 models: linear logistic regression from sklearn [125], a gradient-boosted decision tree implemented using the LGBM package [126], and a convolutional neural network implemented in keras with tensorflow[127] using an ADAM optimizer with default hyper-parameters.*

Generation	Library ID	Sort Percentile	Raw Reads	Merged Reads	Aligned Reads (not indels)	Indels
G1	**OB133-3-1**	N/A	957949	627457	626924	58419
G1	**OB133-3-2**	N/A	958026	620219	619680	64609
G1	**OB133-3-3**	N/A	1500000	965560	964742	98036
G1	**OB141**	Low Gate 1	992370	568382	567963	31143
G1	**OB142**	High Gate 1	1064074	684620	684137	25680
G1	**OB145**	High Gate 2	715124	430440	430153	18339
G1	**OB146**	Low Gate 2	1012146	602674	602262	29599
G1	**OB149**	High Gate 3	2264079	1605909	1605907	58407
G1	**OB150**	Low Gate 3	1479973	1012855	1012239	37917
G1 reseq	**OB133-3-1**	N/A	8796092	5021977	5018574	4640424
G1 reseq	**OB133-3-2**	N/A	6652302	4288809	4285469	3927337
G1 reseq	**OB145**	High Gate 2	5042739	2960423	2958639	2843013
ML G2	**OB188 NS 1**	N/A	4405113	3813180	2385507	220066
ML G2	**OB188 NS 2**	N/A	2955910	2542995	2507476	75533
ML G2	**OB193**	86	1603156	1388681	1369732	45585
ML G2	**OB194**	97.5	1569513	1365392	1348237	43699
ML G2	**OB196**	93	4302646	3772972	2540279	239685
ML G2	**OB188**	N/A	14472539	13493968	8739074	1102314
ML G3	**OB222-002**	N/A	2154847	1881694	1552418	384799
ML G3	**OB222-002**	N/A	1861556	1605073	1321291	333557
ML G3	**OB222-002**	N/A	2224181	1948395	1621873	389077
ML G3	**OB222-002**	N/A	2126053	1904016	1573763	388317
ML G3	**OB222-002**	N/A	3393046	2659408	2165138	558286
ML G3	**OB222-002**	N/A	2883162	2327413	1912344	482233
ML G3	**OB230**	80	1379986	1199077	1194422	57309
ML G3	**OB231**	59	2408748	2120119	2098794	117612
ML G3	**OB239**	99	2626136	2065878	2057901	126476
ML G3	**OB241**	93	2372781	1879010	1873513	90589
ML G4	**OB268**	N/A	11923629	11233345	5248728	2462416
ML G4	**OB269**	70	1902601	1799002	1668940	87817
ML G4	**OB270**	90	2719025	2572901	2439231	99799
ML G4	**OB271**	98	2455165	2338449	2225624	87312
ML G4	**OB272**	99.5	1736640	1644487	1533991	80748

Supplementary Table 6 : Sequencing depth and NGS statistics for each library of variants.

	Fluorescence Threshold (low)	Percentage Droplets Sorted (low)	Fluorescence Threshold (high)	Percentage Droplets Sorted (high)
Sort 1	**0.100**	**5.947%**	**0.501**	**0.005%**
Sort 2	**0.115**	**9.228%**	**0.600**	**0.285%**
Sort 3	**0.100**	**6.344%**	**0.370**	**1.659%**

Supplementary Table 7: G1 sorting gate statistics. I*n G1 each sort was run with a low gate followed by continued sorting at a high gate. "Percentage droplets" indicates the percentage of droplets that passed the gate, where lower percentages indicate more stringent sorts at higher fluorescence threshold.*

	Percentile cells (target)	Fluorescence threshold	Percentage Droplets Sorted
G2			
Sort 1	**96%**	**0.201**	**0.32%**
Sort 2	**93%**	**0.318**	**0.83%**
Sort 3	**97.50%**	**0.385**	**1.95%**
G3			
Sort 1	59%	0.118	5.73%
Sort 2	80%	0.217	2.63%
Sort 3	95%	0.285	0.65%
Sort 4	99%	0.346	0.12%
G4			
Sort 1	70%	0.124	4.25%
Sort 2	90%	0.199	1.51%
Sort 3	98%	0.306	0.26%
Sort 4	99.50%	0.384	0.17%

Supplementary Table 8: sorting statistics for gates in G2, G3, and G4. *"Percentile cells" indicates the percentile of the cell-containing library we targeted for sorting. "Percentage droplets" indicates the percentage of droplets that passed the gate, where lower percentages indicate more stringent sorts at higher fluorescence threshold.*

Supplementary Text

S1: Composition of the ML library in each round

MBO-DNN

G2
model: We used a CNN regression model with 3 convolutional layers containing 32 width-5 filters and two fully-connected layers of width 64. The input to the model is a shape = [sequence_length, 20] one-hot-encoded array. After selecting a model architecture and training optimizer hyper-parameters using cross validation, we retrained the model on all available data using 5 replicates with different random parameter initialization. The model score used by MBO is the average prediction of this ensemble. Unlike other rounds, we fit models on a continuous-valued transformation of enrichment factors (Supp. S7), though in hindsight we feel that the discrete labeling used in subsequent rounds was more reliable.

candidate generation: First, we drew 500M samples from the 'broad exploration sampling' distribution.
mbo-dnn-exploit: take all samples with score > 3.
mbo-dnn-explore: take all samples with score > 0.

batch selection: same as G4; with restrictions on mutation usage and a specified target distribution over number of mutations from WT.

Note that the ML2 variant A73R,D74S in Figure 2b was proposed by mbo-dnn-explore.

G3
model: We used a similar approach as in G2, except that the model had 3 convolutional layers of 32 width-5 filters and a single fully-connected layer of width 64. The model was fit on discrete activity labels.

candidate generation: We recombine candidates from two approaches: (1) the same local-search technique as used in G4 and (2) samples from the G3 Prosar methods.

batch selection:
mbo-dnn-exploit: the top-200 candidates, ranked by model score.
mbo-dnn-explore: same as G4; with restrictions on mutation usage and a specified target distribution over number of mutations from WT.

G4
Described in the Methods section.

Prosar

We can trade off exploration and exploitation by varying the size of the set of mutations that are recombined *in-silico,* or equivalently, the threshold on estimated single-mutant effect used for selecting mutations. Mutation effects are estimated using a ridge regression model, where we tuned the weight on the regularization term using cross-validation to maximize the roc-auc score for finding variants with activity comparable or better than the WT. A mutation's score is the model's prediction for a sequence defined by applying the mutation to the WT minus the prediction for the WT. In G3 we use 'prosar_high' and 'prosar_low' to denote the use of mutation effect score thresholds of 2.0 and 0.5.

Prosar+Screen

This approach further filters samples from Prosar using a VAE homology model, and here we can vary the VAE score threshold used for rejecting variants as a secondary knob for training off exploration and exploitation. We use 'prosar_x_screen_y' to denote filtering samples from prosar_x (see above) using either a high or low VAE score threshold y. These thresholds were set heuristically by examining the distribution of VAE scores for samples from prosar_x. The VAE likelihood of a given variant is estimated using importance sampling from the posterior with 2500 samples.

prosar+screen_g2_redux

Prosar+screen worked well in G3 and we were curious to see how well it would have performed in G2, where only the G1 epPCR was available. The VAE score threshold was set heuristically to the 90th percentile of scores for sampled recombination variants with 4 mutations, which resembles the high-threshold filtering used in G3. We heuristically defined the mutation set as the top 45 mutations, since this was about the size of the mutation set used in the best prosar+screen system from G3.

sample-and-screen-linear

This is an ablation of the G4 sample-and-screen method described in the Methods section where we use a linear model instead of a neural network to classify a variant's activity level.

mbo-linear

This is an ablation of the G4 mbo-dnn where we used a linear multi-class logistic regression model.

g4_g3_hit_constituents

For a given multi-mutation variant X, the set of 'constituents' of X is all possible variants that combine subsets of the mutations in X. In G4 we include the constituents of a few top-performing variants from the G3 liquid culture plate assay.

S2: Discussion of hit-rates for additional sub-libraries

G2 sublibrary hit-rates

Broad recombination sampling (BRS) sampled combinations of mutations from the G1 data that were inferred to be non-deleterious to protein function. However, as seen in Supplementary Figure 1, BRS performed quite poorly. In hindsight, we were too permissive in defining this set of non-deleterious mutations (see 'broad recombination sampling' in Methods). Since we sample variants with many mutations, many variants probably contained at least one false-positive mutation. MBO-DNN-Explore screened samples from BRS using a neural network model. This is marginally better than BRS, but was still hurt by the overall low quality of the pool of samples. MBO-DNN-Exploit performed comparably to hit recombination (HR). Had BRS been tuned to perform better, it may have led to downstream improvements in the overall campaign.

G3 sublibrary hit-rates

The purified protein results shown in Figure 2 confirm that G3 contained at least one variant with activity much better than A73R. This is also confirmed by our hit calling procedure based on NGS counts, where we see in Supplementary Table 1 that many G3 sublibraries proposed variants that were labeled as having activity higher than A73R. For example, MBO-DNN-Exploit found 11 such variants. However, the hit rates for finding such variants are sufficiently low that we cannot stratify the analysis by num_mutations.

In response, we analyzed methods' hit rate for designing variants with activity greater than WT. We consider the HR campaign and the key versions of the two types of ML-based design approaches in our G3 portfolio: MBO-DNN and Prosar+Screen. We find that these outperformed hit recombination (HR). However, there are a number of hyper-parameters for each that impact performance and may be difficult to set in advance. In Supplementary Figure 2, for example, we see that both MBO-DNN systems performed similarly, but the left panel of Supplementary Figure 3 demonstrates that Prosar+Screen was sensitive to the parameters we used to trade off exploration and exploitation.

Prosar+Screen Ablations

In Supplementary Figure 3 (left) we analyze the G3 sub-libraries designed using the Prosar+Screen method with different design choices for trading off exploration and exploitation, including 'Prosar' which performs no screening with a zero-shot model. See Prosar+Screen in Section S1 for the prosar_x_screen_y notation. First, we find that all Prosar+Screen versions outperformed Prosar for designing variants with many mutations. Second, the exploit-focused versions of the method had the highest hit rates.

Drawing on the success of Prosar+Screen in G3 and the small number of active variants in the G2 library due to the BRS sampling (see above), we investigated how Prosar+Screen would have performed in G2 as an alternative library design approach (see 'g2 redux prosar+screen' above). We find in Supplementary Figure 3 (right) that it was significantly better than hit

recombination in G2 (HR-G2) at designing variants with many mutations and is an interesting competitor to HR-G3.

Sample+Screen Ablations

In G4, we ran an investigation to analyze the impact of our classification model for screening variants. We ran two versions of Sample+Screen, where a large pool of candidate variants is sampled from a VAE that was trained on a combination of homologs and G1-G3 hits and then filtered using a classification model. In Supplementary Figure 4 (left) we consider methods' ability to find variants with activity higher than the WT and find that filtering using our convolutional neural network (Sample+Screen-DNN) is significantly better than filtering using a linear model (Sample+Screen-Linear), which performs about the same as using raw samples with no filtering (Sample-Unscreened). We also contrast Sample+Screen-DNN with MBO-DNN, which uses local search to find high-scoring candidates instead of ranking a fixed pool of samples and find that MBO-DNN performs better. In Supplementary Figure 4 (right) we consider the methods' ability to find variants with activity higher than A73R. Here, MBO-DNN is dramatically better than Sample+Screen. We expect this is because including the homology data when training the sampling model biases the samples away from the known experimental hits towards the variability of the natural homologs. For MBO-DNN, however, it optimizes a model-based fitness landscape based entirely on experimental data.

S3: Zero-shot results

A: Benchmarking Zero-Shot Scoring

Our zero-shot VAE model provides two capabilities: scoring the likelihood of a given variant and sampling a novel variant. There are many other computational methods that also provide these, ranging, for example, from context-independent models of amino acid substitution probabilities to deep neural networks that define a full joint distribution over variable-length protein sequences. Here, we evaluate a collection of such models in terms of their ability to perform zero-shot scoring on the G1 epPCR data.

In Supplementary Figure 5 and Supplementary Figure 6 we provide the same figures as Figure 5a and b, but using scores from 4 different approaches: our VAE, the 650M-parameter ESM-1b model[71], a profile hidden Markov model (pHMM) fit using the hmmer package[72] on the same alignment used to train the VAE, and context-independent scoring using substitution scores from the BLOSUM62 matrix[128]. In Supplementary Figure 5 we show qualitatively that the VAE scores provide the most noticeable separation between functional and non-functional variants.

In Supplementary Figure 6 we analyze methods' ability to filter a library to a smaller size while still keeping the hits. The rows of the grid of sub-figures correspond to which level of activity is used to define a hit and columns correspond to which set of variants we analyze. In the top row, we analyze models' ability to identify variants with non-zero activity. This is a setting where we expect zero-shot scoring to perform well, since mutations that render a protein non-functional may be easy to infer using patterns of conservation in natural sequences. In the bottom row, we explore models' ability to identify variants with activity that is greater than WT, which is a primary protein optimization goal. In the left column, analyzing variants with num_mutations = 1 reflects a use-case constrained by low-throughput experiments where assaying even all single-mutant variants of a starting sequence would be infeasible, and thus it would be helpful to filter this set *in-silico*. On the right, we consider all G1 variants with multiple mutations, which probes models' ability to identify epistatic interactions. One challenge with the right figure is that enzyme activity is correlated with the number of mutations from WT. To control for this, we only consider variants with exactly two mutations in the middle column. Overall, we find that the VAE performs comparable or better than the alternative methods across this range of evaluation settings.

B: Comparing Zero-Shot Sampling to Homolog Grafting

‘Homolog grafting’ is a model-free zero-shot design approach that incorporates groups of mutations appearing in nearby homologs to the WT (Methods). Of the 11 homolog grafting variants, 5 ± 2 were functional (Supplementary Table 1), similar to the overall hit rate of the VAE-designed zero-shot library (hit rates for functional variants of 50.9 ± 16.8% vs 50.9 ± 1.8%, respectively). While this model-free approach showed a promising hit-rate, natural homologs are often quite far from the wildtype sequence, so generating a large library within a certain mutational distance of the WT is not straightforward, as grafting from a distant homolog would

result in many mutations. VAE sampling, on the other hand, trains a model on distantly-related homologs, but can sample many new nearby neighbors of the WT.

S4: G4 MBO-DNN Model Selection

We assess model performance using the following steps:

1) Create a train-test split of the G1, G2, and G3 data by using all variants with less than or equal to two mutations for training and the remainder for testing.
2) Give each variant two binary labels using the procedure described in Section S7: whether it has activity higher than the WT and whether it has activity higher than A73R. These were then merged into a single multi-class label. Of note is that we do not perform any EFDR correction when producing these labels; each variant is processed independently.
3) Train models using a multi-class classification loss.
4) For each model and for each activity level, define a sequence-to-scalar ranking function as score(sequence; activity_level) = P(sequence | activity_label >= activity_level). For example, score(sequence; WT) = P(sequence | label = WT) + P(sequence | label = A73R).
5) compute hits@1000_wt, the fraction of the 1000 variants with highest score(sequence; WT) that have been labeled as better-than-WT. And similarly, compute the hits@1000_a73R metric, where variants are ranked using score(sequence; A73R).
6) To optimize over hyper-parameters for each model, we sorted by the hits@1000_A73R metric, as we felt this best reflected our goal of finding new, improved variants. See Supplementary Table 4 and Supplementary Table 5 for hyperparameters and model performance metrics.

S5: Algorithms used in our MBO systems

The model defines a mapping from an amino acid sequence to a real-valued score, and our goal is to select a batch of new, diverse variants with high model scores. For the sake of simplicity, we restrict the search space for MBO to only consider substitutions to the wildtype sequence. Therefore, every variant can be expressed as a list of single-point mutations to the wildtype.

Candidate generation with local search optimization

First, we seek to find a large set of high-scoring sequences, with the assumption that a small, diverse subset of these can then be selected downstream. We proceed with the following steps:

A. We curate a list of 15 'seed' sequences that had high activity in the previous round of experiments.
B. Starting at each seed, we run a randomized local search optimizer that incrementally builds up variants with high model scores by adding mutations to the seed.
C. We pool the results across multiple seeds, multiple algorithms for step (B), and 100 random optimization trajectories for each method for each seed.

Each step i of the iterative local search procedure (B) can be seen as taking a population P[i] of (sequence, model score) pairs and proposing a new set of child sequences C[i] that hopefully improve the model score. The model is then applied to C[i] and the result is appended to P[i] to obtain P[i+1]. We use three different methods for proposing C[i] from P[i]:

1) Single-mutant walk: we uniformly sample a parent sequence from one of the top-20 sequences in P[i], then we define C[i] as all possible single-mutation neighbors of the parent.
2) Sub-sampled single-mutant walk: we uniformly sample (with replacement) 500 different parent sequences from the top-20 sequences in P[i]. For each parent, we sample a single-mutation neighbor.
3) *A Regularized evolution*[129] extension of (2), where the sampling of parent sequences is informed by the model score as well as how recently the sequence was first added to the population.

Batch selection with greedy algorithm constraining mutation usage

Given a large list of (sequence, model score) pairs, we seek to select a subset that have high model score and are also diverse. We found that simply taking the top-N sequences by model score resulted in certain mutations appearing in nearly all variants. While there may be experimental evidence to suggest that these mutations were good, we further diversified to correct for model overconfidence. Therefore, we use the following greedy algorithm:

1) Sort the candidates by model score in decreasing order. Express each sequence as a list of (old amino acid, position, new amino acid) mutations.

2) Select the top candidate from the sorted list. Discard the candidate if any of its mutations appear more than M times in the pool of candidates selected so far. Otherwise, include it in the pool of selected candidates.
3) Repeat (2) until N candidates have been selected.

S6: Additional details about assays of enzyme activity

6A Isolating the highest activity variants using a liquid culture plate assay

After stringently sorting at successively higher thresholds, cells that pass the selection were plated and single colonies screened in a “Tier 1” liquid culture plate assay. In Tier 1, each colony was assayed (Methods: Liquid Culture Plate Assay) in a single well on a 96-well plate that included controls of high activity variants selected in prior rounds. The ranking of activity (normalized by optical density) in Tier 1 was used to identify high performing variants that were genotyped and promoted to “Tier 2”. In Tier 2, each variant was assayed at higher replication to confirm their relative ranking. High performing variants in the Tier 2 screen were promoted for protein purification and assayed for specific activity. Results for Tier 1 and 2 screens for all generations are presented in Supplementary Figure 8 - Supplementary Figure 13.

6B Specific activity assay

To determine the specific activity of a purified variant we compare the reaction kinetic curves between the variant of interest and the wildtype at a series of enzyme concentrations, as described in Methods: Nuclease activity assays. In Supplementary Figure 14 we present an example kinetic curve and describe how we compute specific activity.

6C Biofilm disruption assay

In Supplementary Figure 15 we evaluate the ability of the purified nuclease variants to disrupt *Bacillus licheniformis* biofilms. *B. licheniformis* was cultured in 10 mL of LB at 37°C and 220 rpm for 2 days. The culture was then diluted 1:100 into fresh LB media and dispensed in 150-µL volumes into the wells of sterile, 96-well, clear round-bottom plates for biofilm to develop for 2 days at 37°C and 100 rpm. The biofilms were disrupted by pipetting, and the residual biofilm left on the plate walls was gently washed three times with 200 µL saline. The washed residual biofilm was incubated at 37°C and 100 rpm with 200 µL of purified enzyme (a dilution series in 25 mM Tris, pH 7.5, 0.1% pluronic and 2.5 mM $MnSO_4$) for 20 h. The remaining biofilm was washed in 200 µL saline three times, and incubated with 200 µL of 0.1% crystal violet for 10 minutes at room temperature before being removed by aspiration, and washed once with saline. The now-stained, residual biofilms were then disrupted by adding 200 µL of 96% EtOH and 2% acetic acid and transferred to a flat-bottom plate to measure absorbance at 590 nm. Each variant’s biofilm disruption ability is determined by dividing absorbance at 590 nm by the average absorbance of a no-enzyme control, which yields the percentage of biofilm remaining after digestion.

6D Dependence of wildtype nuclease activity on pH

To determine how the wildtype activity differs under different pH conditions, we conducted enzyme activity assays using several buffers to cover a pH range from 6 to 11, see Supplementary Figure 16. These assays consisted of 25 mM buffer, 0.1% pluronic, 2.5 mM MnSO4, 50 uM G25/G24, 0.2 uM G651/G537, while the enzyme buffer also contained 25 mM

buffer with 0.1% pluronic. Rates were determined from the linear region of the kinetic curve. corresponding to 30-750s. Note that most assays are conducted with 100mM buffer concentrations to compensate for the alkalinity in spent media, but in this assay only 25mM was used because the enzyme was diluted in matched pH buffer before the assay. In our kinetic assays, the MOPS buffer was used.

Our protein engineering campaign was conducted at pH 7, and we report relative activity everywhere with respect to the wildtype enzyme at pH 7 unless otherwise specified. A 5.9-fold improvement relative to the wildtype is necessary to restore the enzyme to its maximum activity (i.e. its activity at pH 9), an 11.8-fold improvement in our campaign would imply an enzyme with 200% activity of the maximum at pH 9, etc.

S7: Generating ML Training Labels

In the Methods section, we describe a procedure for calling 'hits' with respect to a fiducial sequence, i.e., a set of variants with activity that is likely above that of a fiducial sequence. This approach was used when reporting all results about hit rates and to create the final dataset that we have released. Note, however, that we also needed to generate a dataset of sequences and corresponding activity labels during each round of the campaign for training the machine learning models that would design the next round, and our approach for creating this differed from the above procedure in a few key ways.

First, we did not perform any false-discovery rate correction; each variant was compared to fiducial sequences independently. This increases the false-positive rate of our labeling, which we felt was desirable to increase 'optimism in the face of uncertainty', a general design principle for trading off exploration and exploitation in model-based optimization[130]. Second, we performed both right and left-sided tests with respect to fiducials. This was used to provide fine-grained labels, such as 'WT+', where the activity is labeled as better than WT, but worse than A73R. Third, some variants appeared in multiple rounds. To reconcile potentially conflicting labels across rounds, we took the label from the most recent round.

Our labeling approach for G2 and G3 (i.e. the training data used to design G3 and G4) can be represented as a decision tree, which we established heuristically by reasoning about which gates had resolution for labeling activity as higher or lower than which fiducials. We visualize these decision trees in Supplementary Figure 26**.** Let, for example, EF_{A73R}^{sort} (1-α) refer to the (1-α) quantile of the enrichment factor distribution of the synonyms of fiducial A73R in a particular sort. If a variant has an enrichment factor greater than EF_{A73R}^{sort} (1-α) quantile of a fiducial, we label the variant as being “better” than A73R. If it has an enrichment factor greater than the (α) quantile, we label the variant as being “comparable” to A73R. We do such comparisons at each node in the decision tree, using different fiducials and different gates.

Finally, to design generation G2 using MBO-DNN, we used continuous regression targets for each G1 variant instead of discrete activity labels. In hindsight, these were more noisy than we thought, and we would use discrete labels if we were re-designing G2 again. This can be seen in our 'g2 redux' investigation, which was based on discrete labels. There were 3 high threshold sorts and 3 low threshold sorts, each with negative control and WT fiducials. We computed the mean μ and standard deviation σ of the WT fiducial distribution (trimmed at the top/bottom 1% to remove outliers). Then, for each variant we computed the z-score of its enrichment factor $z_V^{sort} = EF_V^{sort} - \mu_{WT}^{sort} / \sigma_{WT}^{sort}$. To combine the information across all sorts, for each variant we assigned an aggregate score by taking the max z score across the 3 high threshold sorts, and clipping the scores to be between [-4, 4]. In addition, any variant with an enrichment factor <= 1 in all low threshold sorts was mapped to score = -4.

S8: Gate Selection

For each sort, we had to select fluorescence thresholds for sorting cells to enable us to characterize variants at different levels of activity. Selecting at higher fluorescence thresholds selects for higher activity. With the exception of the first generation, we selected gates based on the fluorescence distribution of fiducial sequences; activity relative to fiducials was then used to characterize our high-throughput libraries. Our procedure for determining our gates was as follows. We first performed a fluorescence read experiment with fiducial sequences together with the library to determine the fluorescence distribution of our fiducials and our library. For the activity levels we were targeting (i.e. “greater than A73R”), we picked the appropriate fluorescence thresholds and computed the corresponding percentile of the overall library. For the sorting experiment, we also count the percentage of droplets that pass the gate.

G1 Gating design

In G1, tested variants were drawn from a randomly generated library (epPCR) on top of a single-site saturation mutagenesis (SSM). Low gate cutoffs were chosen to differentiate between very poor performers (“dead”) and active variants (“alive”). High gate cutoffs were chosen to differentiate between top performers and the rest of the library. Different from all the other libraries, no fiducial sequences were used to determine the gate value of this library.

G2 Gating Design

In G2, we focused on differentiating between variants that were comparable to, or better, than the parent. G2 gates were set at the 86th, 93rd, and 97.5th percentile of the library distribution, corresponding to the left tail, mean, and right tail of the parent fiducial fluorescence distribution, respectively.

G3 Gating Design

In G3, we focused on differentiating between variants that were better/comparable to the parent and better/comparable to the best variant in G2, i.e. A73R. G3 gates were set at the 59th, 80th, 95th, and 99th percentiles of the library distribution, corresponding to the mean of the parent fiducial, an intermediate value between the parent and A73R fiducial distributions, the left tail of the A73R fiducial, and the mean of the A73R fiducial, respectively.

G4 Gating design

In G4, we had multiple target activities we wanted to assess, since sublibraries were focused on both ablations and improvements on previous rounds. G4 gates were set to 70th, 90th, 98th, and 99.5th percentiles, corresponding to the mean fluorescence of the parent, the best G2 variant A73R, the best G3 double (D64A, A73R), and the best G3 quadruple (A63P, A73R, D74H, I84Y), respectively (see Supplementary Figure 27d).

S9: Additional Sublibrary Details

Hit-recombination

In G2, we recombined the top 20 hits from G1 that contained mutations in the G2 design region (see 'Methods: Designed DNA library generation'). The G3 design regions contained residues not appearing in the G2 design region, so we considered the following pools for recombination: the top 30 variants appearing in (or 1 mutation from) the G2 HR library, the top 30 variants from G1 that had previously not been feasible in the G2 design region but were now possible in the expanded G3 regions, and the top 10 single-mutation variants observed in G2 that were not screened in G1. In G4, we recombined the top 70 variants designed by (or 1 aa from) the HR library in G3.

Designed synonyms

In G1, WT synonyms were randomly generated via epPCR. In G2 we picked 50 of the WT synonyms that had appeared in G1, where 37 had 1 nucleotide mutation and 13 had 2 nucleotide mutations. In G3 we constructed 50 WT synonyms and 50 A73R synonyms, stratified by the number of codon mutations: at each of C = 1, 2, 3, 4, 5 we selected c codons within the design region at random and replaced the codon with its highest frequency synonym. We did this 10 times for each value of C, leading to 50 synonyms total. We also included the 50 WT synonyms used in G2. In G4 we constructed 100 synonyms of WT, A73R, and A73R,D74S using a similar procedure, constructing 10 synonyms each at C = 2,3, …, 11.